Classical and Quantum Non-Linear Optical Applications Using the Mach-Zehnder Interferometer

by

Andru Prescod

A dissertation submitted to the Graduate Faculty in Electrical Engineering in partial fulfillment of the requirements for the degree of Doctor of Philosophy, The City University of New York

2010

This manuscript has been read and accepted for the Graduate Faculty in Electrical Engineering in satisfaction of the dissertation requirement for the degree of Doctor of Philosophy.

Roger Dorsinville, Ph.D.

Date — Co-Chair of Examining Committee

Nicholas Madamopoulos, Ph.D.

Date — Co-Chair of Examining Committee

Mumtaz Kassir, Ph.D.

Date — Executive Officer

Barry Gross, Ph.D., Associate Professor, The City College of New York

Fred Moshary, Ph.D., Professor, The City College of New York

Benjamin Dingel, Ph.D., Nasfine Photonics Incorporated

Daniel Nolan, Ph.D., Corporate Research Fellow, Corning Incorporated

Supervisory Committee

THE CITY UNIVERSITY OF NEW YORK

Abstract

CLASSICAL AND QUANTUM NON-LINEAR OPTICAL APPLICATIONS USING THE MACH ZEHNDER INTERFEROMETER

by

ANDRU PRESCOD

Advisers: Professors Roger Dorsinville and Nicholas Madamopoulos

Mach Zehnder (MZ) modulators are widely employed in a variety of applications, such as optical communications, optical imaging, metrology and encryption. In this dissertation, we explore two non-linear MZ applications; one classified as classical and one as quantum, in which the Mach Zehnder interferometer is used.

In the first application, a classical non-linear application, we introduce and study a new electro-optic highly linear (e.g., >130 dB) modulator configuration. This modulator makes use of a phase modulator (PM) in one arm of the MZ interferometer (MZI) and a ring resonator (RR) located on the other arm. The modulator performance is obtained through the control of a combination of internal and external parameters. These parameters include the RR-coupling ratio (internal parameter); the RF power split ratio and the RF phase bias (external parameters). Results show the unique and superior features, such as high linearity (SFDR~133 dB), modulation bandwidth extension (as much as 70%)

over the previously proposed and demonstrated Resonator-Assisted Mach Zehnder (RAMZ) design. Furthermore the proposed electro-optic modulator of this dissertation also provides an inherent SFDR compensation capability, even in cases where a significant waveguide optical loss exists. This design also shows potential for increased flexibility, practicality and ease of use.

In the second application, a quantum non-linear application, we experimentally demonstrate quantum optical coherence tomography (QOCT) using a type II non-linear crystal (periodically-poled potassium titanyl phosphate ($KTiOPO_4$) or PPKTP). There have been several publications discussing the merits and disadvantages of QOCT compared to OCT and other imaging techniques. First, we discuss the issues and solutions for increasing the efficiency of the quantum entangled photons. Second, we use a free space QOCT experiment to generate a high flux of these quantum entangled photons in two orthogonal polarizations, by parametric down-conversion. Third, by ensuring that these down-converted photons have the same frequency, spatial-temporal mode, and the same polarization when they interfere at a beam splitter, quantum interference should occur. Quantum interference of these entangled photons enables high resolution probing of dispersive samples.

ACKNOWLEDGEMENTS

I wish to thank my internal advisors - Drs. Roger Dorsinville (co-Chair), Nicholas Madamopoulos (co-Chair) and Ardie Walser, in addition to my internal supervisory committee members, Drs. Barry Gross and Fred Moshary of City College and external advisors Dr. Daniel Nolan of Corning Inc. and Dr. Benjamin Dingel of Nasfine Photonics for their valuable technical discussions and feedback. Additionally, I extend special thanks to Corning Incorporated for funding my education and research. Lastly, I wish to thank my spouse and partner, Jeanine for her patience as I pursued yet another degree, and my mom for always being supportive and encouraging.

Table of Contents

List of Figures

List of Tables

Table **Page**

PART A: INTRODUCTION

Chapter 1: Introduction and Thesis Objective

1.1. Objective of the thesis

In this dissertation we focus on two nonlinear processes which, combined with the Mach Zehnder Interferometer, result in applications for imaging and communications. The first nonlinear process is the electro-optic effect (the change in the refractive index of a material due to the application of an electric field). The second non-linear process is parametric down-conversion (which can be considered as the reverse of harmonic generation). The two applications discussed in this dissertation both rely on $\chi^{(2)}$ nonlinear polarization effects. Additionally, the first discussed process is based on classical physics while the latter is based on quantum physics. Finally, we divide the dissertation in three sections. Part A is the introduction and consists of Chapters 1-2. Part B consists of Chapters 3-4 and discusses a classical nonlinear optics application which uses the Mach Zehnder interferometer. We introduce a new type of highly-linear optical modulator with the underlying fundamentals based on the electro-optic effect. And, Part C consists of Chapters 5-6 and discusses a quantum nonlinear optics application that uses the MZI. We experimentally investigate an application of parametric down-conversion (Quantum Optical Coherence Tomography).

We begin in Chapter 1 with a brief review of both linear and non-linear optics. We describe the nonlinear polarization effects and the relationships to the electric field strengths of an electromagnetic wave. Then, we discuss some of the most common nonlinear optical processes, which play important roles in the fields of engineering and science, and in particular to the applications described in this dissertation. These

nonlinear optical processes include the electro-optic effect and parametric down-conversion.

In Chapter 2, we introduce the principles of the MZI. We note that although we use a free space design as the foundation of our description, there are many designs and implementations of the MZI, including planar lightwave circuit (PLC) designs in which the interferometer is completely integrated in optical waveguides. However, the interferometric principles of remain the same. As part of Chapter 2, we also discuss both classical and quantum implementations of the MZI, namely second order and fourth order interference scenarios. This discussion is important for discussion since the first application that we present (highly-linear optical modulator) exhibits second order (classical) interference, and the second application (quantum optical coherence tomography) exhibits fourth order (quantum) interference.

In Chapter 3 we introduce the basic theory and designs for linear optical intensity modulators. We discuss their application space and the many categories that exist. As part of this explanation, we review the electrooptic effect, with a special focus on the linear electrooptic effect. Also, since the modulator that is discussed combines a phase modulator and ring resonator in a Mach Zehnder configuration, we review the fundamentals of phase modulators, ring resonators, Mach Zehnder modulators (MZMs) and Ring-Resonator Assisted Mach Zehnder modulators (RAMZs). In the latter part of Chapter 3 we present the merits for characterizing an analog fiber-optic link and more importantly the spurious free dynamic range (SFDR), which is widely used to describe the performance of these modulators, including some potential issues with its usage.

Finally, we summarize the two common electrode configurations (lumped and traveling wave) that can be implemented with the proposed designs.

Chapter 4 summarizes the analytical and numerical analysis of the ultra linear modulator. The analytical model (discussed in Section 4.1) assumes a frequency independent design, with ideal conditions (e.g. no waveguide losses). We derive, from first principles, the transfer function of the device and a rigorous derivation of its fundamental and intermodulation output powers. We demonstrate the device flexibility and its ability to theoretically describe both the RAMZI and MZI under certain conditions. In Section 4.1, we rigorously analyze the lumped electrode design, with a thorough numerical approach to derive the transfer function. From this, we compute the electrical fundamental and intermodulation powers using Fourier analysis. In Section 4.3, we perform a similar analysis on the traveling wave electrode device. Additionally, we investigate the modulation frequency dependence of IMPACC, using well-known Bessel function identities. Finally, the end of Chapter 4 summarizes the content of Part B. We review the merits of the modulator, highlighting its strengths over other highly-linear optical modulators, including the special contributions of two newly-introduced external controls (namely the power split ratio and the RF phase shift).

In Chapter 5, we introduce and discuss a quantum nonlinear optics application (Quantum Optical Coherence Tomography, QOCT). We first summarize the theory underlying both Optical Coherence Tomography (OCT) and QOCT. QOCT is a fourth order interference technique that uses quantum-entangled photons, which are generated via spontaneous parametric down-conversion. Constructive and destructive quantum interference of "coincident" entangled photons provides significant benefits over OCT.

Because of this, we summarize the process of spontaneous parametric down-conversion, in addition to related concepts, such as ideal phase matching, non-ideal phase matching, quasi-phase matching and the concept of coincident photons.

Chapter 6 details an experimental demonstration of quantum interference of coincident photons. We generate down-converted quantum-entangled photons from a nonlinear periodically poled $\chi^{(2)}$ crystal. We investigate the coincidence counts and evidence of quantum destructive interference, which only occurs if the spatio-temporal modes, frequency and polarization of the interfering photons are the same (otherwise known as indistinguishable photons). Lastly, at the end of Chapter 6, we summarize the contents of Part C of the dissertation. We state our conclusions from the experimental results and our review of the literature and similar experimental attempts. We discuss the challenges of the experiment and future work is proposed.

1.2. Linear Optics

To understand the field of linear optics, one needs to understand the principles of interaction of light and matter. Matter can be considered as a large number of positively charged nuclei that are encircled by negatively charged electrons (or atoms). The interaction of light with matter typically occurs at the valence shells of these atoms, resulting in electronic polarization (essentially oscillations of the electric fields).

Light can be considered to be an electromagnetic wave with rapidly oscillating electric and magnetic fields, whose relationship is governed by the well-known Maxwell's equations, shown below in their differential form[1].

$$\nabla \cdot \vec{D} = \rho \tag{1.1}$$

$$\nabla \cdot \vec{B} = 0 \tag{1.2}$$

$$\nabla \times \vec{E} = \frac{-\partial \vec{B}}{\partial t} \tag{1.3}$$

$$\nabla \times \vec{H} = \vec{J} + \frac{\partial \vec{D}}{\partial t} \tag{1.4}$$

Additionally, for homogeneous materials:

$$\vec{D} = \varepsilon \vec{E} = \varepsilon_0 (1 + \chi)\vec{E} = \varepsilon_0 \vec{E} + \varepsilon_0 \chi \vec{E} = \varepsilon_0 \vec{E} + \varepsilon_0 \chi \vec{E} \tag{1.5}$$

$$\vec{B} = \mu_0 \left(\vec{H} + \vec{M}\right) = \mu_0 \left(\vec{H} + \chi_M \vec{H}\right) = \mu_0 (1 + \chi_M)\vec{H} = \mu \vec{H} \tag{1.6}$$

where, $\vec{D}$ is the electric flux density, $\vec{B}$ is the magnetic flux density, $\vec{E}$ is the electric field intensity, ρ is the electric charge density, ε is the electric permittivity, ε_0 is the permittivity of free space, $\vec{H}$ is the magnetic field intensity, $\vec{J}$ is the current density, $\vec{M}$ is the magnetization, μ is the magnetic permeability, μ_0 is the permeability of free space, χ is the electric susceptibility, χ_M is the magnetic susceptibility, and the speed of light, $c = \frac{1}{\sqrt{\mu_0 \varepsilon_0}}$. In linear optics, the induced polarization, $\vec{P}(t)$, is proportional to the strength of the applied electric field, $\vec{E}(t)$, and can be expressed as:

$$\vec{P}(t) = \chi^{(1)} \vec{E}(t) \tag{1.7}$$

where $\chi^{(1)}$ is a constant known as the linear susceptibility.

For inhomogeneous materials, the electric permittivity is position dependent and Eq. 1.5 can be written as:

$$\vec{D}\left(\vec{r},t\right)=\varepsilon\left(\vec{r}\right)\vec{E}\left(\vec{r},t\right) \tag{1.8}$$

For anisotropic materials, the electric permittivity depends on the x, y and z directions and is written in tensor form:

$$\begin{pmatrix} D_x \\ D_y \\ D_z \end{pmatrix} = \begin{pmatrix} \varepsilon_{xx} & \varepsilon_{xy} & \varepsilon_{xz} \\ \varepsilon_{yx} & \varepsilon_{yy} & \varepsilon_{yz} \\ \varepsilon_{zx} & \varepsilon_{zy} & \varepsilon_{zz} \end{pmatrix} \begin{pmatrix} E_x \\ E_y \\ E_z \end{pmatrix} \tag{1.9a}$$

and the polarization can be written as:

$$\begin{pmatrix} P_x \\ P_y \\ P_z \end{pmatrix} = \varepsilon_0 \begin{pmatrix} \chi_{xx} & \chi_{xy} & \chi_{xz} \\ \chi_{yx} & \chi_{yy} & \chi_{yz} \\ \chi_{zx} & \chi_{zy} & \chi_{zz} \end{pmatrix} \begin{pmatrix} E_x \\ E_y \\ E_z \end{pmatrix} \tag{1.9b}$$

where χ_{ij} is the electric susceptibility tensor and $\varepsilon_{ij} = \varepsilon_{ji} = \varepsilon_0\left(1+\chi_{ij}\right)$, which implies that it is symmetric with six independent elements.

In dispersive materials, the electric permittivity depends on the frequency of the applied electric field and is governed by the relationship:

$$\vec{D}\left(\vec{r},\omega\right)=\varepsilon\left(\vec{r}\right)\vec{E}\left(\vec{r},\omega\right) \tag{1.10}$$

Although all materials have some measure of dispersion, the dependence is typically for a certain range of frequencies.

1.3. Non-Linear Optics

The field of non-linear optics essentially began with the 1961 ruby laser experiment by Franken et al.[2, 3] In this experiment, a high intensity beam of red light (λ=694 nm, f ≈ 432 THz) was focused on a quartz crystal, resulting in a faint blue beam (λ=347 nm, f ≈ 864 THz), which is the first harmonic of red. Subsequent work by Bloembergen et al (1965) further developed the field.[4]

In non-linear optics, the electric permittivity may depend on the magnitude of the applied electric field and thus can be written as:

$$\varepsilon\left(E\right)=\varepsilon+\varepsilon_2 E+\varepsilon_3 E^2+... \tag{1.11}$$

So, with the typical assumption that the electric field is of the form $E = E_0 e^{jwt}$, then the electric flux density can be written as:

$$D=\varepsilon\left(E\right)E=\varepsilon E+\varepsilon_2 E^2+\varepsilon_3 E^3+...=\varepsilon E_0 e^{j\omega t}+\varepsilon_2 E_0^2 e^{j2\omega t}+\varepsilon_3 E_0^3 e^{j3\omega t}+... \tag{1.12}$$

Thus, non-linear effects result in the generation of higher harmonics which may be an undesired attribute in some cases, such as when the input intensity in optical fiber is too high, resulting in higher harmonics and hence noise terms. In other cases, such as applications that utilize the electro-optic effect (e.g. second harmonic imaging microscopy) these higher harmonics are a desired attribute, since they do not excite molecules, as in other techniques such as fluorescence microscopy. Therefore, negative side effects such as photo-bleaching are minimized.

Additionally, whereas in Eq. 1.7, the polarization is linearly proportional to the electric field in linear optics, in the non-linear domain the polarization is now a power series of the electric field:

$$\begin{aligned}\vec{P}(t) &= \chi^{(1)}\vec{E}(t) + \chi^{(2)}\vec{E}^{2}(t) + \chi^{(3)}\overrightarrow{E^{3}}(t) + \ldots \\ \vec{P}(t) &= \vec{P}^{(1)}(t) + \vec{P}^{(2)}(t) + \vec{P}^{(3)}(t) + \ldots\end{aligned} \tag{1.13}$$

In this case $\chi^{(2)}$ and $\chi^{(3)}$ are the second and third order nonlinear susceptibilities and $\vec{P}^{(2)}(t)$ and $\vec{P}^{(3)}(t)$ are the second and third order polarizations.

1.4. Types of Nonlinear Optical Processes

There are many types of nonlinear optical process. They include parametric processes (identical initial and final quantum-mechanical states, real susceptibilities and conservation of photon energies), such as second harmonic generation, intensity-

dependent refractive index, parametric down-conversion, sum and difference frequency generation, and optical parametric oscillation; and non-parametric processes, such as two-photon absorption, saturable absorption, stimulated Brillouin scattering, stimulated Rayleigh scattering and stimulated Raman scattering[5]. This is certainly not an exhaustive list. Below, we briefly introduce and summarize some of the processes mentioned above.

In second harmonic generation (SHG), when an electric field of frequency ω is incident on a crystal with non-zero $\chi^{(2)}$ a resultant output field of frequency 2ω is produced. At optimum experimental conditions, the efficiency of generating the second harmonic frequency from the incident radiation can approach 100%.

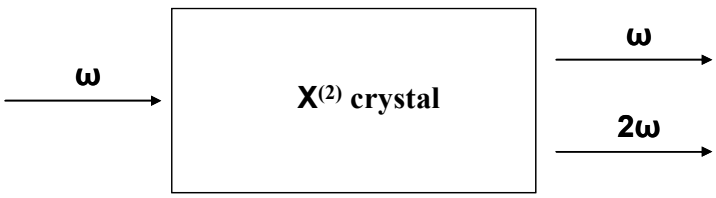

Figure 1.1: Second Harmonic Generation[5]

The nonlinear polarization produced in the $\chi^{(2)}$ crystal is:

$$\vec{P}^{(2)}(t) = \chi^{(2)}\vec{E}^{2}(t) \tag{1.14}$$

In sum frequency generation (SFG), two frequencies ω_1 and ω_2 incident on a crystal with non-zero $\chi^{(2)}$ a results in an output frequency ω_3 that is the sum of the input frequencies.

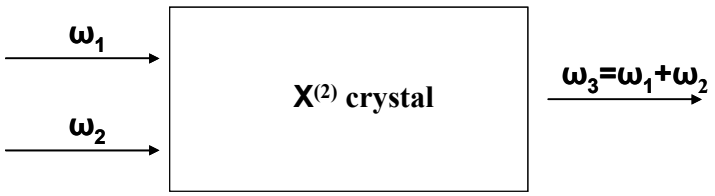

Figure 1.2: Sum Frequency Generation[5]

The nonlinear polarization produced in this process is:

$$\vec{P}(\omega_1+\omega_2)=2\chi^{(2)}\vec{E}_1\vec{E}_2 \tag{1.15}$$

In difference frequency generation (DFG), two frequencies ω_1 and ω_2 incident on a crystal with non-zero $\chi^{(2)}$ a results in an output frequency ω_3 that is the difference of the input frequencies.

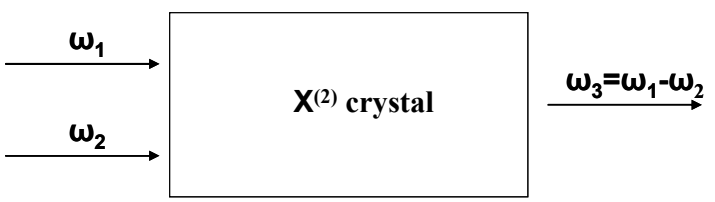

Figure 1.3: Difference Frequency Generation[5]

The nonlinear polarization produced in this process is:

$$\vec{P}(\omega_1-\omega_2)=2\chi^{(2)}\vec{E}_1\vec{E}_2^{*} \tag{1.16}$$

In optical parametric oscillation (OPO), a pump with frequency two frequencies ω_p (pump frequency) is incident on a crystal with non-zero $\chi^{(2)}$, which is placed in an optical resonator. In this way, the generated frequencies ω_s (signal frequency) and ω_i (idler frequency) interact to cause a stimulated emission of more photons at these frequencies. Fig. 1.4 shows the schematic of a typical optical parametric oscillator.[5]

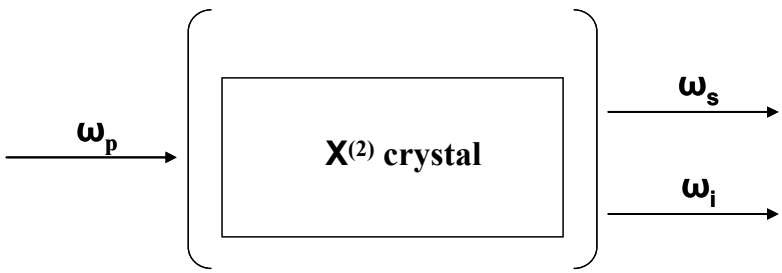

Figure 1.4: Optical Parametric Oscillator[5]

Chapter2: Review of the Mach Zehnder Interferometer

2.1. Fundamentals of the Mach Zehnder Interferometer

The Mach-Zehnder interferometer (MZI) is widely used in optics to determine the relative phase shift between two collimated light beams. Both light beams typically originate from a coherent source. The incoming beam is typically split into to beams that traverse different paths and recombine at final beam combiner. The relative phase shift between the two beams depends on the relative optical path length difference of the two beams. This path length difference may be due to a sample material in one of the beam paths, or the actual path length difference between the two paths. The main difference between the Mach-Zehnder interferometer and the more commonly known, and used, Michelson interferometer is that in the Michelson interferometer the beam splitting optical element is also used as the beam combiner. In some applications, such as the ones discussed here, the geometry of the MZI enables easier alignment and the ability to achieve a zero phase shift between the two paths when the path lengths are equal.

Fig. 2.1 below shows the typical configuration of the MZI. An incident collimated optical beam (E_{in}) splits into two beams at the interface of a half-silvered mirror (or beam splitter). Each of the beams then reflects off of an additional separate mirror, while traversing two different paths. If a sample is placed in one of the paths (typically called the sample path), and/or the path lengths are different, a relative phase shift between the sample path and the other path (reference path) results in an interference pattern, which is observed at the detectors after a final overlap another half-

silvered mirror/beam splitter. The MZI (and other types of interferometers) is used in a wide variety of fields, including metrology, fiber optics, nuclear physics, classical and quantum optics and astronomy. The interference technique described above is also categorized as homodyne detection (two interfering beams have the same frequency), as opposed to heterodyne detection (in which one of the two beams is modulated before detection).

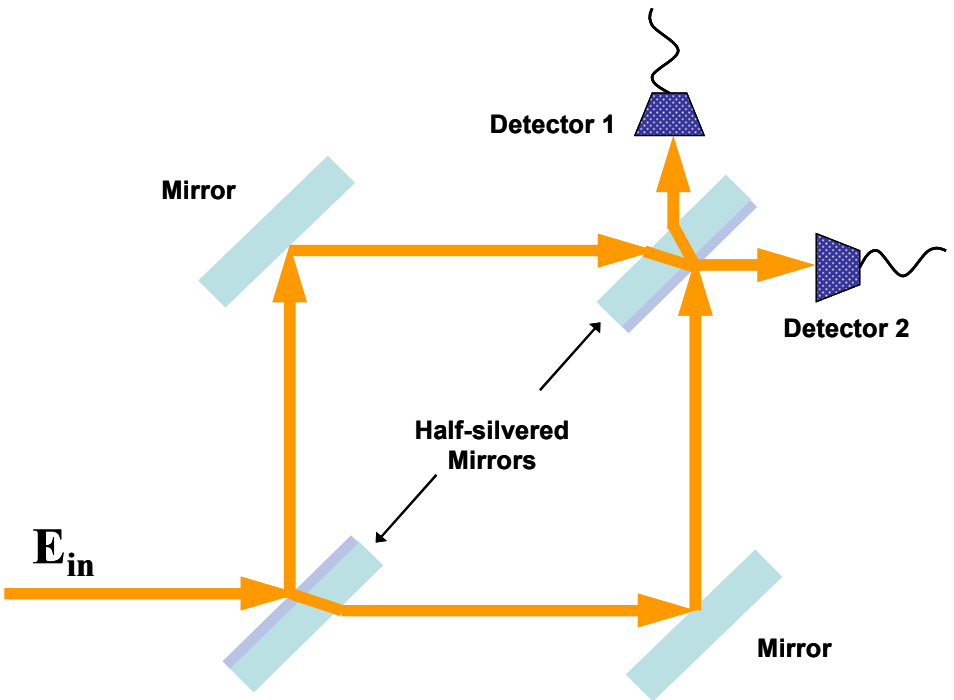

Figure 2.1: Mach Zehnder Interferometer

It is important to note again that both of the applications we discuss in this dissertation use a Mach-Zehnder configuration. However, in the first application (the ultra-linear modulator) we use a classical interference technique, in which the half-silvered mirrors are replaced by a fiber-optic or optical waveguide-based splitter and combiner. In the second application (Quantum Optical Coherence Tomography) we use a quantum interference technique, which include other optical components such as

polarization beam splitters and waveplates. We first describe the basic operation principle of the Mach Zehnder interferometer under the classical interference scheme. Then we discuss the Mach Zehnder interferometer under the quantum interference scheme.

2.2. Classical Interference in the Mach Zehnder Interferometer

The half-silvered surface of the first mirror faces the incoming beam, and the half-silvered surface of the last mirror faces the outgoing beam. It is very important that this outgoing beam exits in the same orientation as the original collimated beam (as seen in Fig. 2.1). Also evident from Fig 2.1 is the impact of the higher refractive index of the glass mirrors compared to air, the location of the silvered surface in the path of the incoming beam and the resultant phase shifts.

If the silvered surface faces the incoming beam then that implies that the incoming beam reflects from the surface of a glass medium, causing a phase shift of half the optical wavelength. However, if the silvered surface is on the opposite side to the incoming beam, then the beam first refracts as it passes through the glass and then is reflected from the surface of an air medium, and thus causing no phase shift. Lastly, when light propagates through a material of refractive index n, it slows and a phase shift proportional to n occurs.

When no sample is present, the glass plates have equal thickness and the path lengths are equal, hence constructive interference occurs at detector 2 because there is no

phase difference between the beams. Each beam experiences two reflections from a front surface and one transmission through a glass plate. However, there is a relative phase difference between the two beams at detector 1, because one beam experiences two transmissions and one front reflection, and the other beam experience two front reflections and one rear reflection. With a sample present the intensities of the beams incident on detectors 1 and 2 will vary, allowing one to determine the phase shift caused by the presence of the sample. Typically, since the sample is placed in one of the arms of the Mach Zehnder interferometer, the beam propagating in that arm is referred to as the sample beam, whereas the other beam is referred to as the reference beam.

2.3. Quantum Interference in the Mach Zehnder Interferometer

In section 2.1, the classical interference refers to the superposition of classical light waves and the interference patterns that result. But according to the quantum theory of light, light can also be viewed as a stream of massless photons. In the quantum version of the famous double slit experiment, it was shown that an interference pattern can also be achieved "one photon at a time", essentially implying that a photon can interact with itself.[6] In the view of the quantum interpretation, the photon has a wave function and a statistical probability of passing through one of the two slits.

Applying this concept to the MZI, quantum interference effects can be observed by interacting indistinguishable photons at the final half-silvered mirror (beam splitter). These photons can be generated by a variety of sources. Notably, we will discuss the

generation (via parametric down-conversion) and detection of indistinguishable (quantum entangled) photons within the Mach Zehnder interferometer configuration.

To understand the interference effects that occur at a 50:50 beam splitter (half-silvered mirror) we consider an enlarged view of the photon interactions (Fig. 2.2) and the amplitude contribution scenarios (Fig. 2.3). In Fig. 2.2, we label the reference and sample beams that interact at the final beam splitter. It shows the reflected and transmitted beams at the top surface (solid lines) and the reflected beams at the back surface (dotted lines). The latter beams (dotted lines) are ignored for this analysis. They are faint and do not overlap with the other beams because of the finite thickness of the beam splitter.

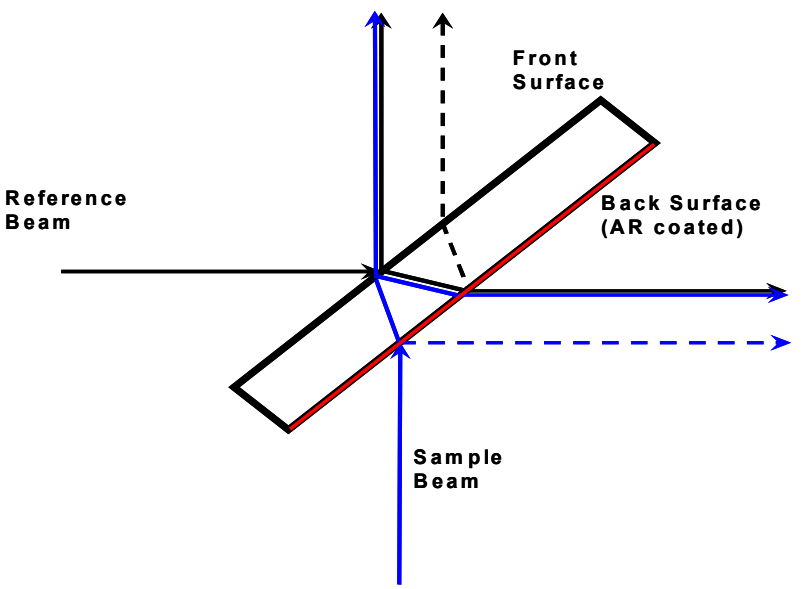

Figure 2.2: Final 50:50 Beam Splitter in Experiment

In Fig. 2.3, we consider two photons, one in each input mode of the 50:50 beam splitter (BS). There are four probable ways for the photons to behave at the front surface. We label these probable scenarios from 1-4. They are:

Scenario 1: the reference photon is reflected and the sample photon is transmitted.

Scenario 2: the reference and sample photons are both reflected.

Scenario 3: the reference and sample photons are both transmitted.

Scenario 4: the reference photon is transmitted and the sample photon is reflected.

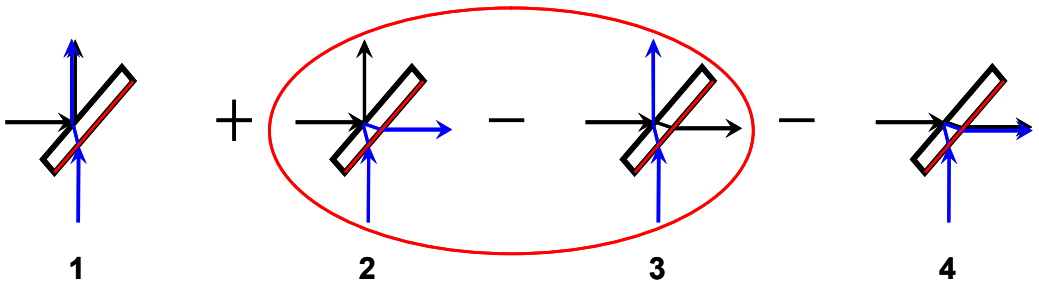

Figure 2.3: Two-Photon Reflection and Transmission at the final Beam Splitter

It is assumed that the reference and sample photons are identical in their physical properties (i.e., polarizations, spatial-temporal mode structures, and frequencies). Because of this, and the fact that the state of the beam splitter does not store which of the four scenarios actually occurs, we add all four probable scenarios at the amplitude level (according to Feynman's rule).[7]

Additionally, reflection off the bottom side of the beam splitter introduces a relative phase shift of "−1" in the associated term in the superposition. This is required by the reversibility of the quantum evolution of the beam splitter. Lastly, since the reference and sample photons are identical, we cannot distinguish between the output states of scenarios 2 and 3. The relative minus sign between these two scenarios therefore causes cancelation (or destructive interference). This cancelation accounts for the quantum interference dip in quantum interference.

PART B: CLASSICAL NON-LINEAR OPTICS APPLICATION

Chapter 3: INTRODUCTION: Linear Intensity Modulators

3.1. Applications and Requirements of Linear Intensity Modulators

The performance of analog fiber-optic (FO) links is critical for photonics to provide utility to RF systems.[8, 9] Efficient electrical-to-optical (EO) conversion and optical-to electrical (OE) conversion are imperative for photonic solutions to be competitive with conventional RF electronics. Optical fiber, with virtually lossless signal transport over wide-band frequencies and long distances, provides a very good starting point. In the past, it has been the EO and OE conversion losses that have significantly impaired RF link performance. However, recent progress in laser, modulator and detector component technologies are beginning to remove this impairment and create new photonics insertion opportunities.[10]

Typically, military applications have been the main application space for analog FO-links.[11, 12] Conventional antenna systems are typically designed to operate in either transmit or receive mode, and are typically fed electronically with a coaxial cable from the processing station. Such electronic feeds entail high loss, are heavy, and significantly degrade the size, weight and power efficiencies of the link. Photonic technologies on the other hand are very attractive for application in antenna systems due to their low loss, lightweight flexible cabling, immunity to electromagnetic interference, broad bandwidth, and overall ability to remote antennas over distances not possible with conventional electronic approaches. In addition, optical wavelength multiplexing techniques allow for

multiple channel transport with no interference over a single physical channel and the potential for parallel processing.

Photonically remoting the antenna aperture significantly alleviates the power burden at the aperture because a majority of the power hungry components can now be located at an in-board processing station. Furthermore, in shipboard and avionic applications the coaxial cable runs from the antenna aperture to the processing station, and can range from tens of feet up to a thousand feet. Also, typically there are many such coaxial cable runs on board any given ship or aircraft. There is a significant size, weight, power reduction and redistribution potential when these coaxial cables are replaced with the much more efficient photonic links. Such migration is already occurring in the case of digital buses employed in shipboard and avionic networking applications. RF systems on the other hand are still heavily dependent on conventional high-speed electronic technologies and are therefore constrained by the performance, prime power, and distance limitations of the coaxial cable.

Ultra-linear modulators are critical components for these types of high end FO-link based RF communication systems. In addition, broadband access applications in analog fiber-optic communication links, such as Radio-over-Fiber (RoF), Radio-over-Free Space (RoFS) and ultra-dense (cable television) CATV can also be benefited by ultra-linear modulators.[13]

With the advent of long distance broadband communication and the need for highly linear and fast modulating capability, external ultra-linear modulators have become vital components in the broadband network. External modulators are typically preferred over direct (or internal) modulators, since the latter are usually limited by the

relative intensity noise (RIN) performance of the laser source. Because of need for highly linear modulators, extensive research on linear modulator designs has been published in recent literature.[14, 15, 16, 17, 18, 19] Some key performance measures of these external modulators include the linearity or spurious free dynamic range (SFDR), RF bandwidth capability, low half-wave (V_π) voltage, low insertion loss, minimal design complexity and minimal cost.

Ultra-linear optical modulators with SFDR capability in the range of 130-140 dB have been introduced.[18, 20, 21] This modulator is based on a modified version of a Michelson Gires-Tournois Interferometer (MGTI)- which was invented by Dingel et al.[22, 23] In that design, the optical and RF performance depended on the optimization of two parameters – a power splitting ratio (F) and a coupling ratio (τ), which are further explained below. The SFDR performance of this modulator made it an apparent candidate for applications, such as ultra-dense CATV and RoF, in which it is generally accepted that the SFDR requirement is >130 dB.

However, in addition to the high linearity requirement, other key attributes are high bandwidth capability (>10 GHz) and large link gain. Many different designs have been investigated in the literature, with a recent large scale effort on ring resonator-assisted modulators (RAMZs).[24, 26] The new modulator, described here, is a novel modified implementation of the ring resonator-assisted design.

It is generally accepted that optical modulator designs which incorporate a ring-resonator will be limited by the free spectral range (FSR) of the ring. Because of this, methods to produce rings with small dimensions (hence higher FSR) have been studied.[25] We have opted to take a unique approach, in which we try to extend the bandwidth and

also the linearity performance by the careful control of a few parameters that we will detail below.

So, this part of the dissertation has a two-fold goal. First, we introduce the new configuration of the ultra-linear optical modulator with very high SFDR (~133 dB). Also, we present a powerful technique that simultaneously increases:

(1) the SFDR, and

(2) the linearization modulation bandwidth range (compared with RAMZ) by using an external tunable RF phase delay and a power splitter.

We present the models of the modulator and we investigate optimization of the parameters to obtain ultra-linear response. The dissertation will also identify the critical parameters and the limits of the associated improvements.

In the following sections we present the following. In Section 3.2, we present a brief overview of linear intensity modulators. In Section 3.3, we discuss the important parameter that defines the linearity of the device or link - namely SFDR. In Section 3.4, we differentiate between a lumped electrode design and a traveling wave electrode design. Then, in Section 3.5, we introduce the lumped electrode design of the Highly Linear Optical Modulator (IMPACC which stands for Interferometric Modulator with Phase-modulating And Cavity-modulating Components). We provide the theoretical basis of the new design, and discuss the performance of the new modulator in terms of:

(1) high SFDR value,

(2) effect of RF frequency modulation, and

(3) effect of RF phase bias.

Lastly, in Section 3.6, we analyze the traveling wave configuration of the IMPACC. In our analysis of IMPACC, we compare the corresponding results with the performance of MZ and RAMZ modulators.

3.2. Types of Linear Intensity Modulators

As shown in **Fig. 3.1** below, linear intensity modulation can be divided into two groups: internal (or direct) modulation and external modulation. Direct modulators are typically used for low bandwidth applications (<3GHz) and are typically cheaper than external modulators. Part of focus of this dissertation is on an external modulator. As described in by Dingel et al.[26], external modulation can be classified into three main groups: (i) Direct coupler (DC) modulators, (ii) Mach-Zehnder (MZ) modulators and (iii) Electro Absorption (EA) modulators.

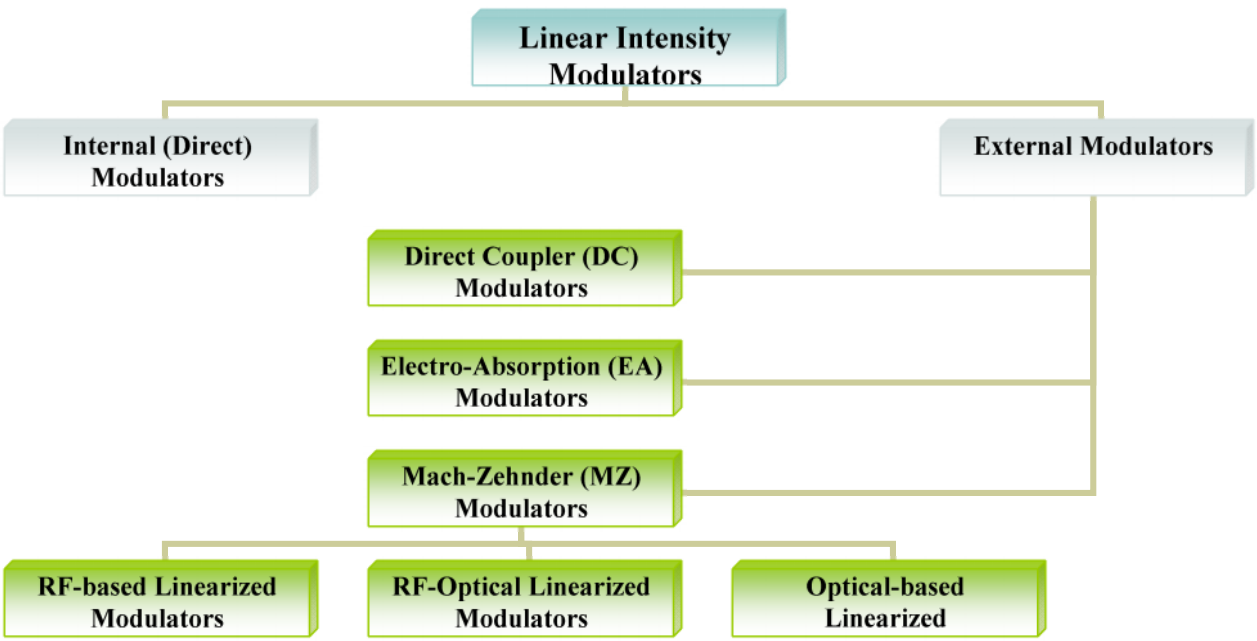

Figure 3.1: Types of Linear Intensity Modulators

The modulator described in this Chapter falls under the category of Mach-Zehnder (MZ) type modulators. More specifically, it is an optical-based linearized-type MZ modulator – one of the sub-classifications in this category. MZ-type modulators also include RF-based and hybrid RF-optical linearized types, but these types are typically limited by low bandwidth capability, moderate SFDR performance and low tolerance to parameter variation.[26]

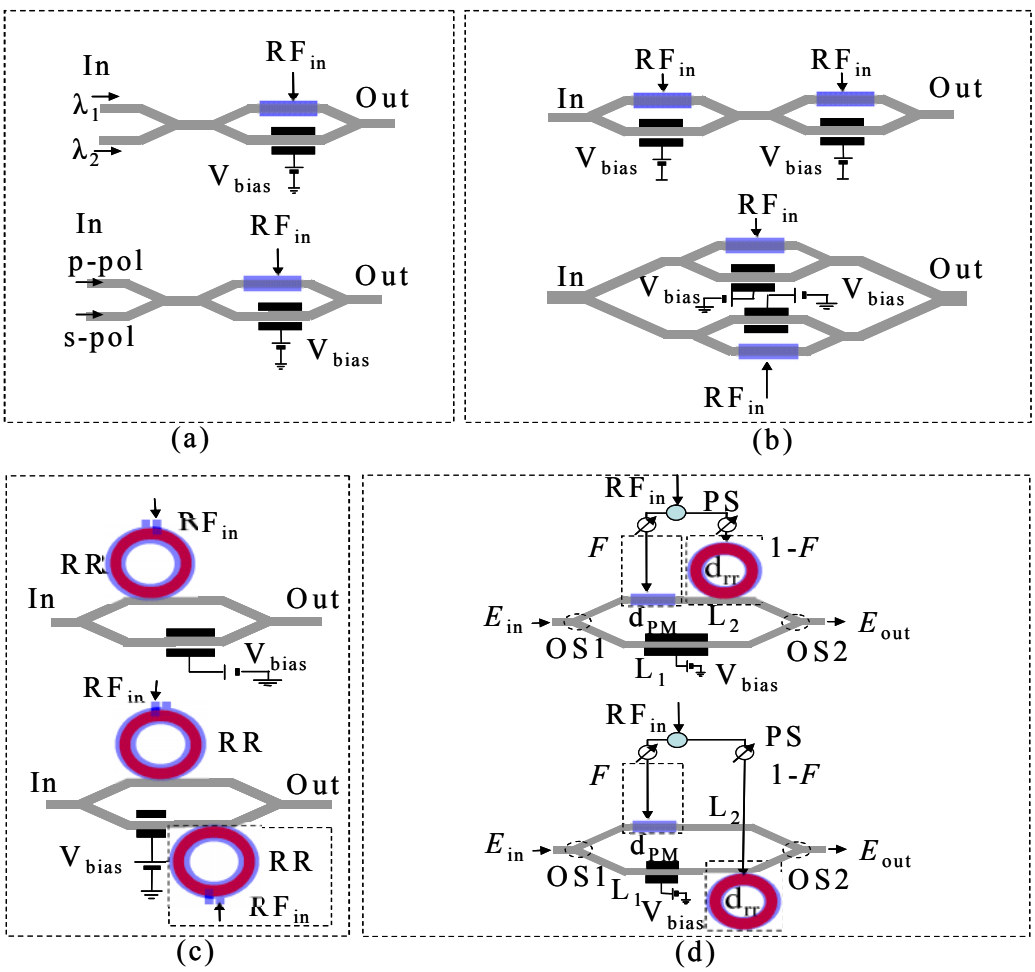

Figure 3.2: Optically linearized MZI-based modulator designs. (a) dual-signal MZI-based modulators, (b) series or parallel MZI modulators, (c) single and dual RAMZI configurations, (d) two different configurations of IMPACC. (PS: RF power splitter, OS1: optical splitter, OS2: optical combiner).

There are many different categories of optical based Linearized-type MZ modulators (as in **Fig 3.2**), including dual signal MZI modulators, cascaded MZ modulators and ring

resonator-assisted (RAMZ) modulators.[26] The new modulator design that is introduced here (the super-linear optical modulator) will be shown to have superior performance characteristics and greater flexibility than those in **Fig 3.2**. However, we first review the building blocks of our proposed IMPACC. Hence, we present fundamentals of the phase modulator (PM), ring resonator (RR), Mach-Zehnder interferometer (MZI) and ring resonator-assisted MZ (RAMZ), after which we analyze the combined performance of the IMPACC, which incorporates the PM and RR in a MZI configuration.

3.3. The Electrooptic Effect

We saw earlier that Eq. 1.9 represents the relationship between the electric flux density and the electric field intensity for an anisotropic material. Additionally, for a lossless, non-optically active material, Eq. 1.9 can be transformed to a new coordinate system (X, Y, Z), otherwise known as the principal axis system, resulting in the following relationship:[5]

$$\begin{pmatrix} D_X \\ D_Y \\ D_Z \end{pmatrix} = \begin{pmatrix} \varepsilon_{XX} & 0 & 0 \\ 0 & \varepsilon_{YY} & 0 \\ 0 & 0 & \varepsilon_{ZZ} \end{pmatrix} \begin{pmatrix} E_X \\ E_Y \\ E_Z \end{pmatrix} \tag{3.1}$$

The energy density in the principal axis system can thus be derived and expressed in terms of the principal axis coordinates (X, Y, Z):

$$U = \frac{1}{8\pi} \vec{D} \cdot \vec{E} = \frac{1}{8\pi} \left(\frac{D_X^2}{\varepsilon_{XX}} + \frac{D_Y^2}{\varepsilon_{YY}} + \frac{D_Z^2}{\varepsilon_{ZZ}} \right) = \frac{X^2}{\varepsilon_{XX}} + \frac{Y^2}{\varepsilon_{YY}} + \frac{Z^2}{\varepsilon_{ZZ}} = 1 \tag{3.2}$$

This is the well-known index ellipsoid (or optical indicatrix), which can be also expressed in the form:

$$\frac{X^2}{n_X^2}+\frac{Y^2}{n_Y^2}+\frac{Z^2}{n_Z^2}=1 \tag{3.3}$$

Where the n_i's are refractive indices along the corresponding principal axes. A crystal is called bi-axial (e.g. calcite) if $n_X \neq n_Y \neq n_Z$. A crystal is uniaxial if two of the refractive indices are equal, e.g. $n_X = n_Y = n_o \neq n_Z$ (e.g. quartz and lithium niobate, $LiNbO_3$). In this crystal, a polarized wave (called the ordinary wave) experiences the index n_O, while another orthogonal polarization (called the extra-ordinary wave) experiences a refractive index that ranges from n_o to n_e.

However, *x*, *y*, and *z* do not always lie along the respective principal axes. They could lie along the crystal axes. So, a generalized form of Eq. 2.3 is:

$$\left(\frac{1}{n^2}\right)_1 x^2+\left(\frac{1}{n^2}\right)_2 y^2+\left(\frac{1}{n^2}\right)_3 z^2+\left(\frac{1}{n^2}\right)_4 2yz+\left(\frac{1}{n^2}\right)_5 2xz+\left(\frac{1}{n^2}\right)_6 2xy=1 \tag{3.4}$$

where the $\left(\frac{1}{n^2}\right)_i$ coefficients can be expressed in terms of the principal axes' permittivities ε_{XX}, ε_{YY}, and ε_{ZZ}. Eq. 2.4 can be expressed as:

$$\eta_{11}x^2+\eta_{22}y^2+\eta_{33}z^2+2\eta_{23}yz+2\eta_{13}xz+2\eta_{12}xy=1 \tag{3.5}$$

The η_{ij} 's (impermeability tensors) can be expanded as a power series of the electric field components,

$$\eta_{ij}\left(\vec{E}\right) - \eta_{ij}^{(0)} = \Delta\eta_{ij} = \sum_{k} r_{ijk} E_k + \sum_{kl} s_{ijkl} E_k E_l + \ldots$$
$$= \sum_{k} f_{ijk} P_k + \sum_{kl} g_{ijk} P_k P_l + \ldots. \tag{3.6}$$

The r_{ijk} and f_{ijkl} tensors describe the linear electrooptic effect and the s_{ijk} and g_{ijkl} tensors describe the quadratic electrooptic effects (both nonlinear effects) in which the refractive index has a linear (Pockel's effect) or quadratic (Kerr electrooptic effect) dependence on the electric field intensity. The coefficients have the relationships: [5]

$$f_{ijk} = \frac{r_{ijk}}{\varepsilon_k - \varepsilon_0} \tag{3.7}$$

$$g_{ijkl} = \frac{s_{ijkl}}{\left(\varepsilon_k - \varepsilon_0\right)\left(\varepsilon_l - \varepsilon_0\right)} \tag{3.8}$$

Here, ε_k and ε_l are the principal optical dielectric constants.

For this dissertation we focus on the importance of the linear electrooptic effect, for which some of its applications are described briefly in the sections below. In this case, it can be shown that depending on the class of the crystal, the r_{ijk} and f_{ijkl} tensors can be greatly simplified due to symmetry, since ε_{ij} and its inverse η_{ij} are both real and

symmetric.[5] Because of this, it is common to simplify the expression for the third rank tensor electrooptic coefficient, r_{ijk}, by a two dimensional 6×3 matrix r_{hk}, where h is defined as:

$$h = \begin{cases} 1 & \text{for } ij = 11 \\ 2 & \text{for } ij = 22 \\ 3 & \text{for } ij = 33 \\ 4 & \text{for } ij = 23 \text{ or } 32 \\ 5 & \text{for } ij = 13 \text{ or } 31 \\ 6 & \text{for } ij = 12 \text{ or } 21 \end{cases} \tag{3.9}$$

and,

$$r_{hk} = \begin{bmatrix} r_{11} & r_{12} & r_{13} \\ r_{21} & r_{22} & r_{23} \\ r_{31} & r_{32} & r_{33} \\ r_{41} & r_{42} & r_{43} \\ r_{51} & r_{52} & r_{53} \\ r_{61} & r_{62} & r_{63} \end{bmatrix} \tag{3.10}$$

The r_{ij}'s are determined by the rotational symmetry of the medium, and they determine the rate of change of η_{ij}'s with increasing electric field strength (lowest order approximation of Eq. 3.6). Because of the symmetry of many of these crystal groups, many of the r_{ij}'s vanish.[27]

3.4. Fundamentals of Phase Modulators (PMs)

If an incident beam is polarized parallel to one of the axes (x') of a polarizer, as shown in **Fig. 3.3** below, then the application of a sinusoidal electric field in the z-direction (E_z) changes the output phase by:[5, 27]

$$\Delta\phi_{x'} = -\frac{\omega L}{c}\Delta n_{x'} \tag{3.11}$$

where L is the crystal length, c is the speed of light, ω is the optical frequency and,

$$\Delta n_{x'} = \frac{\omega n_0^3 r}{2c} E_z L \tag{3.12}$$

where r is the electro-optic coefficient $\left(r = r_{63} = r_{6z} = r_{xyz} = r_{yxz}\right)$, and n_0 is the refractive index. E_z can be written as:

$$E_z = E_m \sin \omega_m t \tag{3.13}$$

where E_m is the electric field amplitude and ω_m is the modulation frequency.

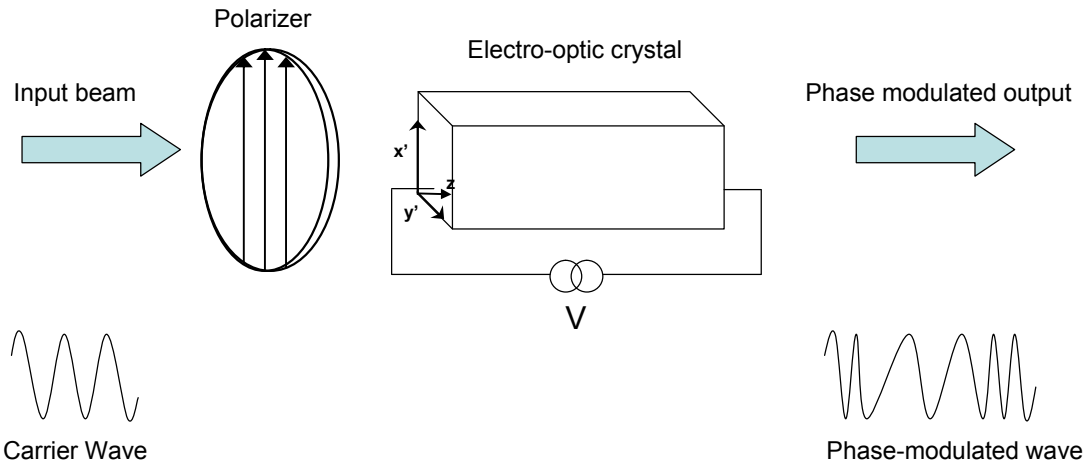

Figure 3.3: Electro-optic phase modulator[27]

If we then assume that an input electric field, $E_{in} = A\cos\omega t$, traverses through the modulating crystal, then the resulting output electric field, E_{out} is given by:[27]

$$E_{out} = A\cos\left[\omega t - \frac{\omega}{c}\left(n_0 - \frac{n_0^3}{2} r E_m \sin\omega_m t\right)L\right] \tag{3.14}$$

If we drop the constant phase factor, we have

$$E_{out} = A\cos\left[\omega t + \delta\sin\omega_m t\right] \tag{3.15}$$

where

$$\delta = \frac{\omega n_0^3 r E_m L}{2c} = \frac{\pi n_0^3 r E_m L}{\lambda} \tag{3.16}$$

is the phase modulation index. Therefore, the optical wave is phase modulated with a modulation index δ. Eqns. 3.15 and 3.16 will be utilized in the analysis of the new modulator design in Section 4.

3.5. Fundamentals of Ring Resonators

The basic formulation for the physics of ring resonators has been extensively discussed.[28, 29, 30] We follow this analysis, in which a ring resonator is coupled to a bus waveguide. With the assumptions that the coupling is lossless and a single mode of the resonator is excited, the matrix equation (with coupling coefficients τ and κ) describing the interactions, shown in **Fig 3.4** below are:

$$\begin{pmatrix} a_2 \\ b_2 \end{pmatrix} = \begin{pmatrix} \tau & -i\kappa \\ -i\kappa & \tau \end{pmatrix} \begin{pmatrix} a_1 \\ b_1 \end{pmatrix} \tag{3.17}$$

where

$$\tau^2 + \kappa^2 = 1 \tag{3.18}$$

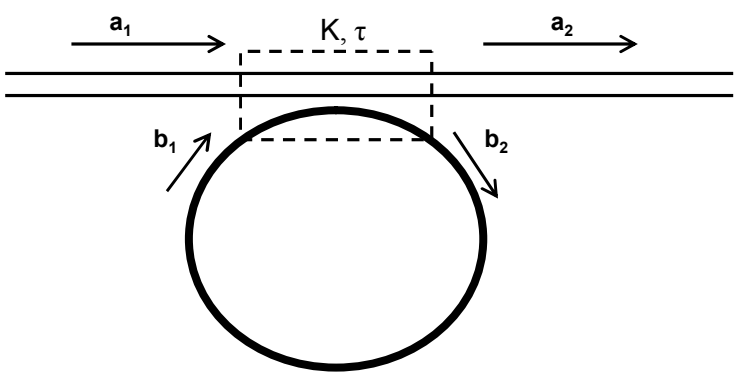

Figure 3.4: Ring Resonator (RR) with one bus waveguide

Therefore, after *one* round trip, we have:

$$\begin{aligned} a_2 &= \tau a_1 - i\kappa b_1 = \tau a_1 - (i\kappa)\alpha e^{-i\theta} b_2 \\ &= \tau a_1 - (i\kappa)^2 \alpha e^{-i\theta} a_1 = \left[\tau - \kappa^2 \alpha e^{-i\theta}\right] a_1 \end{aligned} \tag{3.19}$$

After *two* roundtrips, we have:

$$\begin{aligned} a_2 &= \tau a_1 - i\kappa b_1 \\ &= \tau a_1 - (i\kappa)\alpha e^{-i\theta} b_2 \\ &= \tau a_1 - (i\kappa)\alpha e^{-i\theta}(-i\kappa a_1 + \tau b_1) \\ &= \tau a_1 - (i\kappa)\alpha e^{-i\theta}(-i\kappa a_1 + \tau b_1) \\ &= \tau a_1 - \kappa^2 \alpha e^{-i\theta} a_1 - i\kappa\alpha\, e^{-i\theta} \tau b_1 \\ &= \tau a_1 - \kappa^2 \alpha e^{-i\theta} a_1 - i\kappa\tau\alpha\, e^{-i\theta} \alpha e^{-i\theta} b_2 \\ &= \tau a_1 - \kappa^2 \alpha e^{-i\theta} a_1 - i\kappa\tau\alpha^2 e^{-i2\theta}(-i\kappa) a_1 \\ &= \left[\tau - \kappa^2 \alpha e^{-i\theta} a_1 - \kappa^2 \tau\alpha^2 e^{-i2\theta}\right] a_1 \end{aligned} \tag{3.20}$$

Finally, after infinite roundtrips, we have:

$$\begin{aligned} a_2 &= \left[\tau - \kappa^2 \sum_{n-1}^{\infty} \tau^n \left(\alpha e^{-i\theta}\right)^n\right] a_1 \\ &= \frac{\tau - \alpha e^{-i\theta}}{1 - \tau\alpha e^{-i\theta}} a_1 \end{aligned} \tag{3.21}$$

And, the transmission of the ring resonator, $T(\theta)$ is given by:

$$T(\theta)=\left|\frac{a_2}{a_1}\right|^2=1-\frac{(1-\alpha^2)(1-\tau^2)}{(1-\alpha\tau)^2+4\alpha\tau\sin^2(\theta/2)} \tag{3.22}$$

Eqns. 3.21 and 3.22 will be handy in the analysis of the new modulator that we introduce in Section 4.

Also, if a voltage, V_0, is applied to an electro-optic (EO) RR, a phase shift θ is induced in the ring.[27] The magnitude of this phase shift is given by:

$$\theta=\theta_0+\Delta\beta L \tag{3.23}$$

where,

$$\Delta\beta=\frac{\pi n_0^3 r\Gamma V_0}{\lambda g} \tag{3.24}$$

Here, $\mathbf{n_0}$ is the index of refraction, **r** is the electro-optic coefficient, **λ** is the incident light wavelength, **g** is the electrode gap and **Γ** is the overlap integral. The output intensity is given by Eq. 3.22. Lastly, if the wavelength of the incident light wave is adjusted around the resonance (i.e. when $\theta=m\pi$), or the RR is properly voltage-biased, the output intensity is strongly modulated with a small modulated voltage.

If, instead of a DC voltage, a sinusoidal voltage, $V=V_0\sin\omega_m t$, is applied to the ring, then using the same approach that was used to derive Eq. 3.21, the output amplitude, $E_{out}(t)$ is given by:[31]

$$E_{out}(t)=\left[\tau-\kappa^2\sum_{n-1}^{\infty}\tau^{n-1}\alpha^n\exp\left[-i\left(n\theta+\delta_n\sin\left(\omega_m t-n\phi\right)\right)\right]\right]E_{in}(t) \tag{3.25}$$

where $\phi=\omega_m/FSR$ (ω_m is the modulation frequency and FSR is the free spectral range of the ring modulator) and δ_n is the modulation index. The modulation index depends on the electrode structure (we will discuss lumped and traveling wave configurations in Section 4 of this dissertation). For a lumped electrode, the modulation index is:[27]

$$\begin{aligned}\delta_n\sin\left(\omega_m t-n\phi\right)&=\int_0^{nL}\Delta\beta\sin\left[\omega_m\left(t+\frac{n_0}{c}z\right)-n\phi\right]dz\\&=\Delta\beta L\frac{\sin\left(n\phi/2\right)}{\phi/2}\sin\left(\omega_m t-{}^{n\phi}\!/_{2}\right)\end{aligned} \tag{3.26}$$

For a traveling wave electrode, the modulation index is given by:[27]

$$\begin{aligned}\delta_n\sin\left(\omega_m t-n\phi\right)&=\sum_{k=0}^{n-1}\int_0^{nL}\Delta\beta\sin\left[\omega_m\left(\left(t+kt_r\right)-\frac{\Delta n}{c}z\right)-n\phi\right]dz\\&=\Delta\beta L\frac{\sin\left(\psi/2\right)}{\psi/2}\frac{\sin\left(n\phi/2\right)}{\sin\left(\phi/2\right)}\sin\left(\omega_m t-\frac{\psi}{2}-\frac{n+1}{2}\phi\right)\end{aligned} \tag{3.27}$$

where $t_r={}^{n_0L}\!/_{c}$ is the optical round-trip time and $\psi={}^{\omega_m\Delta nL}\!/_{c}$ is the velocity matching factor. Here, $\Delta n=n_m-n_0$, where n_m is the microwave effective index and n_0 is the optical index. We further differentiate between lumped and traveling wave electrodes below.

3.6. Fundamentals of Mach-Zehnder Modulators

A typical external modulator is usually in the form of an integrated optical modulator, which includes a waveguide MZI that is fabricated on a slab of lithium niobate ($LiNbO_3$). Lithographic techniques – similar to those used in semiconductor manufacturing – are used to fabricate the waveguide. To ensure that light is channeled through the waveguide, the area is typically doped with impurities in order to increase the index of refraction.

In **Fig 3.5** below, light enters the modulator and splits into upper and lower arms. The light traversing the lower arm is modulated by a RF signal. Due to the electro-optic behavior of $LiNbO_3$, applying a voltage across the waveguide (via the electrodes) causes a change in its index of refraction. This induced change causes a phase delay in the light passing through the waveguide. The magnitude of the phase delay is proportional to the applied voltage.

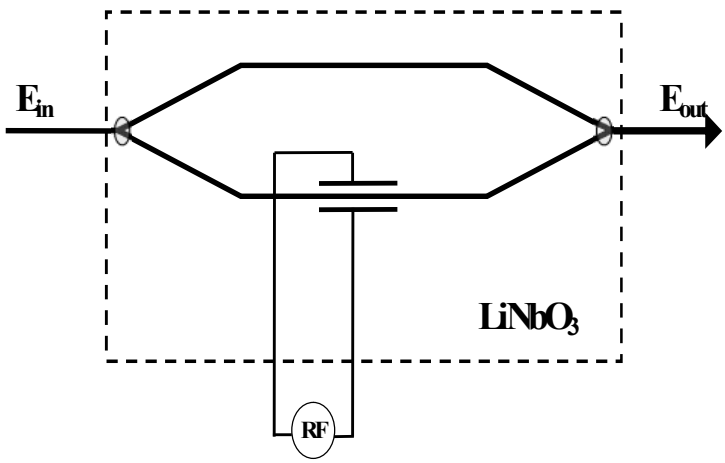

Figure 3.5: External modulation using Mach-Zehnder waveguide interferometer

The light traverses both arms of the interferometer and recombines either constructively or destructively at the other end. The induced phase shift in the lower arm of the interferometer is given by:

$$\Delta\theta = \pi \frac{V}{V_\pi} \tag{3.28}$$

where V is the voltage applied to the modulator and V_π is the half-wave voltage that, when applied, causes a phase shift of 180º. The transfer function of a MZ modulator is given by: [5, 14]

$$T_{MZ}(V) = \frac{1}{2}\left[1 + \cos\left(\pi \frac{V}{V_\pi} + \phi\right)\right] \tag{3.29}$$

where ϕ is the bias. Also, as discussed in Chang[14] and Tazawa[42] if this transfer function is expanded around a quadrature bias point $\phi = \pi/2$ (a standard operating point) we have:

$$T_{MZ}(V) \approx \frac{1}{2} + \frac{1}{2}\frac{\pi}{V_\pi}V - \frac{1}{12}\left(\frac{\pi}{V_\pi}\right)^3 V^3 + \frac{1}{240}\left(\frac{\pi}{V_\pi}\right)^5 V^5 - \ldots \tag{3.30}$$

We note that $T_{MZ}(V)$ contains no even-order terms, indicating that MZ only has odd order distortions. More importantly, the third order inter-modulation (IMD) terms, generated when two closely spaced RF frequencies are driving the modulator, cause the most difficulty, since the IM products tend to be very close to the fundamental signal.

Lithium niobate-based MZIs are common commercial off-the-shelf items that are used extensively in both CATV and telecommunication applications. In Section 4, we

compare the performance of these modulators to the new modulator that we introduce in this dissertation.

3.7. Ring Resonator-Assisted MZ Modulators

In **Fig 3.6** below, we illustrate a ring-resonator assisted MZ modulator (RAMZ). In the RAMZ design, a RR is coupled to a MZI. The coupling coefficients between the RR and the MZI are κ and τ. A modulating sinusoidal RF voltage is applied to the RR.

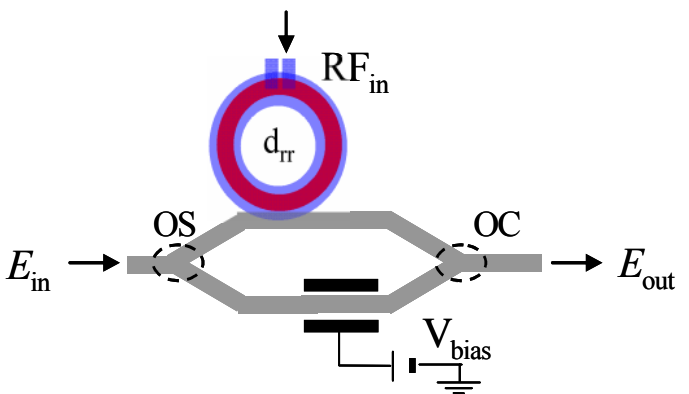

Figure 3.6: Schematic or a ring resonator-assisted MZ modulator (RAMZ)

To derive the transfer function of the RAMZ, we revisit equations 3.11 and 3.16 above. The transfer function of a RAMZ is:[32]

$$T_{RAMZ}(\theta) = \frac{1}{2}\left|\left[\frac{1}{\sqrt{2}}|a(\theta)|e^{-i\arg(a(\theta))} + \frac{1}{\sqrt{2}}e^{-i\phi}\right]\right| \tag{3.31}$$

$$a(\theta) = \frac{\tau - \alpha e^{-i\theta}}{1 - \alpha\tau e^{-i\theta}} \tag{3.32}$$

where ϕ is the DC phase bias between the two arms of the MZI and $a(\theta)$ is the amplitude transfer function of the RR. If the RR is lossless ($\alpha = 1$), $\tau = 2 - \sqrt{3}$ and $\phi = \pi/2$, then RAMZ becomes linearized around $\theta = \pi$ - which is off-resonance for the ring resonator.

3.8. SFDR definition and evaluation

The SFDR specification is widely used as the measure of linearity of a link system. It is defined as the difference between the largest signal that can be input into a system (with negligible distortion) and the smallest detectable noise-limited signal in the system. To evaluate the SFDR of a system we employ the commonly used 2-tone input frequency and analyze the fundamental and IMD output products.[32, 33, 34] If two closely spaced frequencies, f_1 and f_2 are simultaneously input into a non-linear system, non-linear interaction between these two signals creates new output frequencies. For example, in **Fig. 3.7** below, we see that 2nd order IMD output frequencies occur at f_1+f_2 and f_2-f_1. Second order harmonics occur at $2f_1$ and $2f_2$, and some 3rd order IMD outputs are seen at $2f_1-f_2$ and $2f_2-f_1$. Although other higher order IMD effects are also present, the most important and often most difficult to remove are the 3rd order effects (shown in **Fig. 3.7**). Some of these 3rd order outputs occur very close to the fundamental frequencies and are thus very difficult to filter out. Other higher order effects (e.g. 4th, 5th, etc.) are typically not problematic in narrow band applications, and therefore can be filtered away. However, they will usually be of some concern in broadband applications.

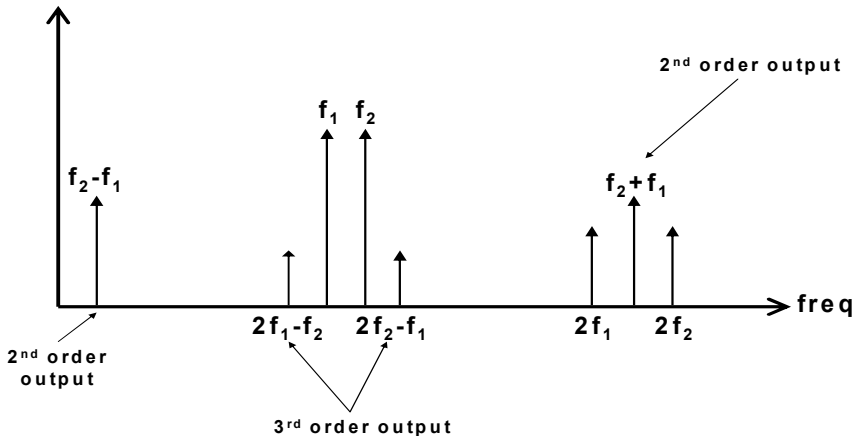

Figure 3.7: Spectrum of 2nd and 3rd order frequency outputs for a 2-tone input frequency

A graphical illustration of the calculation of SFDR is shown in **Fig. 3.8** below. SFDR is measured from the point where the intermodulation distortion (IMD) curve intersects the output noise floor power (P_{ONF}) to the corresponding point on the fundamental curve. It is an approach to determine SFDR, as discussed by Bridges et al.[33] As shown in **Fig. 3.8**, the fundamental curve has a slope of 1 in the linear region, and the 3rd order IMD curve has a slope of 3 in the linear region. Extending the linear slopes of these two curves cause them to intersect at the third order intercept point (IP3).

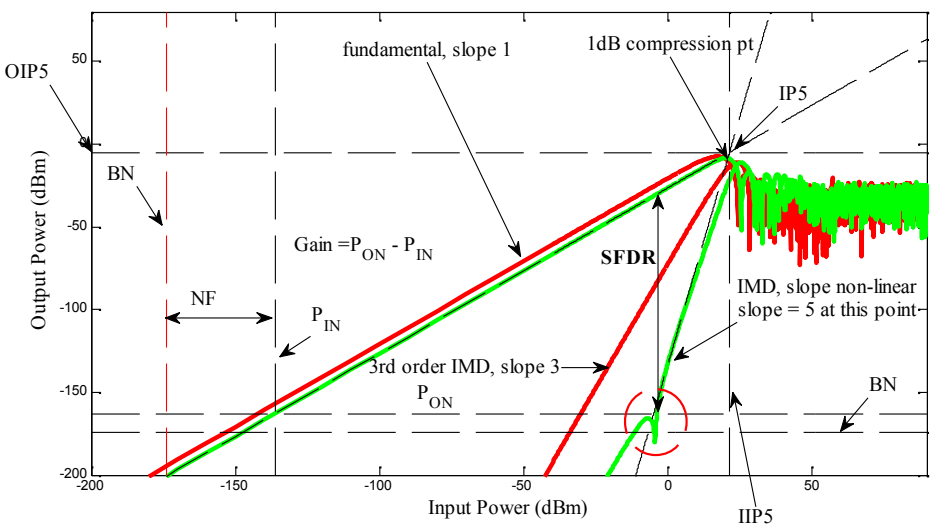

Figure 3.8: SFDR calculation and issues with non-linear IMD

3.9. Importance of Wide Linearized Bandwidth Capability

Wide linearized bandwidth capability is critical for many of the photonic applications mentioned above. SFDR performance is the commonly used indicator of the linearity of a system. Many systems are typically limited by third order intermodulation distortion (IMD). For a system limited by third order intermodulation distortion, SFDR is defined as two-thirds the difference between the largest distortion-less signal that can be input into the system and the smallest detectable signal in the system. The lower end of this range (the minimum discernable signal) is the sum of the output noise floor (P_{ONF}) and the system bandwidth, B.[32, 33, 34] The measurement bandwidth is assumed to be 1dB/Hz when defining the SFDR capability, so we also make that assumption here. Hence, for a system limited by 3rd order intermodulation, the SFDR is thus defined as:[33]

$$SFDR = \frac{2}{3}\left(OIP3 - P_{ON} - 10\log_{10}(B)\right) \tag{3.33}$$

where OIP3 is the output power at the 3rd order intercept point and B is the system bandwidth (with units Hz). In this case, the units of SFDR are $dB/Hz^{2/3}$. However, in the case of more linear systems that are limited by 5th order IMD, SFDR is defined as:[33]

$$SFDR = \frac{4}{5}\left(OIP5 - P_{ON} - 10\log_{10}(B)\right) \tag{3.34}$$

where OIP5 is the output power at the 5th order intercept point. And, the units of SFDR for a system limited by 5th order IMD are $dB/Hz^{4/5}$.

In both Eqns. 3.33 and 3.34, the IMD curve is assumed to be a straight line with a constant slope.[35] The graphical derivation of the formula for SFDR depends on the solution of simple geometry. However, in our previous discussions about the SFDR capability of our new modulator design, we noted that the intermodulation curve is nonlinear.[35] This is clearly seen in Fig. 3.8 above, in the circled region just below the output system noise level (P_{ON} – output noise floor), where the slope of an IMD curve increases beyond 5. So the generalized units of SFDR will be dB/Hz^x, where x is determined by the impact of the IMD curvature as it approaches the noise floor. More specifically, due to the curvature of the IMD curve in Fig. 3.8, x lies within the range $4/5 \leq x \leq 1$. Because of this complexity, we choose to report SFDR units in dB, with the knowledge that the explicit units are dB/Hz^x.

Other relevant parameters that are used to describe the performance of a link, include the background noise level (BN) = -174 dBm/Hz @ 25°C, the input system noise level (P_{IN}) with units dBm/Hz, the link gain (Gain =P_{ON}- P_{IN}) with units dB. Lastly, one of the main goals of this paper is to compare the performance of frequency-dependent IMPACC to that of frequency-dependent RAMZ. We investigate the SFDR performance as the modulation frequency varies. Additionally, for IMPACC we show that by changing our parameter controls (F and ξ_{pm}), we are able to inherently compensate for a potential reduction in SFDR with increased modulation frequency. This is critical, since as we mentioned above, large system bandwidth (large modulation frequency) applications require concurrently high SFDR capability.

3.10. Potential issues with the SFDR calculation

As we introduce the new modulator design below, we note that the IMD curve of this new modulator deviates slightly from a straight line just above $P_{ONF.}$ Therefore, the location of the n^{th} order intercept point (IP_n), in **Fig. 3.9** below, depends on the slope of the best linear fit of the IMD curve. Since this nonlinearity in the IMD curve is not taken into account in Eqns.3.33 and 3.34, the graphical approach (as shown in Fig. 3.9) is best suited to be used in calculating the SFDR for the new modulator. In this approach, the SFDR is simply defined as the difference between the fundamental and intermodulation output powers at the input power location where the IMD curve intersects the output noise floor (P_{ONF}).

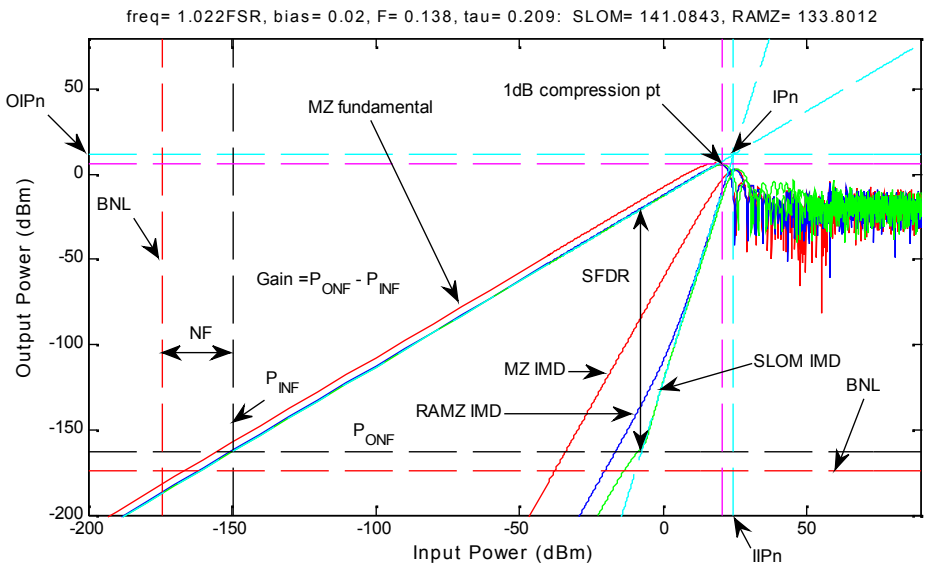

Figure 3.9: Important Parameters to describe System Link Performance

To fully investigate the linearity and bandwidth capability of the new modulator, we first consider a simplified design that makes use of lumped electrodes and operates at low modulation frequencies. Then we extend our analysis to a traveling wave electrode

design operating at higher modulation frequencies. This two-tiered analysis is a commonly applied technique[32, 33, 34] and we choose to also follow it here. But first, in Section 3.11, we briefly review the differences between a lumped electrode and a traveling wave electrode.

3.11. Electrode Configurations (Lumped vs. Traveling Wave)

In electronics, the lumped element assumes that each element is extremely small and that the connecting wires are perfect conductors. The major advantage of assuming a modulator with a lumped electrode design, in which the electrodes are assumed to be very short, is that it is easy to drive at low modulation frequencies.[36] At large modulation frequencies the lumped modulator becomes transit-time limited[27] - that is the transit time, t, becomes comparable to the modulation period, $2\pi/\omega_m$ (where ω_m is the modulation frequency). In fact, it is noted that the reduction in the modulation depth, ρ, for a lumped modulator due to the finite transit time is given by:[27]

$$\rho = \frac{\sin \frac{1}{2}\omega_m t}{\frac{1}{2}\omega_m t} \tag{3.35}$$

In Eq. 3.35, $t = nL/c$, where n is the index of refraction of the medium at the frequency of the optical signal and L is the modulator length. In order for there to be no reduction in modulation depth (i.e. $\rho = 1$), then $t << \frac{1}{\omega_m}$. In other words, the transit time has to be very small compared to the modulation period. Also, if the maximum practical

modulation frequency, $(\upsilon_m)_{\max}$, is assumed (for comparison to the traveling wave below) to occur at $\omega_m t = \pi$ (when $\rho = 0.64$), then using $t = nL/c$, we have:

$$(\upsilon_m)_{\max} = \frac{c}{2Ln} \tag{3.36}$$

Hence, one can increase the operation speed by further reducing the modulator length. However, a further reduction in the modulation length results in a reduced interaction between the optical signal and the externally-generated electric field. To counteract this reduced electro-optical coupling a higher modulating voltage will be required. Unfortunately, there is a trade off between higher operating speeds and using low driving voltage. In addition, it is very difficult to achieve impedance ($50\,\Omega$) matching between the source and the modulator.

To address the transit-time limitation of lumped electrodes, a traveling wave design is typically implemented. This configuration enables one to achieve larger bandwidth-capable modulators and the electrode is designed as a transmission line (**Fig 3.10**). In this case, the electrode is very long compared to the optical wavelength and the driving voltage requirements are much smaller.

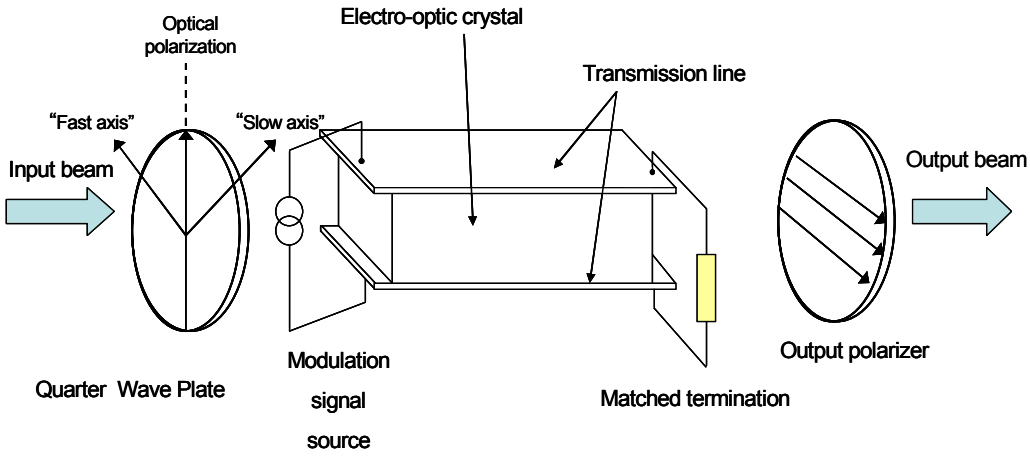

Figure 3.10: Representation of a Traveling Wave Electrode[27]

Also, if there is a velocity mismatch between the optical wave and the modulating wave (as is typical), then the transit time becomes $t = (n\text{-}n_m)L/c$, where n_m is the refractive index at the modulating frequency. This implies that the modulation frequency bandwidth capability increases. This is clearly seen as Eq. 3.36 is modified to:[27]

$$(\upsilon_m)_{\max} = \frac{c}{2L(n - n_m)} \tag{3.37}$$

So, after this brief review of the difference between lumped and traveling wave electrodes, we now discuss both designs in Section 4. We introduce the new optical modulator, in which we first assume that the modulator is lossless and that the electrodes in the PM and RR are lumped structures. We then extend the analysis to a traveling wave design in order to fully illustrate the large bandwidth capability of the modulator.

Chapter 4: Ultra Linear Modulator Analysis

4.1 Analytical Model: Formulation of IMPACC

The IMPACC design is based on a modified version of the Michelson Gires-Tournois Interferometer (MGTI) originally invented and used for optical filtering by Dingel *et. al*.[37] We have adapted this concept for external linearized optical modulator applications and in particular the high linearity (SFDR>130 dB $Hz^{2/3}$) with high manufacturing tolerance characteristic.

4.1.1. Modeling of IMPACC

The representative modulator design is shown in Fig. 4.1 where a PM and a RR are combined within a MZI structure. Both the PM and RR are driven by the same radio frequency (RF) input signal, which has been divided by an RF power splitter (PS) and fed onto their respective electrodes with a power split ratio of F**:(**1-F). The role of the RR is to provide the necessary optical phase correction onto the transmitted beam of one MZI arm without affecting its amplitude, and thus linearizing the modulator's response.

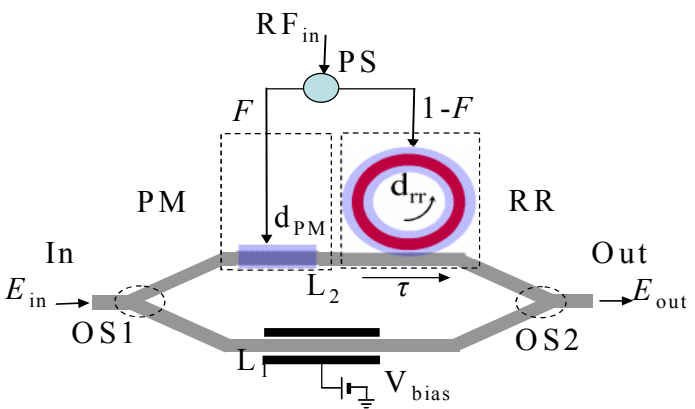

Figure 4.1: Schematic of IMPACC modulator consisting of a phase modulator (PM) and a ring resonator (RR) within a MZ configuration. (PS: RF power splitter, OS1: optical splitter, OS2: optical combiner).

The incoming optical signal is split into two beams of equal optical intensities by the optical splitter OS1. The first, of the two beams, propagates through the lower arm of the interferometer having length L_1. On the other hand, the second beam propagates through the upper arm of the interferometer having length L_2 and through the PM and RR, with lengths of d_{PM} and d_{RR}, respectively. In the upper interferometer arm, the PM and the RR are placed in series. The two beams, after having propagated through the associated arms, are combined coherently through combiner OS2 and produce the output electric field E_{out} described by:

$$E_{out} = \frac{E_o}{2} e^{-jknL_1} + \frac{E_o}{2} e^{-j\left(knL_2 + knd_{pm} + \Theta(\tau, d_{rr})\right)}, \tag{4.1}$$

where E_o is the optical field amplitude input to the modulator, $k \cdot n \cdot d_{pm}$ is the modulating phase term of the PM, n is the index of refraction, $d_{pm}=n \cdot d_0$ is the modulated length of the PM, and $\Theta(\tau, d_{rr})$ is the phase response of the RR.[37]

$$\Theta(\tau, d_{rr}) = -2\arctan\left[\frac{1-\tau}{1+\tau}\tan\left(\frac{knd_{rr}}{2}\right)\right], \tag{4.2}$$

where τ is the transmission coupling coefficient of the MZI arm, and d_{rr} is the circumference length of the RR.

For this particular implmentation of IMPACC, without the loss of generalities, we set d_{rr} to be twice as d_{pm}.

$$d_{rr} = 2\, d_{pm} \tag{4.3}$$

Also, note that for practical issues the RF power splitter (PS) can be variable. The intensity of the output optical signal can be calculated from:

$$I_{out} = \left| E_{out} \right|^2 , \tag{4.4}$$

By substituting Eq. (4.1) and Eq. (4.2) in Eq. (4.4) and using the trigonometric identities that give the relation between *sin* and *cos* to the exponential, we can arrive at the following expression:

$$I_{out} = \frac{{E_o}^2}{2} \left\{ 1 + \cos\left[kn(L_1 - L_2) - (knd_{pm} + \Theta(\tau, d_{rr})) \right] \right\}, \tag{4.5}$$

We can rearrange Eq. (4.5) in a more convenient form using trigonometric identites and since it is desirable to operate the modulator at the inflection point where second-order intermodulation distortion (IMD) is zero, we set

$$kn\,(L_1 - L_2) = (2m - 1)\frac{\pi}{2} \tag{4.6}$$

Hence Eq. (4.5) changes to:

$$I_{out} = \frac{{E_o}^2}{2} \left\{ 1 + \sin\left[knd_{pm} + \Theta(\tau, d_{rr}) \right] \right\} \tag{4.7}$$

Taking into account the parameter factor F (for the RF split ratio) in Eq. (4.7) and using Eq. 4.2, we obtain

$$TF = \frac{I_{out}}{P_{laser}} = \frac{1}{2}\left\{1 + \sin\left[a\sqrt{F} - 2\arctan\left[T\tan\left(a\sqrt{1-F}\right)\right]\right]\right\} \tag{4.8}$$

where TF is the lossless transfer function, $P_{\text{laser}}=I_{\text{o}}=|E_{\text{o}}|^2$ is the laser output optical power, τ is the transmission coupling coefficient, and the terms T and a are given[38] as:

$$T = \frac{1-\tau}{1+\tau}, \tag{4.9}$$

$$a = knd_{pm} \tag{4.10}$$

Note that in this approach we have assumed that the phase difference between the two RF signals driving the PM and the RR is zero or $2\pi m$. Fig. 4.2 shows some of the possible transfer functions, described by Eq. (4.8), obtained for different parameter choices of F and τ. The optical bias phase shift for IMPACC had to be adjusted since for low values of F the RR dominates the PM. Here, we note for the first time that these transfer functions suggest the possibility of an optical modulator with programmable linearity.

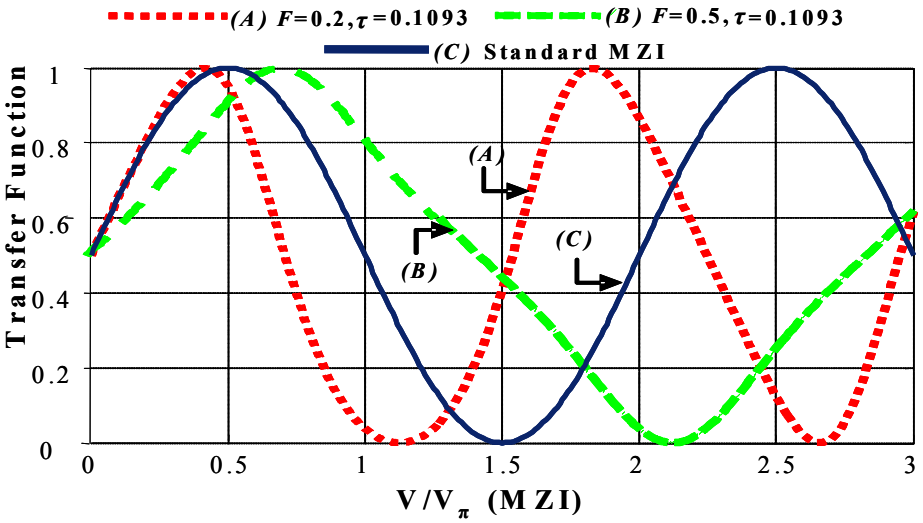

Figure 4.2: Transfer functions of the IMPACC for different F, τ parameters. The linearity of the transfer function highly depends on the choice of the parameters.

Eq. (4.8) can be simplified through some additional trigonometry applied to the sin[·] term within the brackets of Eq. (4.8). Hence, we can rewrite the sin[·] as

$$\sin[\cdot] = \frac{C_1 \sin A + C_2 \sin(A-2B) + C_3 \sin(A+2B)}{1 + C_4 \sin^2 B}, \tag{4.11}$$

Where the C_m (m=1, 2, 3, 4) factors are functions of the transmission coupling coeficient T, and are given by the following expressions:

$$C_1 = \frac{1-T^2}{2} \tag{4.12}$$

$$C_2 = \left(\frac{1-T}{2}\right)^2 \tag{4.13}$$

$$C_3 = \left(\frac{1+T}{2}\right)^2 \tag{4.14}$$

$$C_4 = T^2 - 1 \tag{4.15}$$

and the factors A, and B are expressed as:

$$A = a\sqrt{F} = knd_{pm}\sqrt{F}\ , \tag{4.16}$$

$$B = a\sqrt{1-F} = knd_{pm}\sqrt{1-F}\ . \tag{4.17}$$

Eq. (11) can be expanded further by using the Taylor expansion

$$\frac{1}{1+x} = 1 - x + x^2 - x^3 + x^4 - \ldots \tag{4.18}$$

with the assumption that x <<1. Keeping up to four terms of the expansion (i.e., x^4), and performing the multiplications, rearranging the equations and simplifying it by factoring common terms, we arrive at an expression for sin[·]:

$$\sin[\cdot] = Q_1 \sin A + \sum_{m=1}^{5}\left[Q_{2m}\sin(A + 2mB) + Q_{2m+1}\sin(A - 2mB)\right] \tag{4.19}$$

where the Q terms are functions of C_1, C_2, C_3 and C_4 parameters.

4.1.2. Linearity of IMPACC

In order to study the linearity of IMPACC, and in particular the SFDR performance as a function of the F and τ parameters, we use the well-known two-tone test.[39] For the two tone test we can write Eq. (4.10) as:

$$a = \pi \frac{V}{V_\pi} \left[\sin(\omega_1 t) + \sin(\omega_2 t) \right], \tag{4.20}$$

where V is the amplitude of the two-tone modulating voltage, ω_1 and ω_2 are the two-tone RF frequencies. Using trigonometric as well as Bessel function identities, Eq. (4.19) can reduce to a form that includes the fundamental signal, odd harmonics, and the intermodulation (IM) products. Hence, Eq. (4.19) changes to

$$\begin{aligned} \sin[\cdot] = {} & Q_1 \sin\left[\pi \frac{V}{V_\pi} \sqrt{F} \left[\sin(\omega_1 t) + \sin(\omega_2 t) \right] \right] + \\ & + \sum_{m=1}^{5} Q_{2i} \sin\left[\pi \frac{V}{V_\pi} \left(\sqrt{F} + 2m\sqrt{1-F} \right) \left[\sin(\omega_1 t) + \sin(\omega_2 t) \right] \right] + \\ & + \sum_{m=1}^{5} Q_{2i+1} \sin\left[\pi \frac{V}{V_\pi} \left(\sqrt{F} - 2m\sqrt{1-F} \right) \left[\sin(\omega_1 t) + \sin(\omega_2 t) \right] \right] \end{aligned} \tag{4.21}$$

We can further expand the individual terms of Eq. (4.21) using the trigonometric identity

$$\sin(z_1 + z_2) = \sin z_1 \cos z_2 + \cos z_1 \sin z_2, \tag{4.22}$$

or in our case:

$$\sin\left[M\left(\sin\omega_1 t+\sin\omega_2 t\right)\right]=\sin(M\sin\omega_1 t)\cos(M\sin\omega_2 t)+ \\ +\cos(M\sin\omega_1 t)\sin(M\sin\omega_2 t), \tag{4.23}$$

where M is the multiplicative factor within the argument of the *sin* that is a function of V_π and F. Then, we further simplify Eq. (4.21) with the help of the trigonometric to Bessel function transformations,

$$\sin(x\sin\theta)=2\sum_{n=1}^{\infty}J_{2n-1}(x)\sin\left[(2n-1)\theta\right], \tag{4.24}$$

$$\cos(x\sin\theta)=J_o(x)+2\sum_{n=1}^{\infty}J_{2n}(x)\cos(2n\theta), \tag{4.25}$$

where J_n is the Bessel function of the first type. Eq. (4.21) can be rewritten as a function of these Bessel functions by factoring common terms and keeping Bessel function order up to n=2. The terms can be separated into terms that describe the fundamental (*FUND*) and the *IMD* (IM distortion) terms. From the *IMD* terms, the important ones are the $2\omega_1$-ω_2 and $2\omega_2$-ω_1 (see appendix). Hence the output optical intensity can be expressed as the superposition of a DC term and the *FUND* and the *IMD* terms, where the *FUND* and *IMD* terms are described by:

$$
\begin{aligned}
FUND &= \mathrm{Q}_1 \cdot 2 \cdot \mathrm{J}_o\left(\alpha\sqrt{\mathrm{F}}\right) \cdot \mathrm{J}_1\left(\alpha\sqrt{\mathrm{F}}\right) + \\
&+ \sum_{m=1}^{5} Q_{2i} \cdot 2 \cdot \mathrm{J}_o\left[\alpha\left(\sqrt{\mathrm{F}} + 2m\sqrt{1-\mathrm{F}}\right)\right] \cdot \mathrm{J}_1\left[\alpha\left(\sqrt{\mathrm{F}} + 2m\sqrt{1-\mathrm{F}}\right)\right] + \\
&+ \sum_{m=1}^{5} Q_{2i+1} \cdot 2 \cdot \mathrm{J}_o\left[\alpha\left(\sqrt{\mathrm{F}} - 2m\sqrt{1-\mathrm{F}}\right)\right] \cdot \mathrm{J}_1\left[\alpha\left(\sqrt{\mathrm{F}} - 2m\sqrt{1-\mathrm{F}}\right)\right]
\end{aligned}
\tag{4.26}
$$

$$
\begin{aligned}
IMD &= \mathrm{Q}_1 \cdot 2 \cdot \mathrm{J}_1\left(\alpha\sqrt{\mathrm{F}}\right) \cdot \mathrm{J}_2\left(\alpha\sqrt{\mathrm{F}}\right) + \\
&+ \sum_{m=1}^{5} Q_{2i} \cdot 2 \cdot \mathrm{J}_1\left[\alpha\left(\sqrt{\mathrm{F}} + 2m\sqrt{1-\mathrm{F}}\right)\right] \cdot \mathrm{J}_2\left[\alpha\left(\sqrt{\mathrm{F}} + 2m\sqrt{1-\mathrm{F}}\right)\right] + \\
&+ \sum_{m=1}^{5} Q_{2i+1} \cdot 2 \cdot \mathrm{J}_1\left[\alpha\left(\sqrt{\mathrm{F}} - 2m\sqrt{1-\mathrm{F}}\right)\right] \cdot \mathrm{J}_2\left[\alpha\left(\sqrt{\mathrm{F}} - 2m\sqrt{1-\mathrm{F}}\right)\right]
\end{aligned}
\tag{4.27}
$$

with $\alpha=\pi\cdot V/V_\pi$. The RF output power from the photodetector[40] is then given by:

$$
P_{RF-out} = \frac{1}{2} \cdot \left\langle i_D{}^2 \right\rangle \cdot R_D \tag{4.28}
$$

where i_D is the detector photocurrent and R_D is the effective load impedance of the detector. Eq. 4.28 expresses the conversion of the detector photocurrent to electrical power. When this detector is connected to a resistive load, R_D is the load resistance. The photocurrent is related to the fiber-to-fiber optical insertion loss (IL) of the modulator-to-detector link that is expressed as the product of the lossless TF, the laser output power (P_{laser}), the link insertion loss (l), in linear terms ($l=10^{-\text{IL[dB]}/10}$), and the detector responsivity (r_D).

$$i_D = l \cdot P_{laser} \cdot TF \cdot r_D \,, \tag{4.29}$$

Substituting Eq. 4.29 in Eq. 4.28 and taking into acount Eq's 4.26 and 4.27, we can calculate the RF output power for the fundamental and third order intermodulation terms.

$$P_{RF-FUND} = \frac{1}{8} l^2 \cdot {P_{laser}}^2 \cdot {r_D}^2 \cdot FUND^2 \cdot R_D \,, \tag{4.30}$$

$$P_{RF-IMD} = \frac{1}{8} l^2 \cdot {P_{laser}}^2 \cdot {r_D}^2 \cdot IMD^2 \cdot R_D \,. \tag{4.31}$$

We will use these RF powers to characterize the SFDR performance of the FO-link and in particular the IMPACC in comparison to a standard MZM.

4.1.3. Reduction to RAMZI and MZI

One of the powerful advantages of the formulation is that it can be used to describe other modulator designs. Here we will show that IMPACC can be reduced easily to the RAMZI design and the standard MZI modulator under certain conditions. These conditions depend on two parameters, namely (1) F and (2) τ.

4.1.3.1 IMPACC to RAMZI

In order to reduce IMPACC to a conventional RAMZI, we need to set the value of $F = 0$ so that no RF power is directed into the PM and parameter τ is set to $2 - \sqrt{3}$.[34] The transfer function in Eq. 4.8 then reduces to

$$TF = \frac{I_{out}}{P_{laser}} = \frac{1}{2}\left\{1 + \sin\left[-2\arctan\left[\frac{3-\sqrt{3}}{\sqrt{3}-1}\tan(a)\right]\right]\right\} \tag{4.32}$$

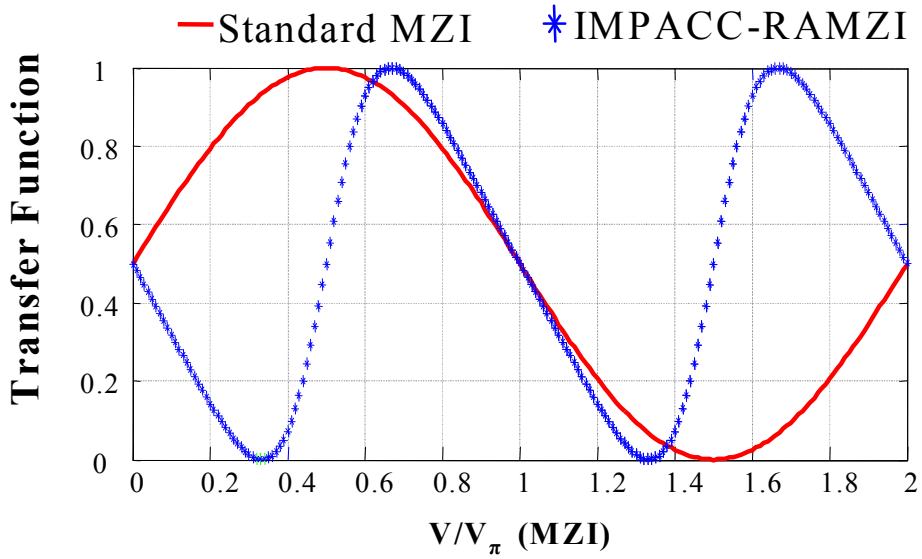

Figure 4.3: Transfer function profile of IMPACC under the RAMZI condition

In Fig.4.3, we note first, the frequency of IMPACC-RAMZI is shifted by π radians compared to Standard MZI. Second, IMPACC-RAMZI also has twice the frequency of the Standard MZI because of our initial assumption in Eq. 4.3. That is the RR circumference is twice the length of the PM. Lastly, the effective value of the V_π is smaller than the standard modulator. Further discussion and comparison of the SFDR values between RAMZI, MZM and IMPACC is given in the next section.

4.1.1.1 IMPACC to Standard MZI

Reducing IMPACC to standard MZI can be accomplished in two ways. In the first appraoch, the value of *F* is set to 1 so that all RF power is directed into the PM and

parameter τ is set to 1 so that no optical power is coupled into the RR. Under these conditions, Eqn. (8) reduces to the following sinusoidal expression:

$$TF = \frac{I_{out}}{P_{laser}} = \frac{1}{2}\{1 + \sin[a]\}. \tag{4.33}$$

It resembles very much the case of standard MZI, as shown in Fig. 4.4 (IMPACC-MZI(a))

In the second approach, we set the value of F = 0 and τ = 0. This will direct all RF power to the RR but the optical beam in the L2 arm will circulate or propagate to the RR only once. Hence, the RR functions as plain phase modulator. The resultant transfer function is another sinusuidal expression given as:

$$TF = \frac{I_{out}}{P_{laser}} = \frac{1}{2}\{1 + \sin[-2a]\}, \tag{4.34}$$

and labeled as IMPACC-MZI(b) in Fig. 4.4. We note that the transfer function in Eq. 4.34 has twice the frequency of that in Eq. 4.33 and is shifted by π radians. This is expected, since we have initially set the condition that $d_{rr} = 2d_{pm}$ as stated in Eqn. 4.3.

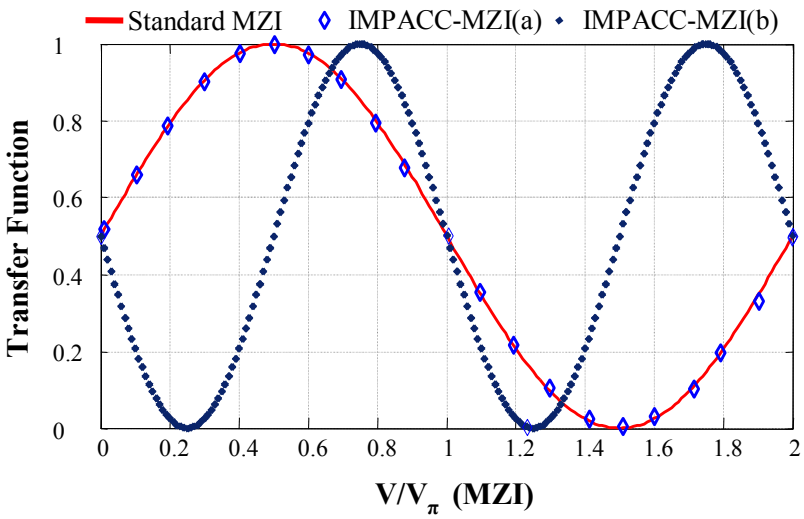

Figure 4.4: Transfer function profiles of IMPACC under the MZI conditions

4.2. IMPACC (Lumped Electrode Design)

Whereas in Section 4.1 we introduced the analytical formulation of IMPACC, with the assumption of ideal electrodes, here we develop a numerical approach to simulate the performance of IMPACC. With this approach, we investigate the bandwidth performance of IMPACC, and have the flexibility to account for non-ideal conditions, such as waveguide losses.

4.2.1 Phase Response and Linearity Performance of IMPACC

The design of the super linear modulator that we discuss in this Section is shown in **Fig 4.5** below. The modulator consists of a ring resonator (RR) and a phase modulator (PM) arranged parallel to each other in a Mach Zehnder interferometer (MZI) configuration. An external radio frequency (RF) delay line and a bias control are also present in this configuration. As previously reported[20 21] an RF input is divided by a

power splitter (PS) into a power split ratio F:1-F and channeled to the electrodes of the PM and RR. The relative phases of the RF inputs into the phase modulator and ring resonator are also controlled by the external RF delay line.

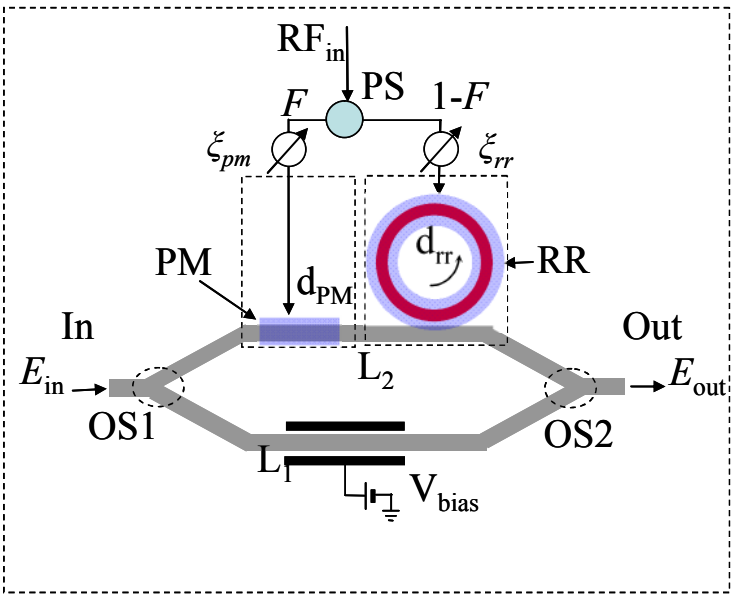

Figure 4.5: Design of Super Linear Modulator, consisting of a PM and RR in a MZI

As seen in **Fig. 4.5** an incident electric field (E_{in}) is split into two beams of equal intensities. One of the beams propagates in the upper arm of length L_1, which contains a bias control and a PM. The other beam propagates in the lower arm of length L_2, which contains a RR with coupling coefficients κ and τ. The RF input signal is also divided into two parts by an external RF power splitter **(PS)** with power ratio **(1-*F*:*F*)** before they are injected into RR and PM electrodes, respectively. These RF signals are delayed by an amount ξ_{rr} and ξ_{pm} using external tunable RF delay lines or phase shifters.

The two light beams combine to give an output field E_{out}. To minimize 2nd order intermodulation distortion (IMD), we set $kn_0(L_1 - L_2) = (m-1)\pi/2$. The transfer function of the device, $T_N(\theta)$ and its embedded functions are defined as:

$$T_N(\theta) = \tfrac{1}{2}\left|\tfrac{1}{\sqrt{2}}\left|a(\theta_{rr})\right|e^{-i\arg(a(\theta_{rr}))} + \tfrac{1}{\sqrt{2}}e^{-i(\varphi+\theta_{pm})}\right|^2 \tag{4.35}$$

$$a(\theta_{rr}) = \tau - \kappa^2 \sum_{n=1}^{\infty} \tau^{n-1}\alpha^n \exp[-i\theta_{rr}] \tag{4.36}$$

$$\theta_{rr} = n\left(kn_0 d_{rr}\right) + \sqrt{1-F}\,\delta_n \sin\left(\omega_m t - n\phi\right) \tag{4.37}$$

$$\delta_n \sin(\omega_m t - n\phi) = \Delta\beta d_{rr} \frac{\sin\left(\frac{n\phi}{2}\right)}{\frac{\phi}{2}} \sin\left(\omega_m t - \frac{n\phi}{2} + \xi_{rr}\right) \tag{4.38}$$

$$\theta_{pm} = kn_0 d_{pm} + \sqrt{F}\,\Delta\beta d_{pm} \frac{\sin\left(\frac{\phi}{2}\right)}{\frac{\phi}{2}} \sin\left(\omega_m t - \frac{\phi}{2} + \xi_{pm}\right) \tag{4.39}$$

$$\Delta\beta = \frac{\pi n_0^3 r \Gamma V_0}{\lambda g} \tag{4.40}$$

Here, $\mathbf{n_0}$ is the index of refraction, **k** is propagation constant, $\boldsymbol{\theta_{pm}}$ and **arg(** a($\boldsymbol{\theta_{rr}}$) **)** are phase responses of the PM and RR respectively, $\mathbf{d_{pm}}$ and $\mathbf{d_{rr}}$ are lengths of the PM and RR, respectively, **n** is the number of times the beam propagates inside the RR, α_n is the waveguide loss factor, $\boldsymbol{\delta_n}$ is the modulation index, $\boldsymbol{\omega_m}$ is the modulation frequency, $\phi = \omega_m / FSR$ is the normalized modulation frequency, **r** is the electro-optic coefficient, $\mathbf{V_0}$ is the voltage amplitude, **λ** is the incident light wavelength, **g** is the electrode gap, **Γ** is the overlap integral[41] (See Eq. A.1 in the Appendix for explicit form of **Γ**), and **φ** is an

optical bias phase. We note that when F=0 and F=1, this modulator reduces to RAMZ and standard MZ, respectively.

Eq. 4.36 is the complex amplitude response of the RR that takes into account the multiple propagation of the beam inside the ring[22], with an input parameter given by Eq.4.37. The first term in Eq. 4.37 represents the static phase due to the fixed length of the RR, while the second term is the phase change due to RF power with DC component. The third term describes the dynamic phase change due to RF power with AC components under a lumped electrode structure defined by Eq. 4.38. The phase response of the PM is given by Eq. 4.39 and has a similar interpretation as in Eq. 4.37, except for a particular length d_{pm}, n=1, and RF phase term ξ_{pm}.

After the transfer function is derived, the next step is to calculate the fundamental and intermodulation signal output powers, given pre-defined input parameters. The fundamental output signal power, P_{Fund} is given by:[42]

$$P_{Fund} = \left| \frac{P_L L_0 n_D R_D}{T} \int_0^T T_N \exp(-2\pi i f_1 t) dt \right|^2 \tag{4.41}$$

The second order intermodulation distortion output power is given by:[42]

$$P_{IM2} = \left| \frac{P_L L_0 n_D R_D}{T} \int_0^T T_N \exp\left[-2\pi i (2f_1) t\right] dt \right|^2 \tag{4.42}$$

And the third order intermodulation distortion output power is given by:[42]

$$P_{IM3} = \left| \frac{P_L L_0 n_D R_D}{T} \int_0^T T_N \exp\left[-2\pi i (2f_1 - f_2) t\right] dt \right|^2 \tag{4.43}$$

where P_L is the laser input power, L_0 is the total optical loss, n_D is the detector sensitivity, R_D is the detector impedance and T is the period.

To investigate the linearity, we choose specific values of F and τ and compare IMPACC's SFDR to both SFDRs of MZ and RAMZ. **Fig. 4.6** below shows the calculated SFDRs of IMPACC with (F,τ)= (0.009, 0.195), RAMZ with τ= 0.278[22 23], and standard MZ at relatively low normalized modulation frequencies (norm. to FSR of RR).

IMPACC provides a large SFDR (>**132.6** dB) which is >21.5 dB higher than MZ and >3.4 dB higher than RAMZ. As the inset in **Fig. 4.6** shows, this is primarily due to the shift of IMPACC's IMD curve to the right. Furthermore, the link gain of IMPACC is comparable to RAMZ (~-30dB) at relatively low frequencies.

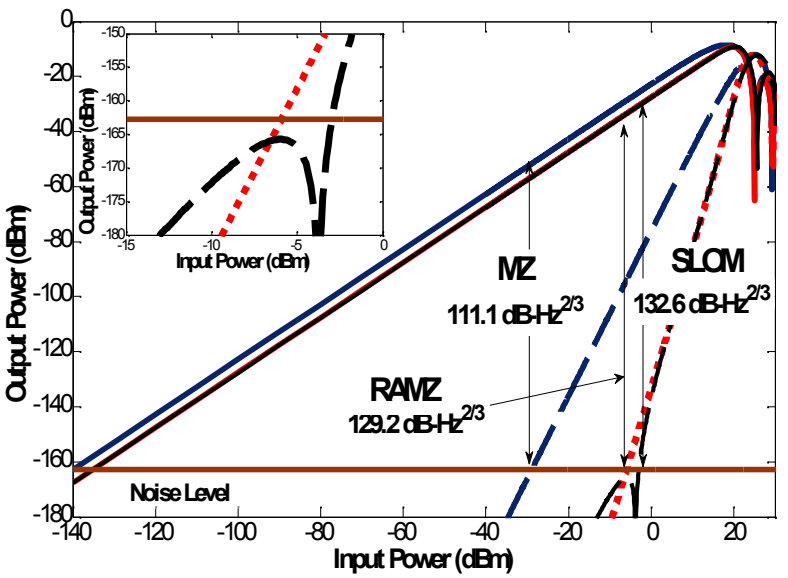

Figure 4.6: SFDR comparison of IMPACC vs. MZ and RAMZ for $\omega_m = 10^{-5}$ FSR and (F,τ) = (0.009, 0.195)

4.2.2 Method to Select (F,τ) values that Generate High SFDR Values

Selecting (F, τ) nodes that result in high SFDR values can be computationally intensive. One method to identify regions with high SFDR includes mapping a 2-dimensional space with relatively low resolution, in order to identify suitable regions that will generate high SFDR values.[21] Since the SFDR values range from very low (below 100dB) to high (>120dB) the contour plots in **Figs 4.7a** and **4.7b** below only show SFDR values that are greater than 100 dB.

After these regions are identified, using a higher resolution in the identified regions will clearly identify the high SFDR regions. For example, **Fig 4.7a** shows a contour map of SFDR values in the entire (F, τ) space with a 0.01 step size on both axes. Regions of interest (where high SFDR values are observed) are then identified. One such region is marked in **Fig 4.7a**. In **Fig 4.7b**, resolution steps of 0.0001 are used to more clearly identify the high SFDR values in the region of interest.

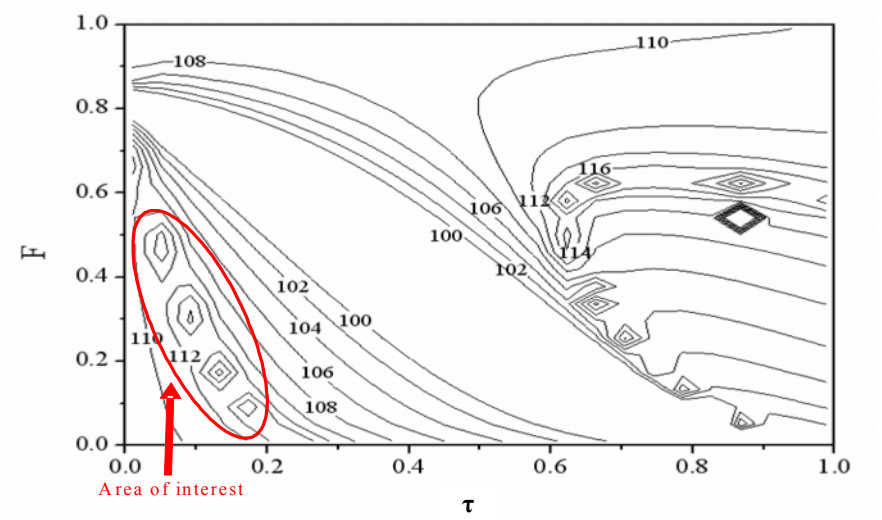

Figure 4.7a: Contour plot of SFDR in (F,τ) space

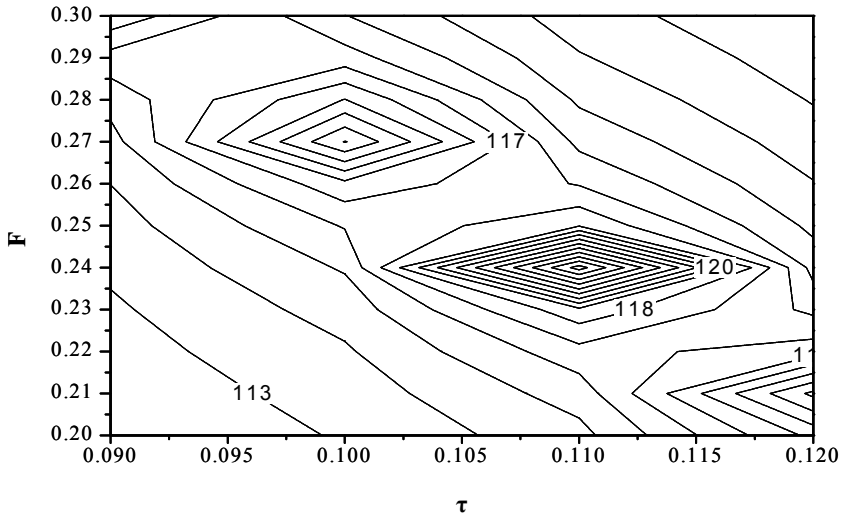

Figure 4.7b: SFDR values in Area of Interest

4.2.3 Bandwidth of IMPACC (Lumped Electrode)

Fig. 4.8 shows the calculated modulation frequency dependence of the dynamic range (SFDR) for IMPACC, RAMZ, and MZ. It illustrates the modulation bandwidth enhancement, which is another important attribute of IMPACC. The DR of an ideal MZ is frequency independent and is capped at 111.2 dB. From **Fig. 4.8**, we can observe three important characteristics. First, the DR of both IMPACC and RAMZ decrease as the modulation frequency increases. However, the SFDR of IMPACC is always ~1-5dB (or 25-350%) greater than that of RAMZ up to 0.35 FSR.

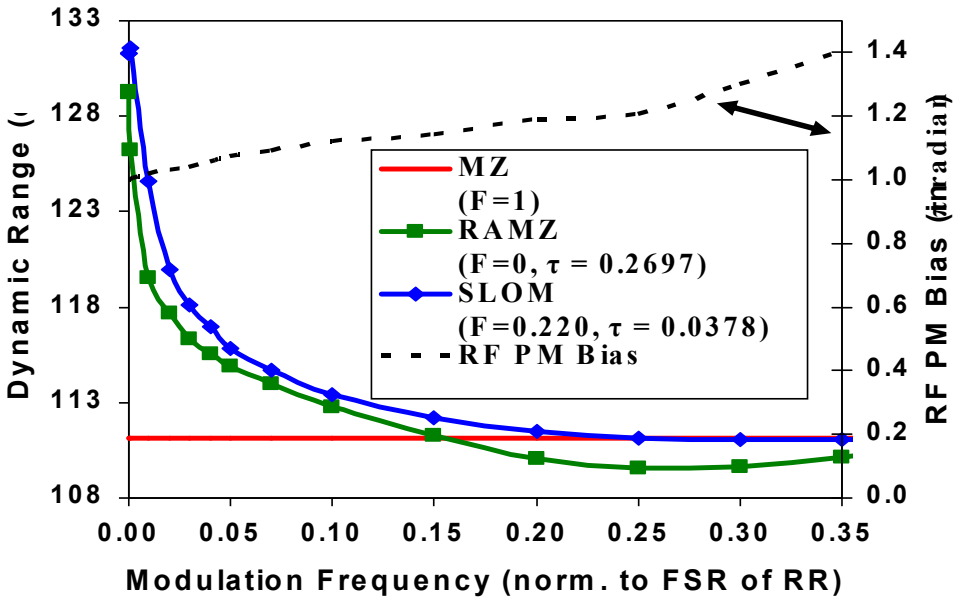

Figure 4.8: Frequency dependence of SFDR for IMPACC (F,τ,) =(0.22, 0.038) compared to RAMZ and MZ.

Second, if we define the "effective linearization bandwidth" of any resonator-based modulators as the point where the DR equals the DR of an ideal MZ, then we can see that RAMZ is basically limited to **0.15 FSR**. And, compared with RAMZ, IMPACC's effective bandwidth range is at least 70% as wide (**0.25 FSR vs. 0.15 FSR**). It is important to note here that this increased linearization bandwidth is accomplished without resorting to a smaller ring circumference. Note that a RAMZ design with smaller RR circumference brings negative consequences, such as: higher V_π value, lower link gain, and increased cost due to added amplifiers.

The SFDR performance improvement in IMPACC is obtained by selecting the optimum ξ_{pm} (with ξ_{rr}=0) value for a given frequency (top right of **Fig. 4.8)**. Detailed effects of the different values of ξ_{pm} on IMD at frequency (= 10^{-3} FSR) is shown in **Fig. 4.9**. When ξ_{pm} is increased from 1.0π to 1.01π, the IMD signal is shifted to the right side and leads to a powerful 5.8 dB improvement on SFDR (=132.0 dB).

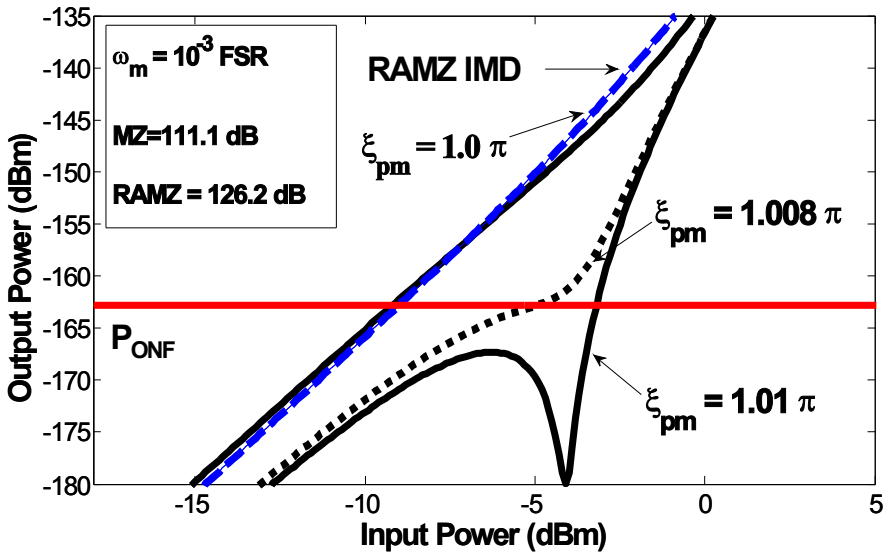

Figure 4.9: Effect of RF Phase ξ_{pm} on the IMD for $\omega_m = 10^{-3}$ FSR and (F,τ) = (0.009, 0.195)

The RF phase ξ_{pm} compensates the deterioration on IMD for increasing modulation frequencies. Besides its performance advantages, this technique is also rather inexpensive and offers flexible control since it is external to the chip. Lastly, we observe in **Fig. 4.8** that as the modulation frequency increases beyond the "effective bandwidth range", the SFDR of RAMZ becomes inferior compared with standard MZ. In the case of IMPACC, its SFDR saturates to the level of MZ but never goes lower.

In all these calculations, we used parameters that are employed in RAMZ calculations and found in many publications[28, 42] for ease of comparison (**Table 4.1**). These calculations were computed with an insertion loss (IL) of 10dB. If the IL can be reduced by 3dB to 7 dB, IMPACC's SFDR increases from ~133dB to ~140dB.

Table 4.1: Commonly used Link Parameter Values

Parameter	Value	Unit
Laser input power (P_L)	100	mW
Relative Intensity Noise (RIN)	-162.8	dB/Hz
Insertion Loss (IL)	10	dB
Half wave voltage (V_π)	5	V
Modulator Impedance(R_M)	50	Ω
Detector Responsivity(η_D)	0.7	A/W
Detective Impedance(R_D)	50	Ω
Maximum Current (P_L)	7	mA

We chose to set $kn_0(L_1 - L_2) = (m-1)\pi/2$ in order to minimize 2^{nd} order intermodulation distortion. We also note that when F=0, this design reduces to a ring resonator-assisted Mach Zehnder (RAMZ). In this case, all the power is transmitted to the ring resonator. Also, when F=1 this design reduces to a standard MZ. Additionally, the ability to vary F and the RF delay allows for dynamic compensation capability. In the analysis to follow, we demonstrate various characteristics of this novel design, including linearity, bandwidth capability and more tolerance allowance during manufacturing.

And, as mentioned earlier, the lumped electrode design is limited to low modulation frequencies. So in the next section, we extend the discussion to the traveling wave design and report the resulting bandwidth and linearity performance.

4.3 IMPACC (Traveling Wave Electrode Design)

4.3.1 Modified Phase Responses of Traveling Wave Design

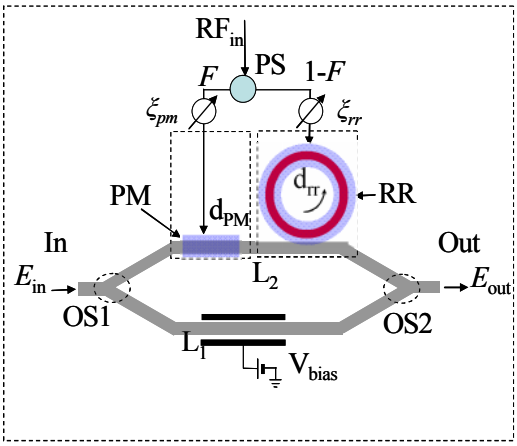

Figure 4.10a: Traveling Wave IMPACC

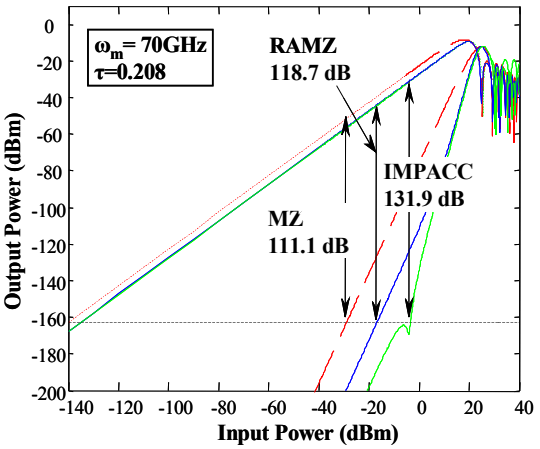

Fig. 4.10b: IMPACC's vs. RAMZ's SFDR

Fig. 4.10a shows the design of the super linear optical modulator (IMPACC), but in this case we assume a traveling wave electrode design. **Fig. 4.10b** illustrates the calculated SFDR values of the traveling wave IMPACC, RAMZ and MZ at a large modulation frequency (>70GHz). IMPACC achieves a superior SFDR value (131.9 dB) compared with RAMZ (118.7 dB) and MZ (111.1 dB) even at these high frequencies The SFDR calculation for the traveling wave modulator requires the modified phase responses (compare to Eqns. 4.37-4.39) of the ring resonator and phase modulator, which are defined below:

$$\theta_{rr} = n\left(kn_0 d_{rr}\right) + \sqrt{1-F}\,\Delta\beta d_{rr}\,\frac{\sin\left(n\phi/2\right)}{\sin\left(\phi/2\right)}\sin\left(\omega_m t + \xi_{rr} - \frac{(n+1)\phi}{2}\right) \tag{4.44}$$

$$\theta_{pm} = kn_0 d_{pm} + \sqrt{F}\Delta\beta d_{pm}\sin\left(\omega_m t + \xi_{pm} - \phi\right) \tag{4.45}$$

After the traveling wave transfer function is derived, we calculate the fundamental and intermodulation signal output powers, using Eqns. 4.41 - 4.43. For ease of discussion, we assume that there is negligible microwave loss and no velocity mismatch. However, microwave loss and velocity mismatch are also bandwidth limiting factors, and have been reported on.[34] In future work, we will include these factors and discuss the implication for material property requirements.

4.3.2 Optimizing the Performance of Traveling Wave IMPACC

The excellent linearity of IMPACC, shown in **Fig. 4.10b,** is a direct result of optimizing the parameters F and ξ_{pm}. Besides its performance advantages, this optimization technique is also very inexpensive and offers flexible and practical control since it is external to the chip. Varying F and the RF phase term, ξ_{pm} at each modulation frequency (with ξ_{rr}=0) compensates the deterioration on the intermodulation distortion (IMD) signal.

Fig. 4.11a shows the effect on IMD signal when F is increased for fixed parameters τ and ξ_{pm}. It causes the IMD curve to shift to the right, which leads to a higher SFDR value. The calculated SFDR is typically maximized when the hump on the IMD curve is just below the Noise Level. For the case shown in **Fig. 4.11a**, with τ=0.208, ω_m=70.0 GHz, and a particular RF phase (ξ_{pm}=1.96π rad), the SFDR value is maximized at F=0.0086 (SFDR=131.9dB). Note that a small change in F can result in significant change in the SFDR value over the narrow BW regions where SFDR is high. Outside these regions the F sensitivity is significantly reduced.

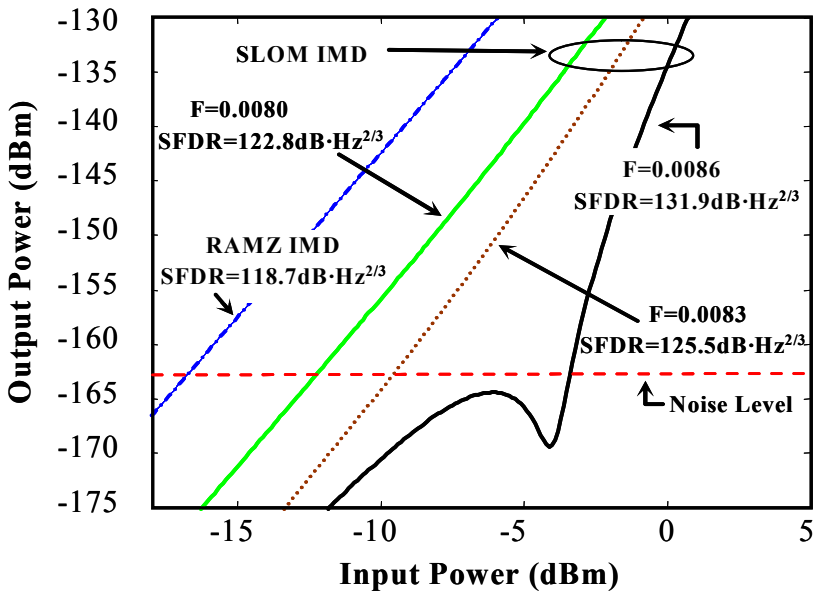

Figure 4.11a: Effect of Power Split Ratio (F:1-F) on the IMD

Fig. 4.11b shows the effect on IMD signal when ξ_{pm} is increased for fixed parameters τ and F. It moves the IMD curve to the right, which consequently increases the SFDR value. For τ = 0.208, ω_m = 70.0 GHz, and F = 0.0086, the SFDR value is maximized at ξ_{pm} = 1.96π rad (SFDR=131.9dB), compared to the other two cases (ξ_{pm} =1.94π rad, SFDR=124.8 dB) and (ξ_{pm} = 1.92π rad, SFDR = 122.3 dB). We state here again that applying a similar RF phase shift of $\xi_{rr} = (2\pi - \xi_{pm})$ to the RR will produce the same results.

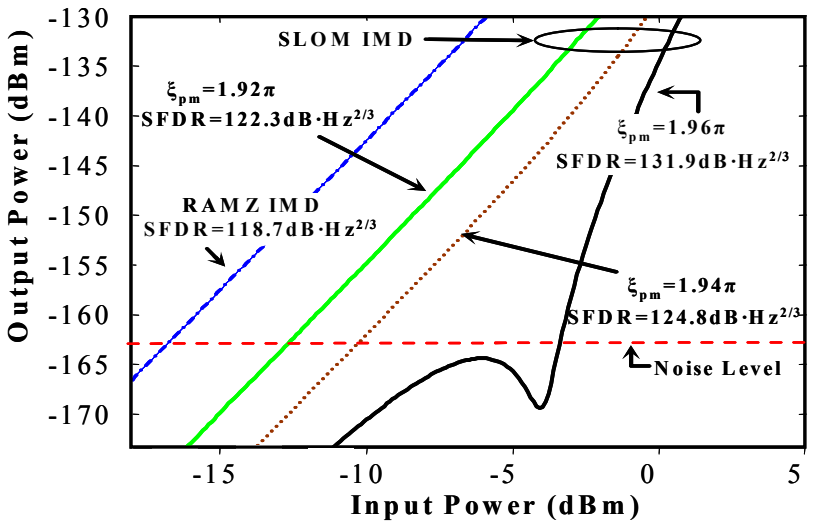

Figure 4.11b: Effect of RF Phase ξ_{pm} on the IMD

Fig. 4.12 shows the frequency dependence of the DR for IMPACC and RAMZ compared to the standard MZ. The DRs of IMPACC for τ = 0.208 and RAMZ with τ= 0.268, are calculated as a function of modulation frequencies from 0 to 75GHz (note that the FSR of the modulator is ~23GHz). We observe four important characteristics.

1. IMPACC provides a large DR (132.9 dB) which is 21.8 dB higher than MZ and 3.7 dB higher than RAMZ at small frequencies (e.g., <2GHz).
2. The bandwidth enhancement of IMPACC over RAMZ occurs at all frequencies (i.e. IMPACC's DR is always greater than RAMZ's). It is important to note that this increased linearization bandwidth is accomplished without resorting to a smaller ring circumference, which relaxes the associated manufacturing complexity.
3. The SFDR of IMPACC is noticeably higher (>5 dB) than RAMZ in the regions around multiples of the FSR. Like RAMZ, the high SFDR values for IMPACC appear to occur in narrow bandwidth regions (3dB BW~10^{-2} FSR) that are

multiples of the free spectral range (FSR) of the modulator. Note that the higher the modulation frequencies the more significant the DR improvement of IMPACC over RAMZ (i.e. 3.7dB @ ~0 GHz, 7.9dB @ 23 GHz, ~11.5dB @47 GHz & ~13.7dB @ 70GHz).

4. At frequencies outside these narrow bandwidth regions, we still observe that IMPACC's DR values still exceed those of RAMZ but the differences are usually smaller - ranging from 0.3 dB to 2 dB - depending on the actual frequency.

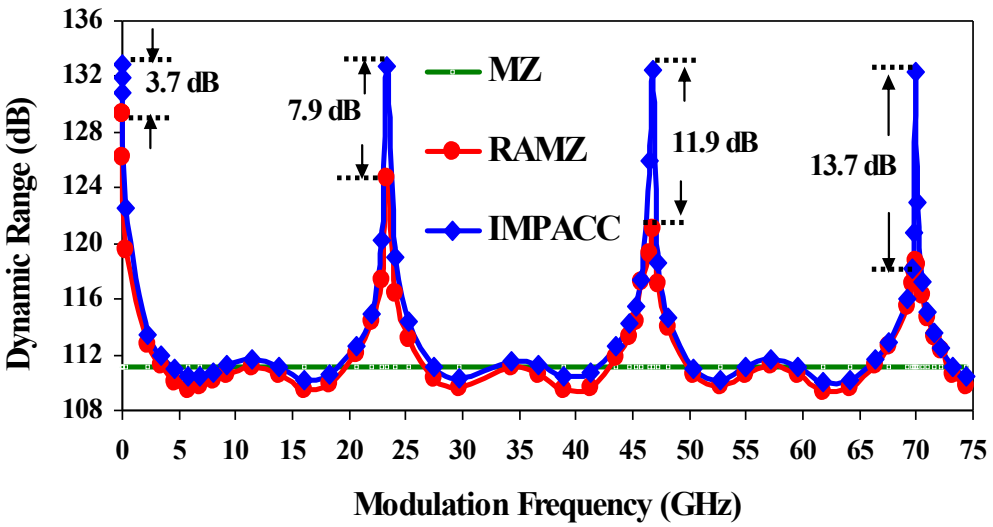

Figure 4.12: Modulation frequency dependence of Dynamic Range of IMPACC vs. RAMZ, $\tau = 0.208$

4.3.3 Sensitivity of *F*, τ and ξ and Maximizing Linearity and Bandwidth

To fully realize the optimum performance of IMPACC, the sensitivity of the parameters F, τ and ξ need to be taken into account. We do not discuss a full sensitivity analysis here, but it is to be noted that the sensitivity of these parameters have a direct impact on the optimization of the linearity and bandwidth capability of IMPACC.

In Fig. **4.13a** we illustrate a typical profile of the SFDR curve (for a specific τ and fixed ξ) for varying F. The SFDR usually increases gradually until the maximum value, after which there is a dramatic drop. This steep gradient corresponds to when the hump on the IMD curve just crosses the noise floor (**Fig. 4.11a**) and in particular because the slope of the IMD curve is different before and after the hump

In **Fig. 4.13b**, we also contrast (for fixed ξ) the SFDR profiles for various τ versus increasing F. This becomes particularly important, as although τ is typically fixed, there will still be some variation (e.g. due to slight temperature changes). So having control of another degree of freedom (RF phase bias, ξ) will help to address this issue.

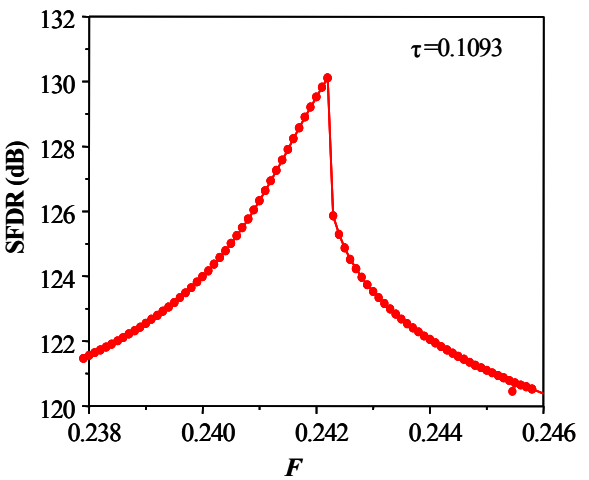

Figure 4.13a: Profile of SFDR curve vs. F

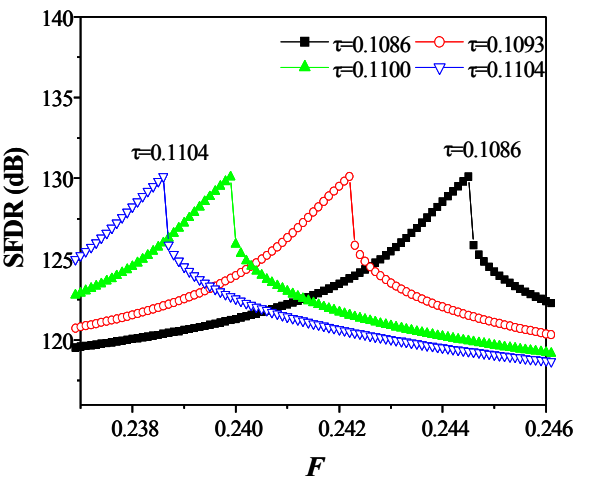

Fig. 4.13b: SFDR curves for various τ

In **Fig 4.14** we demonstrate a particular case, where we vary F and ξ for a fixed τ (τ=0.208). Both F and ξ were adjusted with a sensitivity of 0.1% at a central frequency of 18GHz. This resulted in a 3dB bandwidth of 4GHz. Additional work (as part of the dissertation) will discuss in more detail the dependence of the linearity and bandwidth on the sensitivity control of F, ξ and τ.

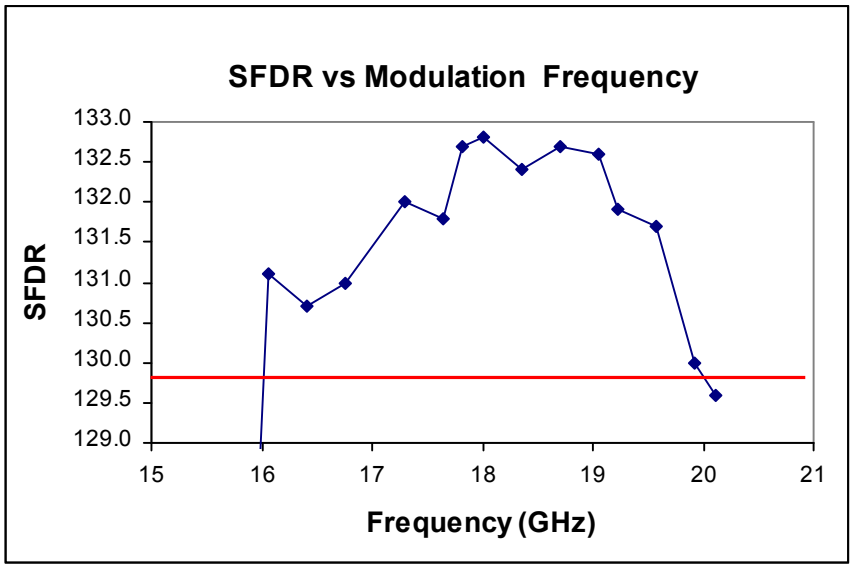

Figure 4.14: Demonstrated ~4GHz 3dB Bandwidth around a central frequency of 18GHz

Fig 4.15 shows (for the same case as above) the symmetry of F and ξ when they are adjusted around a central frequency (18 GHz). As we mentioned earlier, knowledge of the behavior of F and ξ as they are adjusted (for a fixed τ) around a central frequency allows the practitioner to have better control in making parameter adjustments.

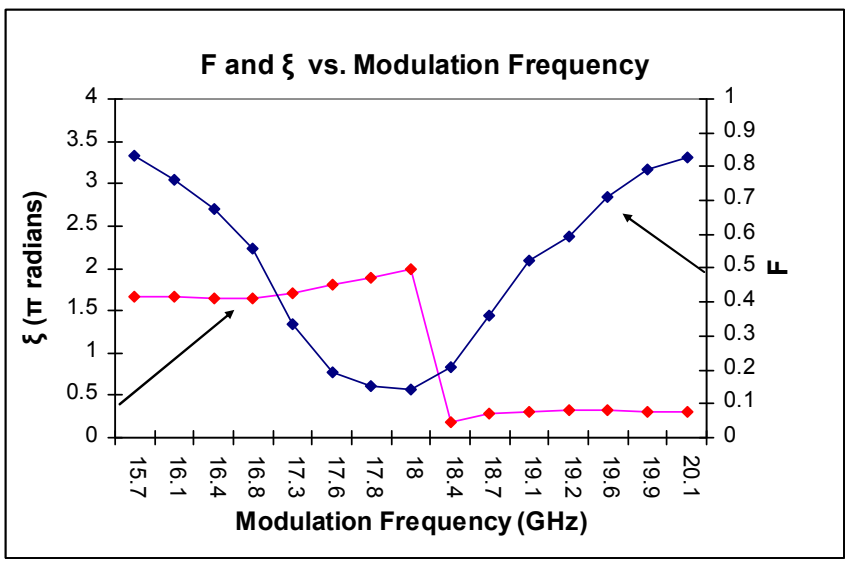

Figure 4.15: Symmetry of *F* and RF Phase bias control around a central frequency of 18GHz

4.3.4 Effect of insertion loss (IL) on SFDR

Figs 4.16a and **4.16b** below demonstrate the impact of higher insertion losses on the fundamental and IMD curves and also the SFDR. A higher insertion loss results in a lower SFDR, as one would expect. As seen in **Figs. 4.16a and 4.16b**, for a specific τ, an increase in the IL from 7dB to 10dB results in a reduction in SFDR by 7.5dB.

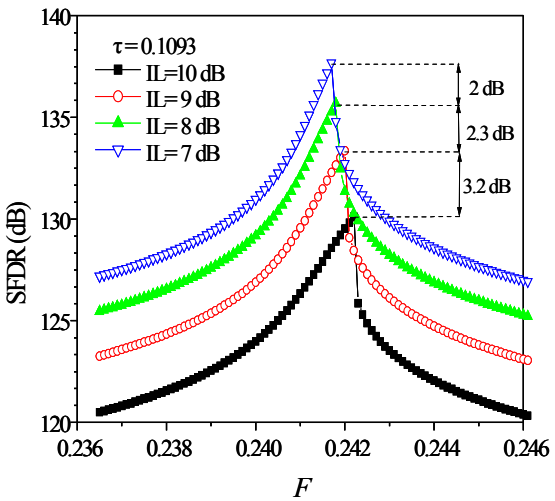

Figure 4 16a: Effect of insertion loss (IL)

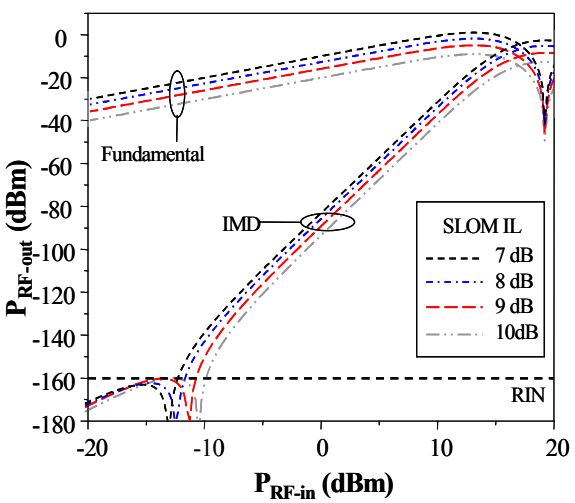

Fig. 4.16b: IL impact on SFDR various τ

Also, as expected, increasing the insertion loss results in lowering the gain and increasing the noise figure (**Fig. 4.17b**). Because IL is such a critical factor in the SFDR response of the modulator, particular attention will be made to address all of the contributors of IL.

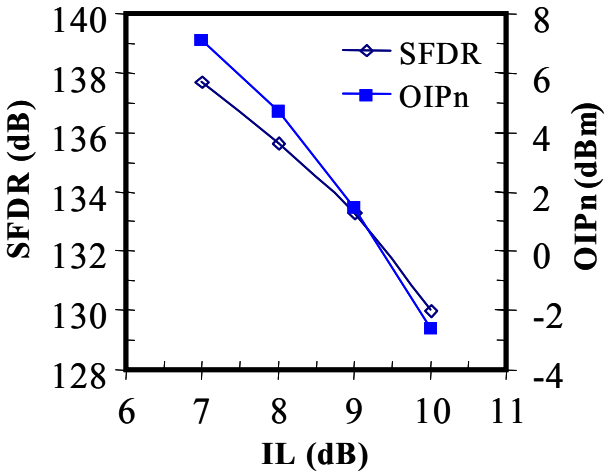

Figure 4 17a: Effect of IL on SFDR and OIPn

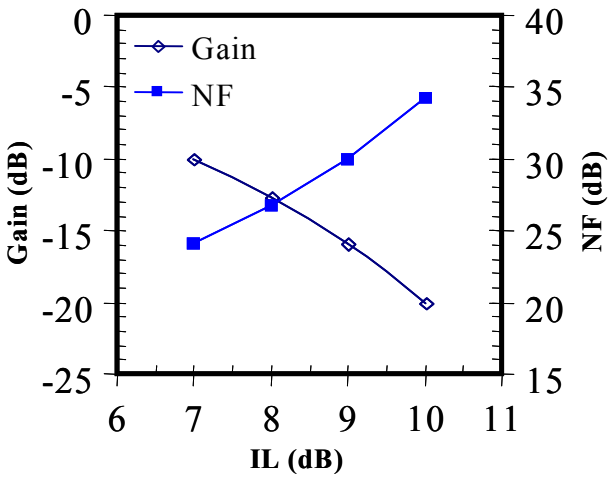

Fig. 4.17b: Effect of IL on Gain and NF

4.3.5 Effect of RR loss on Transfer Functions and SFDR

In Figs. 4.18a and 4.18b below, we address the impact of the RR loss on both the transfer functions and SFDR performance of traveling-wave IMPACC, compared to traveling-wave RAMZ. We use τ=0.208 (for IMPACC) and a low modulation frequency, ω_m=1Hz.

From Fig. **4.18a**, we observe that with a large RR loss (α = 0.8) there is a noticeable change in the amplitude of the transfer function, when compared to the scenario of no RR waveguide loss (α = 1.0). This is more clearly seen in Fig. **4.18b**, where the SFDR of IMPACC with (α = 1.0) is 132.9 dB, and the resultant SFDR is significantly reduced to 113.3 dB with (α = 0.8). Corresponding values for RAMZ are 129.4 dB (α = 1.0) and 109.0 dB (α = 0.8), respectively. Therefore, IMPACC outperforms RAMZ, with or without RR loss, even when no attempt was made to vary the two extra degrees of parameter control (F and ξ_{pm}).

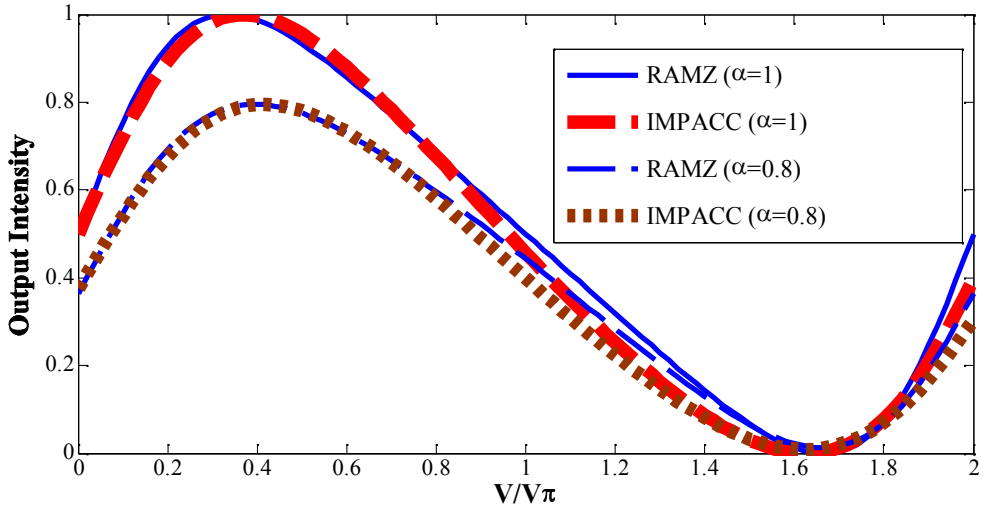

Figure 4 18a: Impact of RR waveguide loss, α on the transfer functions of IMPACC and RAMZ for ω_m=1Hz (F, ξ_{pm} are fixed)

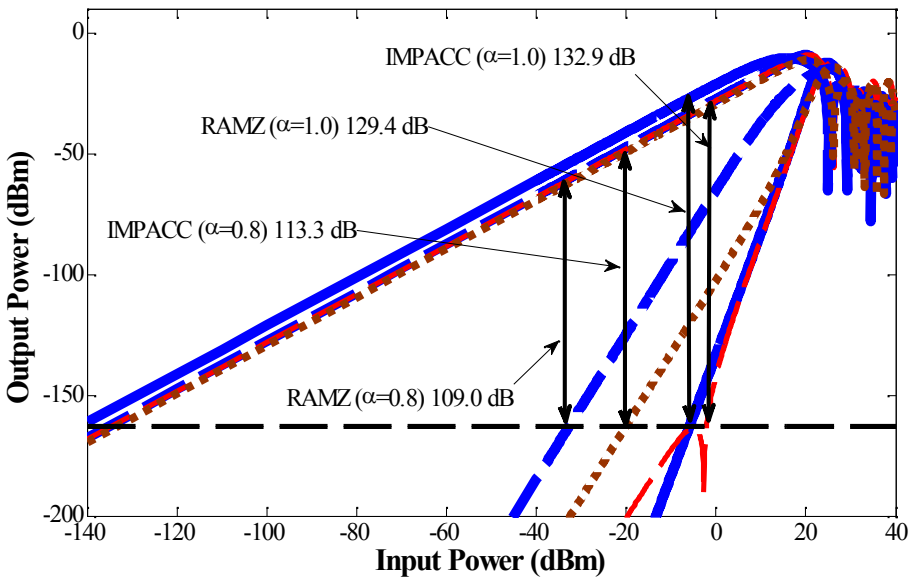

Fig. 4.18b: Impact of RR waveguide loss, α on the SFDRs of IMPACC and RAMZ for ω_m=1Hz (F, ξ_{pm} are fixed)

We further summarize the impact of RR waveguide loss on the SFDR performance of IMPACC and RAMZ, in **Fig. 4.19** below. However, to highlight the

superior performance capability of IMPACC, we now opt to vary only one of the control parameters (F). Note that RAMZ has no such control.

From Fig. 4.19, we make the following observations: (i) the SFDR of IMPACC (with F fixed) remains consistently higher (1.2 dB to 4.3 dB) than that of RAMZ for a range of loss factors (from 0.8 to 1.0), and (ii) changing only one of the control parameters (e.g. F) further increases the SFDR performance of IMPACC (as seen by the top curve). Control of F enables the high SFDR (>130 dB) of IMPACC to be essentially maintained and significantly higher (3.5 dB to 21.8 dB) than that of RAMZ for RR waveguide loss varying from 0 to 1.1dB (that is $1.0 \geq \alpha \geq 0.8$).

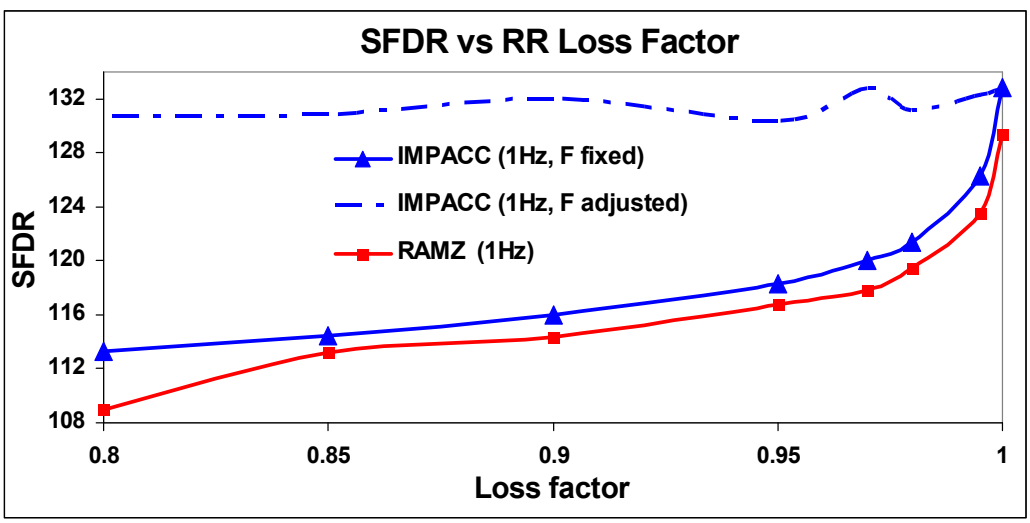

Figure 4.19: Effect of RR loss on the SFDRs for IMPACC vs. RAMZ at low modulation frequency (1Hz)

We illustrate this in the sections below, by studying the modulation frequency dependence of the RF fundamental signal power, P_{Signal}, and the IM power, P_{IM}, for IMPACC and explicitly showing the reduction to RAMZ and MZ. We employ well-known Bessel function identities and the fact that:

$$P_{Signal} \propto \left| \int T(\theta) \exp\left(-i\omega_1 t\right) \right|^2 dt \tag{4.46a}$$

$$P_{IM} \propto \left| \int T(\theta) \exp\left(-i(2\omega_1 - \omega_2)t\right) \right|^2 dt \tag{4.46b}$$

The SFDR, which is defined as the difference between the fundamental output power and the intermodulation output power (at which the intermodulation signal power is equal to the noise floor) can then be calculated. This calculation is done using the parameters in Table I.

4.3.6 Modulation Frequency Dependence of IMPACC

To investigate the modulation frequency dependence of IMPACC, we substitute the transfer function in Eq. 4.35 into Eqns. 4.46a and 4.46b above. Using well-known Bessel function identities, namely:

$$\sin(x\sin\gamma) = 2\sum_{m=1}^{\infty} J_{2m-1}(x)\sin\left[(2m-1)\gamma\right], \tag{4.47a}$$

$$\cos(x\sin\gamma) = J_o(x) + 2\sum_{m=1}^{\infty} J_{2m}(x)\cos(2m\gamma), \tag{4.47b}$$

and carry out the summations to only the first two terms (i.e. up to m=1) we derive the RF signal power and IM power of IMPACC to be:

$$P_{Signal} \propto$$

$$\left| \left(1-\tau^2\right)\sum_{n=1}^{\infty} \tau^{n-1} \begin{bmatrix} \exp\left[-i\left(n\theta+\chi+n\phi/2-\varepsilon_{rr}\right)\right]\times \\ J_0\left(\delta_n\sqrt{1-F}\right)J_1\left(\delta_n\sqrt{1-F}\right)J_0\left(\Delta\beta d_{pm}\sqrt{F}\right)J_0\left(\Delta\beta d_{pm}\sqrt{F}\right)- \\ \exp\left[-i\left(n\theta+\chi+\phi/2-\varepsilon_{pm}\right)\right]\times \\ J_0\left(\Delta\beta d_{pm}\sqrt{F}\right)J_1\left(\Delta\beta d_{pm}\sqrt{F}\right)J_0\left(\delta_n\sqrt{1-F}\right)J_0\left(\delta_n\sqrt{1-F}\right)+\ldots.. \end{bmatrix} \right|^2 \quad (4.48a)$$

$$P_{IM} \propto$$

$$\left| \left(1-\tau^2\right)\sum_{n=1}^{\infty} \tau^{n-1} \begin{bmatrix} \exp\left[-i\left(n\theta+\chi+n\phi/2-\varepsilon_{rr}\right)\right]\times \\ J_1\left(\delta_n\sqrt{1-F}\right)J_2\left(\delta_n\sqrt{1-F}\right)J_0\left(\Delta\beta d_{pm}\sqrt{F}\right)J_0\left(\Delta\beta d_{pm}\sqrt{F}\right)- \\ \exp\left[-i\left(n\theta+\chi+\phi/2-\varepsilon_{pm}\right)\right]\times \\ J_1\left(\Delta\beta d_{pm}\sqrt{F}\right)J_2\left(\Delta\beta d_{pm}\sqrt{F}\right)J_0\left(\delta_n\sqrt{1-F}\right)J_0\left(\delta_n\sqrt{1-F}\right)+\ldots. \end{bmatrix} \right|^2 \quad (4.48b)$$

where $\theta = kn_0 d_{rr}$ and $\chi = \sqrt{1-F}\Delta\beta d_{rr} - kn_0 d_{pm} - \sqrt{F}\Delta\beta d_{pm}$. We note that Eqns. 4.48a and 4.48b have a total of 156 terms, with various permutations of the J's, thereby illustrating the richness of the contributing factors to both the signal and IM RF powers.

4.3.7 Reduction to RAMZ and MZ

The multi-functionality of IMPACC, that is the ability to be reduced to RAMZ or the standard MZ under certain conditions, is easily explained by revisiting Eqns. 4.48a and 4.48b.

4.3.7.1 IMPACC Reduction to RAMZ

To reduce IMPACC to a standard RAMZ, F is set to zero. This implies that no RF power goes to the PM (or all RF power goes directly to the RR. Additionally, $\boldsymbol{\xi_{pm}}$ and $\boldsymbol{\xi_{rr}}$ are set

to 0 and $\theta = \pi$ and $\chi = \chi_1 = \Delta\beta d_{rr}$ (due to the DC component of the RF input). Eqns. 4.48a and 4.48b are modified to:

$$P_{Signal} \propto \left| \left(1 - \tau^2\right) \sum_{n=1}^{\infty} \tau^{n-1} \exp\left(-i\left(n\pi + \chi_1 + n\phi/2\right)\right) J_0\left(\delta_n\right) J_1\left(\delta_n\right) \right|^2 \quad (4.49a)$$

$$P_{IM} \propto \left| \left(1 - \tau^2\right) \sum_{n=1}^{\infty} \tau^{n-1} \exp\left(-i\left(n\pi + \chi_1 + n\phi/2\right)\right) \left[J_1\left(\delta_n\right) J_2\left(\delta_n\right)\right] \right|^2 \quad (4.49b)$$

4.3.7.2 IMPACC Reduction to Standard MZ

Reduction of IMPACC to the standard MZ can be accomplished in two different ways. In one appraoch, the value of *F* is set to 1. This implies that all RF power is directed to the PM. Additionally, ξ_{pm} and ξ_{rr} are set to 0 and θ is set to 0. This implies that no optical power is coupled into the RR. Under these conditions, Eqns. 4.48a and 4.48b reduce to:

$$P_{Signal} \propto \left| J_0\left(\Delta\beta d_{pm}\right) J_1\left(\Delta\beta d_{pm}\right) \right|^2 \quad (4.50a)$$

$$P_{IM} \propto \left| J_1\left(\Delta\beta d_{pm}\right) J_2\left(\Delta\beta d_{pm}\right) \right|^2 \quad (4.50b)$$

In the other approach, the value of F is set to zero. This implies that all of the RF power is directed to the RR. Additionally, τ is set to 0, which implies that optical beam in the L_2 arm will circulate or propagate to the RR only once. Thus, in this case, the RR

acts as a PM with length d_{rr} and the modulator reduces again to a standard MZ. Under these conditions, Eqns. 4.48a to 4.48b reduce to:

$$P_{Signal} \propto \left|J_0(\delta_n)J_1(\delta_n)\right|^2 \tag{4.51a}$$

$$P_{IM} \propto \left|J_1(\delta_n)J_2(\delta_n)\right|^2 \tag{4.51b}$$

4.3.8 Bandwidth Performance of IMPACC vs. RAMZ

As we showed in **Fig. 4.12** above, RR-based modulators, such as RAMZ and IMPACC are typically limited by the FSR of the ring. However, when only one of the two external parameters, ξ_{pm}, is varied and the other, F is fixed, we are able to extend the DR capability of IMPACC beyond that of RAMZ. This is particularly true at the resonances at higher modulation frequencies. In **Fig. 4.12** we use τ = 0.208 for IMPACC, τ= 0.268 for RAMZ, and a PM RF bias control sensitivity, ξ_{pm} of 0.2°. **Fig. 4.12** can be divided into two different regions (i) a resonance region and (ii) a non-resonance region. We now discuss some of the important attributes of the DR performance of IMPACC and RAMZ in these two regions, in addition to the benefit of the multi-functionality of IMPACC in the non-resonance region.

4.3.8.1 Resonance Region

The resonance region is defined as the region where the SFDR is greater than that of the ideal MZ (for example, between ~66 GHz and ~74 GHz and a central frequency of ~70

GHz). We observe some important characteristics. First, IMPACC provides an increasingly higher DR, or increasing resonance enhancement, (from 3.7 dB to 13.7 dB) than RAMZ at the resonant frequency regions. Second, these resonant regions occur at around multiples of the FSR of the modulator (~23 GHz), as seen in Figs. 4.20a and 4.20b below. It is also important to note that the resonance enhancement, as seen in IMPACC, is accomplished without resorting to a smaller ring size, which introduces larger resonator waveguide losses.

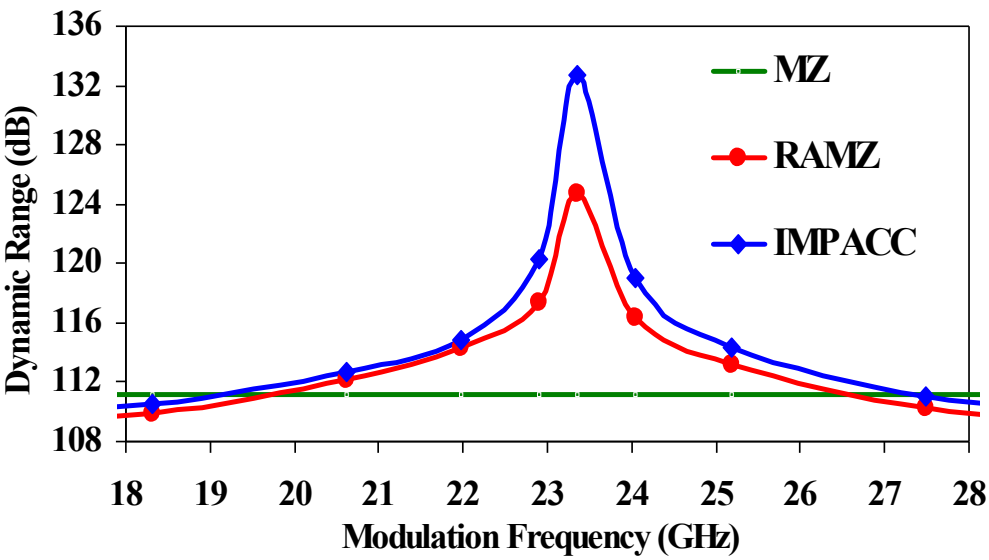

Figure 4.20a: Resonant Region around a central modulation frequency of 23.3 GHz

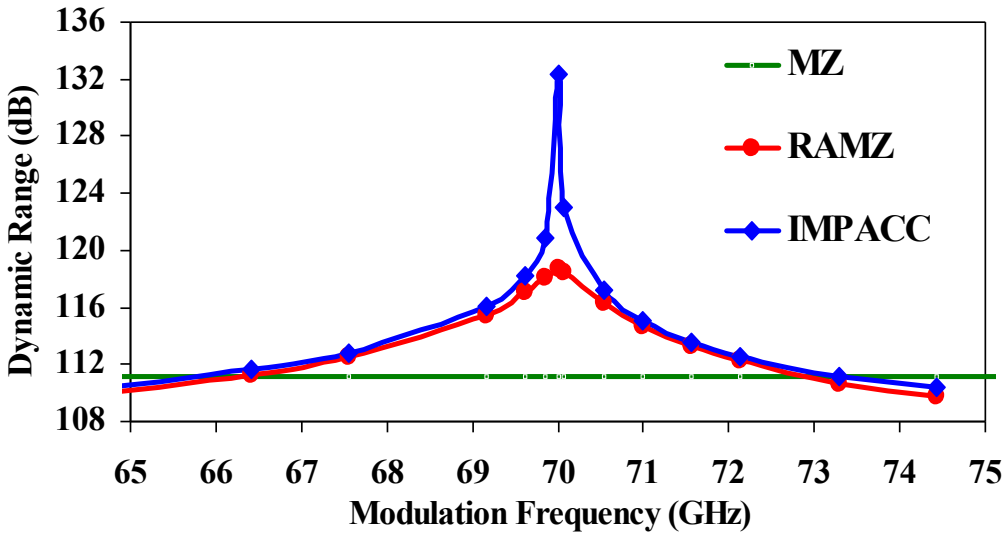

Fig. 4.20b: Resonant Region around a central modulation frequency of 70 GHz

4.3.8.2 Non-Resonance Region

The non-resonance region is obviously defined as the regions outside the resonance regions, where the SFDR is typically less than that of the ideal MZ (for example, between 50 GHz and 66 GHz). At frequencies outside the narrow bandwidth resonant regions, we still observe that IMPACC's DR values exceed those of RAMZ, but the differences are smaller - ranging from 0.3 dB to 2 dB. This is shown in Fig. 4.21 (F is fixed). The explicit (F, ξ_{pm}) dependence of the SFDR in the resonant and non-resonant regions is due to Eqns. 4.44 and 4.45.

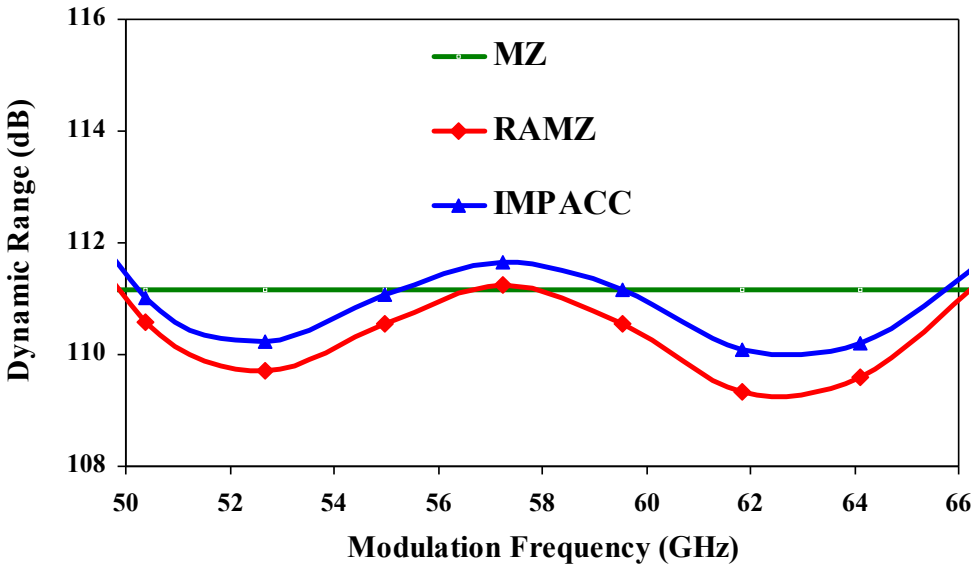

Figure 4.21: Non-Resonance Region around at a large modulation frequency

4.3.8.3 Multi-functionality of IMPACC in the Non-Resonance Region

As mentioned in Section 3, IMPACC has the added benefit of multi-functionality, that is the ability to be reduced to MZ or RAMZ with the appropriate choices of F, τ, ξ_{pm} and ξ_{rr}. If the value of F is set to 1 (all RF power is directed to the PM) and $\boldsymbol{\xi_{pm}}$ and $\boldsymbol{\xi_{rr}}$ are set to 0, IMPACC can be reduced to a standard MZ. The SFDR of MZ in this non-resonance region outperforms both IMPACC and RAMZ. The ability to easily switch from one function to the other adds to the flexibility of IMPACC.

4.3.8.4 SDFR-Bandwidth Optimization of IMPACC

We focus on the lower modulation frequencies (<0.4 times the free spectral range (FSR) of the ring resonator), but this can easily be extended and demonstrated for higher frequencies. In Fig 4.22 we show three scenarios for IMPACC, which we call IMPACC

1, IMPACC 2 and IMPACC 3. We also compare these three scenarios to the bandwidth capability of the standard MZ and RAMZ. The control sensitivities that were used are IMPACC 1: F (0.01%), ξ_{pm} (0.2°), IMPACC2: F (1%), ξ_{pm} (2.0°), and IMPACC3: F (fixed), ξ_{pm} (0.2°).

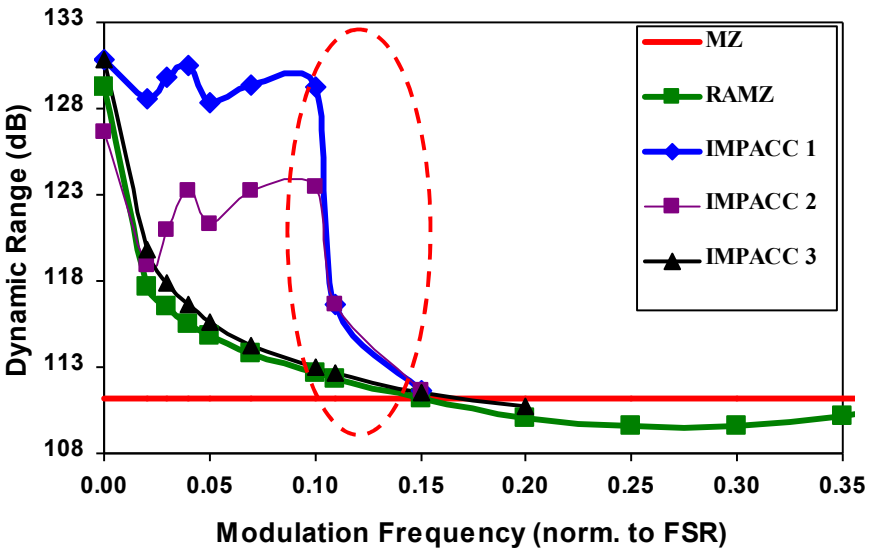

Figure 4.22: Frequency dependence of SFDR for IMPACC compared to RAMZ and MZ.

As shown in Fig. 4.22, the dynamic range (DR) of the ideal MZ is frequency independent and is capped at 111.2 dB. If we define the "effective linearization bandwidth" of resonator-based modulators as the point where the DR equals the DR of an ideal MZ, then we see that the DRs of RAMZ and IMPACC (with τ=0.208) appear to be limited to ~0.15 FSR.

However, one very important performance improvement of IMPACC 1 and IMPACC 2 as compared with RAMZ can be seen in Fig. 4.22 in terms of modulation bandwidth flatness. Here, the effective bandwidths for IMPACC 1 and IMPACC 2 are flat with DR values of about ~129 dB and ~ 123 dB from 0 to 0.12 FSR range, at which

there is a sharp drop in the SFDR capability (see encircled region). This characteristic is not available to the RAMZ case.

In Section 4.2.3, we reported that compared with RAMZ, IMPACC's effective bandwidth range was much wider (0.25 FSR vs. 0.15 FSR) for the lumped electrode design (F=0.22, τ=0.04) and that this increased linearization bandwidth was accomplished without resorting to a smaller ring circumference. Also, it was reported that for the lumped electrode design, the dynamic range of IMPACC never became lower than that of the standard MZ. We note that these two observations were based on a higher d_{pm}/d_{rr} ratio (0.5) and less parameter control sensitivity than any of the three IMPACC designs discussed above. Additional improvement of our optimization algorithms for both the lumped and traveling wave electrode designs will help to address these apparent conflicts between the lumped and traveling wave designs.

4.3.9 CONCLUSION (Part B)

From the above results and discussion, we demonstrate the potential of our proposed super linear traveling wave optical modulator (IMPACC) with both excellent linearity (>130dB) and wider linearization bandwidth compared to RAMZ, by using a novel modulator design and a simple but effective technique that employs external tunable RF phase delay line(s). Also, the ability to have more control over two parameters (the power split - F and the RF phase shift - ξ_{pm}) that are external to the modulator chip enables simpler, flexible and cost effective manufacturing of high linearity modulators.

We also observed that IL is a very critical factor in the performance of the modulator. It becomes particularly important for wide bandwidth, highly linear applications.

Our work shows that this modulator has the potential to meet the high SFDR requirements desired for analog FO-links for antenna remoting and in general analog photonic applications. Future work will be focused on optimizing the modulator performance and testing of externally manufactured devices.

PART C: QUANTUM NON-LINEAR OPTICS APPLICATION

Chapter 5: Quantum Optical Coherence Tomography (QOCT) Theory

5.1. Introduction to Optical Coherence Tomography

Optical coherence tomography (OCT) is a second-order interferometric technique which widely used to image biological samples such as to test tissues for cancer. Unlike ultrasound imaging that uses the resolution of high frequency sound waves for imaging, OCT uses the resolution of light waves. Therefore, since light waves have wavelengths that are orders of magnitude smaller than high frequency sound waves, the resolution capability of OCT is inherently superior to ultrasound.

The resolution is directly proportional to the wavelength of the source. For a Gaussian source, the axial resolution (or depth resolution) is:[43]

$$\Delta z = \frac{2\ln 2}{\pi}\left(\frac{\lambda^2}{\Delta\lambda}\right) \tag{5.1}$$

where Δz and $\Delta\lambda$ are the full widths at half maximum (FWHM) of the auto correlation function and power spectrum respectively, and λ is the central wavelength of the source. From Eq. 5.1, we note that in order to achieve high axial resolution, $\Delta\lambda$ has to be very large, which implies the need for high broadband sources. The transverse resolution (minimum spot size) is determined by the focusing properties of the optical beam and is

inversely proportional to the numerical aperture (NA) of the angle of focus of the beam. The transverse resolution is stated as:[43]

$$\Delta x = \frac{4\lambda}{\pi}\left(\frac{f}{d}\right) \tag{5.2}$$

where d is the spot size on the objective lens and f is the focal length.

Ultrasound has a resolution of ~ 100 μm, and is limited by the wavelength of the sonar waves. And, with a time resolution of ~ 100 ns, direct detection is possible. However, Optical Coherence Tomography (which is analogous to ultrasound B mode imaging) has a resolution of~1 to 15 μm, and a time resolution of ~30 fs. This means that direct detection is not possible. Because of this, OCT requires the use of correlation techniques that compare light from two different paths (typically known as the sample and reference paths). More specifically, OCT uses interferometry to perform imaging by measuring the echo time delay and magnitude of back-scattered or back-reflected light. The most common method is based on the Michelson Interferometer. However, another method is based on the Mach Zehnder Interferometer.

In low coherence interferometry, one measures the field of the optical beam, not its intensity. The electrical field of a light wave traveling (in the z - direction) through a medium with refractive index n is given by:

$$E(t) = E_m(t)\cos\left(2\pi\nu t - \frac{2\pi}{\lambda}z\right) \tag{5.3}$$

where $v = c/n$ ($c = 3 \times 10^8$ m/s). When two beams of light interact, their electric fields combine to produce interference.

OCT can be thought of as classical OCT, since it only depends on classical physics equations. A primary issue of OCT is that it is limited by dispersion effects.[44, 45] However, Quantum Optical Coherence Tomography (QOCT) eliminates dispersion that is present in classical OCT. It uses the concept of quantum entanglement (and thus quantum physics). We list a brief timeline of quantum entanglement in Table A1 (in the Appendix). QOCT also enhances the resolution capability by at least a factor of 2 over OCT.[46] We introduce QOCT below. First, we briefly discuss the theory of QOCT and quantum entanglement in the rest of this chapter. In chapter 6, we outline a QOCT experiment using a Mach-Zehnder configuration in free space. We report the results, in addition to some of the challenges.

5.2. Introduction to Quantum Optical Coherence Tomography

Quantum optical coherence tomography (QOCT) is a fourth-order interferometric technique that uses quantum-entangled photons, which are generated via spontaneous parametric down-conversion. This compares to OCT (classical OCT), which is a second-order interferometric technique that uses broadband light and heterodyne detection to perform axial scanning. The use of broadband light in OCT results in group velocity dispersion (GVD) which can significantly impact the resolution of the imaging. This dispersion is essentially eliminated in QOCT due to two effects: (i) the entanglement of the down-converted photons (entanglement of two photons increases the axial resolution by a factor of two), and (ii) using two photons for imaging in QOCT versus one in

OCT.[47] The first reported demonstration of QOCT is credited to Teich et al (2003).[44] They reported a combined resolution improvement of up to a factor of five for QOCT over OCT. Additional work has demonstrated the characterization of biological samples using QOCT.[48]

5.3. Parametric Down-Conversion

Parametric down-conversion can be considered to be the inverse of harmonic generation. We described the process of harmonic generation in an earlier section, in which two incident photons interact to generate another photon with double the original frequency. In parametric down-conversion, a photon of frequency ω_p which is incident on a $\chi^{(2)}$ crystal results in the generation of two new photons of lower frequencies ω_s and ω_i. As mentioned in section 1 above, these two photons are typically referred to as signal and idler photons.

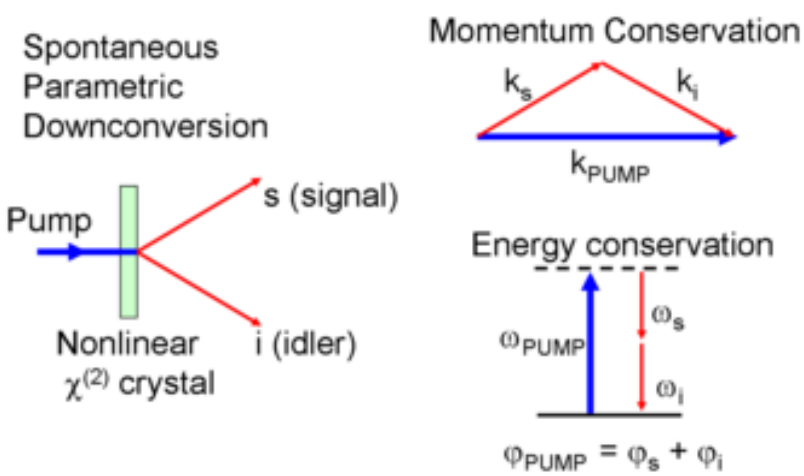

Figure 5.1: Parametric Down-Conversion and Phase Matching[49]

The first theoretical investigation of spontaneous parametric down-conversion in a no-linear crystal was by Klyshko (1968). Harris et al (1967) and Burnham et al (1970)[56] were the first to experimentally demonstrate it. Under phase matched conditions, momentum conservation is preserved and the wave vector relationship is given by:[50]

$$k_p = k_s + k_i \tag{5.4}$$

where k_p, k_s and k_i are the wave vectors of the pump, signal and idler photons. With perfect phase matching, the conversion efficiency from the pump to the signal and idler photons can be quite significant. In this case, we can define:

$$\Delta k = k_p - k_s - k_i = 0 \tag{5.5}$$

Unfortunately, in many cases, perfect phase matching is difficult to achieve and there is negligible depletion of the pump power. In Eq. 5.5, $\Delta k = k_p - k_s - k_i \neq 0$ and the conversion efficiency is significantly reduced. We illustrate this in the following section, by stating the conversion efficiency formulas with a non-depleted pump approximation for three of the nonlinear process described in section 1.4, second harmonic generation (SHG), sum frequency generation (SFG) and difference frequency generation (DFG).

5.4. Negligible Pump Depletion and Non-ideal Phase Matching

If one assumes that all waves are propagating collinearly along the z-axis (as shown in Fig 5.2) and boundary effects are ignored we can derive the following relationships for conversion efficiencies for SHG, SHG and DFG:

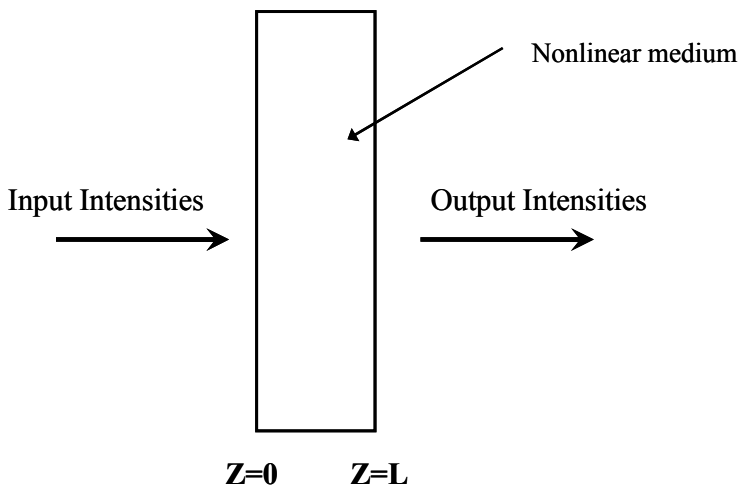

Figure 5.2: Conversion Efficiency in a nonlinear medium depends on medium thickness[1]

<u>Second Harmonic Generation (SHG)</u> $(2\omega = \omega + \omega)$

In SHG, a pump wave with frequency ω is incident on a nonlinear medium, generating a second harmonic with frequency 2ω. If $\eta_{2\omega}$ is the conversion efficiency of this process with non-ideal phase matching, $\eta_{2\omega}^{0}$ is the conversion efficiency with perfect phase matching, $P_{2\omega}$ is the optical power of the second harmonic and P_{ω} is the optical power of the pump wave, L is the z-axis length of the nonlinear medium, d_{eff} is the effective nonlinear coefficient, I_{ω} is the intensity of the pump, n_{ω} is the refractive index

seen by the pump wave and $n_{2\omega}$ is the refractive index seen by the second harmonic wave, then:

$$\eta_{2\omega} = \frac{P_{2\omega}}{P_{\omega}} = \eta_{2\omega}^{0} \frac{\sin^2(\Delta kL/2)}{(\Delta kL/2)^2} \tag{5.6a}$$

$$\eta_{2\omega}^{0} = \frac{8\pi^2 d_{eff}^2 L^2 I_{\omega}}{\varepsilon_0 n_{\omega}^2 n_{2\omega} c \lambda_{\omega}^2} \tag{5.6b}$$

Sum Frequency Generation (SFG) $(\omega_s = \omega_{p1} + \omega_{p2})$

In SFG, an optical wave (with frequency ω_s) is generated when two waves with frequencies ω_{p1} and ω_{p2} are incident on a nonlinear medium. If η_s is the conversion efficiency of this process with non-ideal phase matching, η_s^0 is the conversion efficiency with perfect phase matching, P_s is the optical power of the generated wave and P_{p2} is the optical power of the of the one of the interacting waves with the smaller power, I_{p1} is the intensity of the optical wave with the larger power, n_{p1} is the refractive index seen by the wave with frequency ω_{p1}, n_{p2} is the refractive index seen by the wave with frequency ω_{p2} and n_s is the refractive index seen by the wave with frequency ω_s, then:

$$\eta_s = \frac{P_s}{P_{p2}} = \eta_s^0 \frac{\sin^2(\Delta kL/2)}{(\Delta kL/2)^2} \tag{5.7a}$$

$$\eta_s^0 \frac{8\pi^2 d_{eff}^2 L^2 I_{p1}}{\varepsilon_0 n_{p1} n_{p2} n_s c \lambda_s^2} \tag{5.7b}$$

Difference Frequency Generation (DFG) $\left(\omega_d = \omega_{p1} - \omega_{p2}\right)$

In DFG, an optical wave (with frequency ω_d) is generated when two waves with frequencies ω_{p1} and ω_{p2} are incident on a nonlinear medium. If η_d is the conversion efficiency of this process with non-ideal phase matching, η_d^0 is the conversion efficiency with perfect phase matching, P_d is the optical power of the generated wave and n_d is the refractive index seen by the wave with frequency ω_d, then:

$$\eta_d = \frac{P_d}{P_{p2}} = \eta_d^0 \frac{\sin^2\left(\Delta kL/2\right)}{\left(\Delta kL/2\right)^2} \tag{5.8a}$$

$$\eta_d^0 = \frac{8\pi^2 d_{eff}^2 L^2 I_{p1}}{\varepsilon_0 n_{p1} n_{p2} n_d c \lambda_d^2} \tag{5.8b}$$

In Eqns. 5.6a – 5.8b, we see that as a result of the unequal phase velocities of the interacting waves, a "sinc^2" dependence is introduced. We can also define the phase matching bandwidth, Δk_{BW}, the width of the "sinc^2" function at half-maximum, as:

$$\Delta k_{BW} = 2.784/L \tag{5.9}$$

and the coherence length, L_C, the distance over which the output frequency is generated as:

$$L_C = \frac{\pi}{|\Delta k|} \tag{5.10}$$

To address non-ideal phase matching and low conversion efficiencies, a variety of phase matching techniques are usually employed. These include, temperature phase matching, quasi-phase matching, angle phase matching and Čerenkov phase matching.[1] For purposes of this dissertation, we will only discuss quasi-phase matching, since it is pertinent to the experiment in section 6 below.

5.5. Quasi Phase Matching

In quasi phase matching, a nonlinear crystal is segmented into regions which are each a coherent length, L_C, long. Each segment is also rotated 180° relative to its neighboring segments about the axis of propagation.[51, 52, 53, 54] Due to an absence of inversion symmetry, the result is a change of sign of all of the components of the nonlinear susceptibility tensor. Additionally, the nonlinear polarization wave is shifted by π radians for each coherent length. This coherent length is typically a few microns long. Fig. 5.3 is an illustration of quasi-phase matching in a nonlinear medium.

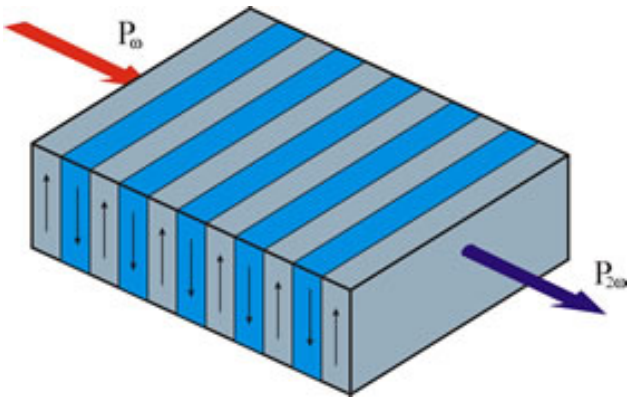

Figure 5.3: Illustration of Quasi-phase matching (each region is a coherent length long)[55]

The effective nonlinear coefficient, d_m for the quasi-phase matching interaction is related to the conventional effective nonlinear coefficient d_{eff} by the relationship:

$$d_m = \begin{cases} \left(2/m\pi\right) d_{eff} & \text{for m odd} \\ 0 & \text{for m even} \end{cases} \tag{5.11}$$

where the coefficient m is referred to as the order of the quasi-phase matching. With this definition, an assuming N segments, we can rewrite Eqns. 5.6a to 5.8b as:[1]

$$\eta_{2\omega} = \frac{8\pi^2 \left(2/m\pi\right)^2 d_{eff}^2 \left(NL_C\right)^2 I_\omega}{\varepsilon_0 n_\omega^2 n_{2\omega} c \lambda_\omega^2} \tag{5.12}$$

$$\eta_s = \frac{8\pi^2 \left(2/m\pi\right)^2 d_{eff}^2 \left(NL_C\right)^2 I_{p1}}{\varepsilon_0 n_{p1} n_{p2} n_s c \lambda_s^2} \tag{5.13}$$

$$\eta_d = \frac{8\pi^2 \left(2/m\pi\right)^2 d_{eff}^2 \left(NL_C\right)^2 I_{p1}}{\varepsilon_0 n_{p1} n_{p2} n_d c \lambda_d^2} \tag{5.14}$$

5.6. Coincidence of Signal and Idler Photons

The concept of coincident photons was first investigated by Burnham and Weinberg (1970).[56] They observed in a coincidence counting experiment that signal and idler photons were separated by a few nanoseconds. They realized that the time correlation between the photons was most likely limited to the time resolution of the detectors, as opposed to an intrinsic result of the down-conversion. The latter is determined by the reciprocal bandwidth of the down-converted light and is typically in the picosecond to sub-picosecond range. Because of this, determination of the true correlation time of the signal/idler photons was not possible with direct measurement. Instead, an interference method, such as that pursued by Hong et al[57] (1987) was a more suitable technique to determine the correlation time for the down-converted photons (see Fig.5.4 below).

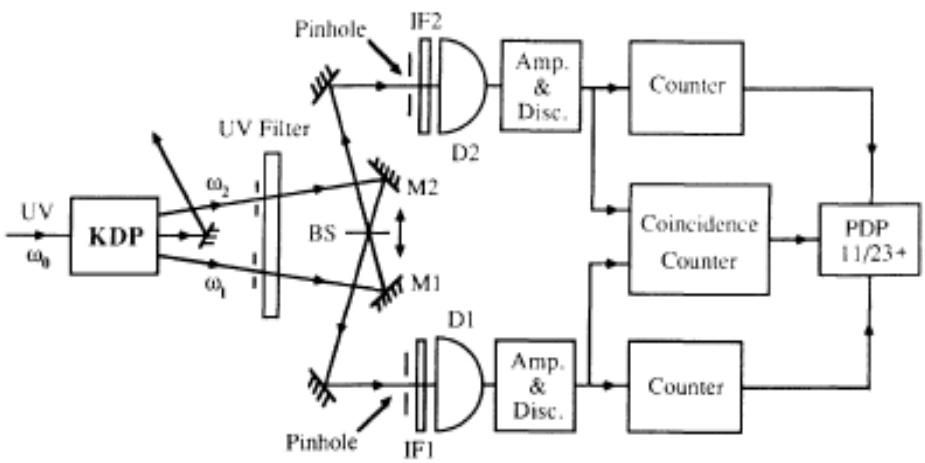

Figure 5.4: Experiment setup to measure the time separation between two photons[57]

Hong et al showed that, given a normalized autocorrelation function of the form $g(\tau) = e^{-(\Delta\omega\delta\tau)^2/2}$ for their experiment, the number of observed coincidences, N_C, can be expressed as:[57]

$$N_C \propto \left(T^2 + R^2\right)\left[1 - \frac{2RT}{T^2 + R^2} e^{-(\Delta\omega\delta\tau)^2}\right] \tag{5.15}$$

Here, T and R are the transmissivity and reflectivity of the final beam splitter, $\Delta\omega$ is the bandwidth of the autocorrelation and $c\delta\tau$ is the increment step size of the stepper motor that drives the reference mirror. Therefore, with a 50:50 BS, $T = R = ½$ and thus $\frac{2RT}{T^2+R^2}$=1. This implies that if $\delta\tau = 0$, the number of observed coincidences N_C become zero under ideal conditions, and an interference dip, such as in Fig. 6.5 is obtained.

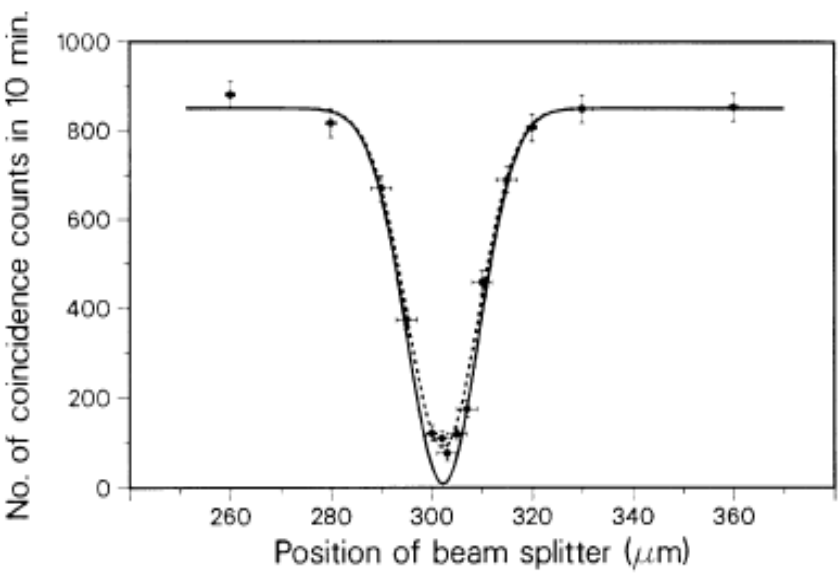

Figure 5.5: Two-photon coincidence measurements as a function of beam splitter displacement (dotted curve: experimental results, solid curve: theoretical results)

In order to get a better understanding of the experiment by Hong et al (Fig. 5.4), we consider the illustration (Fig. 5.6) that shows two input ports, 1 and 2, into the final beam splitter, in addition to two output ports, 3 and 4, out of the beam splitter. If a signal photon travels $c\tau_1$ from the down-converting crystal to the final beam splitter and an idler photon travels $c\tau_2$ from the crystal to the beam splitter, the joint probability for detecting a pair of coincident photons (within a coincidence window τ) at output port 3 and 4, $\mathrm{P}_{34}(t, t+\tau)$, can be determined from the state of the photon field $|\Psi(t)\rangle$ and the fields at the exit ports 3 and 4, $\hat{E}_3^{(+)}(t)$ and $\hat{E}_4^{(+)}(t)$.

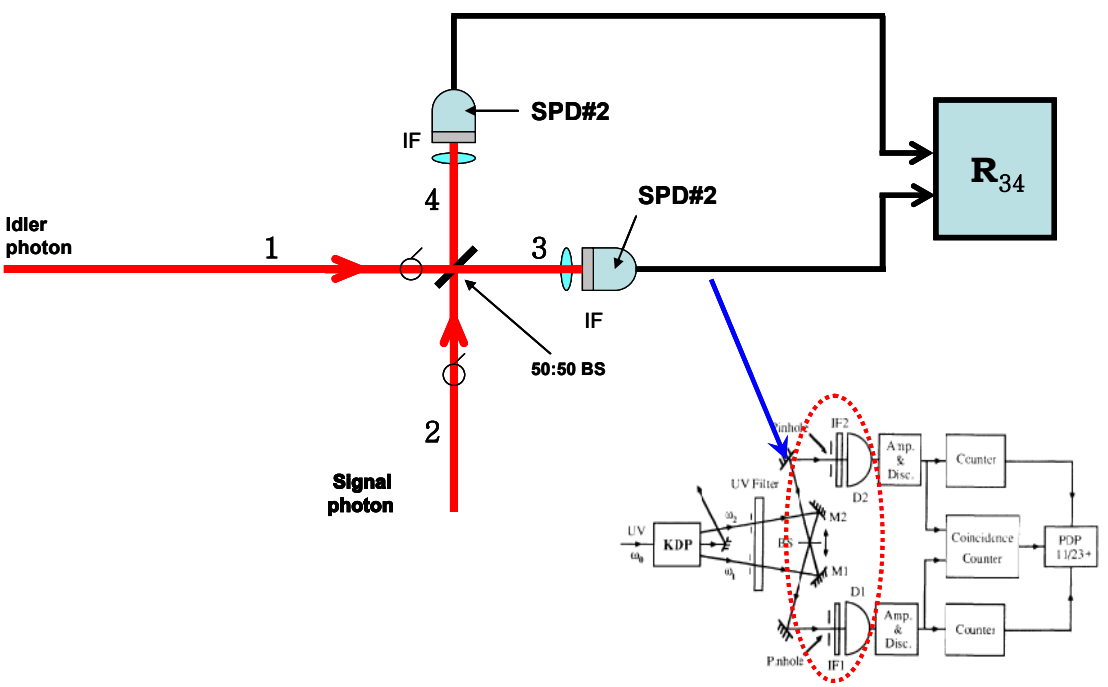

Figure 5.6: Determining the time separation between two photons at the final beam splitter

The fields at the exit ports can be written as:

$$\hat{E}_3^{(+)}(t) = \left(\frac{\delta\omega}{2\pi}\right)^{1/2} \sum_{\omega} \mathrm{T}\,\hat{\mathrm{a}}_{\mathrm{s}}(\omega) e^{-i\omega(t-\tau_1)} + R\,\hat{\mathrm{a}}_{\mathrm{i}}(\omega) e^{-i\omega(t-\tau_2)} \tag{5.16}$$

$$\hat{E}_4^{(+)}(t) = \left(\frac{\delta\omega}{2\pi}\right)^{1/2} \sum_{\omega} R\,\hat{\mathrm{a}}_{\mathrm{s}}(\omega) e^{-i\omega(t-\tau_1)} + \mathrm{T}\,\hat{\mathrm{a}}_{\mathrm{i}}(\omega) e^{-i\omega(t-\tau_2)} \tag{5.17}$$

where R and T are the complex amplitude reflectivity and transmissivity of the beam splitter, $\hat{\mathrm{a}}_{\mathrm{s}}$ and $\hat{\mathrm{a}}_{\mathrm{i}}$ are the photon annihilation operators for the signal and idler modes with frequency ω. If α_3 and α_4 are the quantum efficiencies of the detectors at ports 3 and 4, then the joint probability density that a photon is detected at port 3 at time t and another photon detected at port 4 at time $t+\tau$ is proportional to:

$$\mathrm{P}_{34}(t, t+\tau) = \alpha_3 \alpha_4 \left\langle \Psi(t) \middle| \hat{E}_3^{(-)}(t) \hat{E}_4^{(-)}(t+\tau) \hat{E}_4^{(+)}(t+\tau) \hat{E}_3^{(+)}(t) \middle| \Psi(t) \right\rangle \tag{5.18}$$

The measured coincidence rate, R_{34}, depends on the resolving time of the detectors, T_{R}, and is calculated as:

$$R_{34} = \int_{-T_R/2}^{T_R/2} P_{34}(t, t+\tau) d\tau \tag{5.19}$$

Assuming a pump intensity given as $|V|^2$ and that T_R is much longer than the coherence time $1/\Delta\omega$ it is shown that R_{34} can be written as: [2, 57]

$$R_{34} \propto \alpha_3 \alpha_4 |\eta V|^2 \left[1 - e^{-\Delta\omega^2(\tau_2 - \tau_1)^2}\right] \tag{5.20}$$

with η representing the fraction of the incident pump photons on the nonlinear medium that convert to signal and idler photon pairs.

In the following section, we attempt a similar, though more difficult experiment, in which the coincidence count rate is not only sensitive to frequency, but also to the polarization of the photons interacting at the final beam splitter. Polarization-sensitive interference measurement capability enables the detection of polarization changes from a layered sample, due to scattering and birefringence in the sample. This is critical if the technique is used for the analysis of biological tissue, where a change in birefringence can indicate a problem with the integrity of functionality of the cells. Some examples of tissues that are good candidates for polarization-sensitive measurements include muscle, nerve, tendons and cartilage.[58]

The first experimental QOCT analysis of a biological sample by Nasr et al (2009) shows the potential for QOCT imaging.[48] However, the approach did not use polarization-sensitive QOCT and the experimenters also used a Type-I crystal. Prior to this, the first experimental (and only) attempt to use polarization-sensitive QOCT for

analyzing a reflective sample was done using a type II beta barium borate (BBO) crystal.[58] Our attempt here is to first, increase the flux of the down-converted photons, by using a type II periodically-poled crystal (PPKTP) and second, generate an interference dip, with the ultimate goal of having an experimental setup that can characterize dispersive samples efficiently. Using a periodically-poled crystal provides the added benefit of minimizing the effects of walk-off, which is present in conventional (i.e. not poled) crystals. We introduce our experiment in the next section and discuss our current results.

Chapter 6: TYPE II QOCT Experiment

6.1. Experiment Setup

The experimental set up is shown in Fig. 6.1. It is used to generate quantum-entangled photons. A 405 nm vertically polarized (polarization extinction ratio 100:1) continuous wavelength single mode laser is used as the source. The initial vertical polarization is rotated to horizontal polarization after passing through a dispersion prism and a half wave plate. A Glan-Taylor (GT) prism with a high extinction ratio is used to increase the polarization extinction ratio (e.g. > 10,000:1) before the light passes through a short pass filter that serves as the aperture to a black enclosed box with the experiment components and additional optics. The horizontally polarized 405nm light passes through a converging lens with a focal length chosen so that the minimum beam waist occurs at the center of a type II periodically-poled potassium titanyl phosphate ($KTiOPO_4$) PPKTP crystal. The crystal is placed in a temperature-controlled chamber that maintains the crystal temperature at 39°C. The temperature is chosen to enable quasi-phase matching and maximizing the down-conversion efficiency of the entangled photons.

Two cones of light (one horizontally-polarized and the other vertically-polarized), in addition to the pump beam, emerge from the PPKTP crystal. The pump is extracted by a blocking long pass (LP) filter. At the correct temperature for quasi-phase matching, two intersecting cones with a degenerate central wavelength of 810 nm are sent into the 2^{nd} half of the experiment's black box.

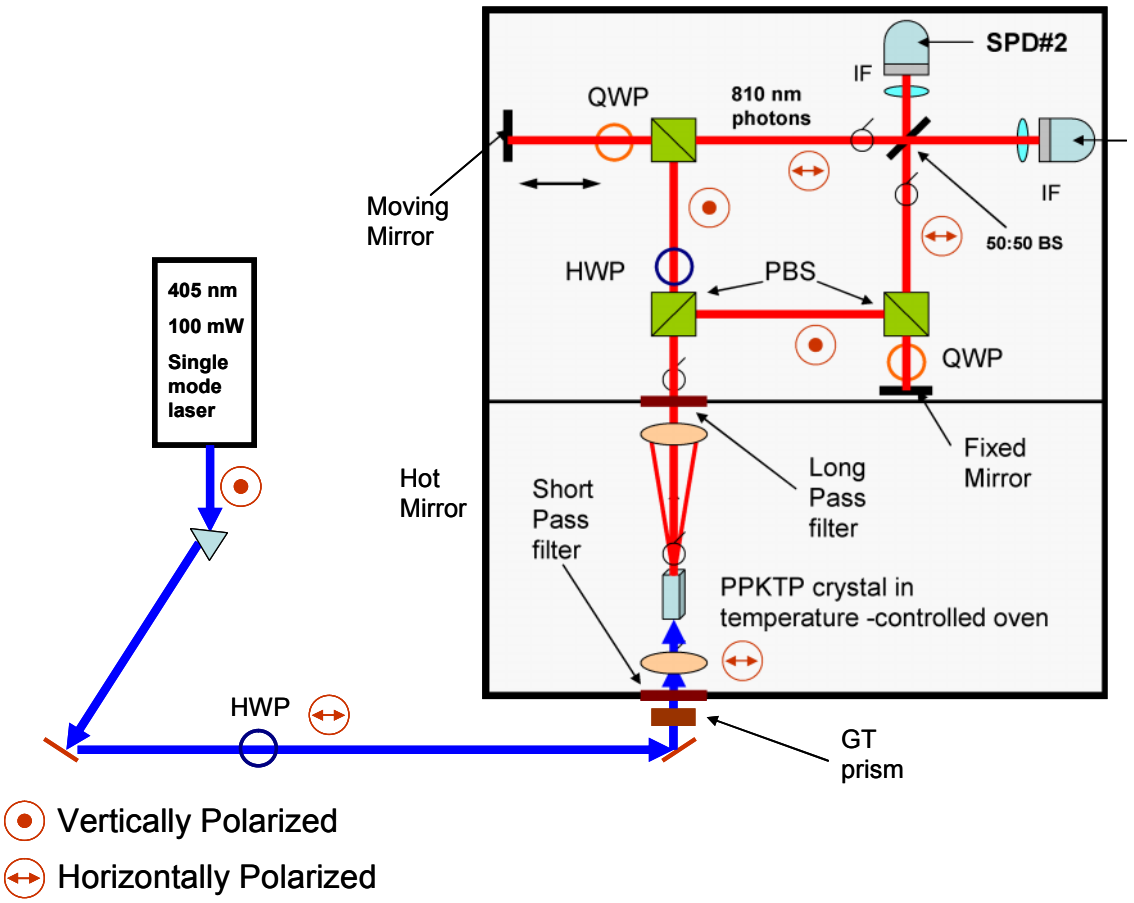

Figure 6.1: QOCT Experiment Configuration

At the first beam polarizing beam splitter (PBS) in the 2nd half of the box, the orthogonally separated cones are separated into the two different arms of the Mach Zehnder interferometer. The horizontally-polarized photons are transmitted into the reference arm. These photons are then changed to vertical polarization with the aid of a half-wave plate (HWP) set to 45°. The now-vertically-polarized photons encounter a second PBS, which reflects the photons towards a quarter wave plate (QWP). The QWP is set to change the polarization of the photons to circularly-polarized photons. These photons are then reflected from a moveable reference mirror and pass through the QWP

once again, thus becoming horizontally-polarized. The horizontally-polarized photons are then incident on a final 50:50 beam splitter (BS).

A similar process happens in the sample arm, where the reflected vertically-polarized photons from the first PBS are again reflected from another PBS (note the absence of a HWP) onto a QWP and then a fixed sample mirror. The reflected photons, which are now circularly-polarized, pass through the QWP, thus becoming horizontally polarized. These photons are also then incident on the final 50:50 BS.

So, in both the sample and reference arms, with the correct orientation, and no sample present, horizontally polarized photons interact at the final 50:50 BS, with the horizontal photons in the sample arm being originally vertical. Returning to the analysis in section 2.2 above, if the reference and sample photons are identical in their physical properties (i.e., polarizations, spatial-temporal mode structures, and frequencies) at the final beam splitter, then destructive quantum interference occurs, resulting in an interference dip with a visibility greater than 50%.

To ensure that the detected photons are the same frequency, we used narrowband filters (FWM~10nm). To ensure the correct spatial-temporal mode in both arms, we use small aperture sizes ($\approx$ 2mm) in addition to forcing equal optical path lengths in both the sample and reference arms (with the help of the moveable reference mirror). In this way, if the photons interacting at the final beam splitter have the same polarization, in addition to these other properties, they are considered to be indistinguishable. Using single photon detectors with high spectral responsivity around 810 nm, and coincidence detection electronics, an interference dip is expected if all of the above conditions are met (refer to Figure 2.3).

Before each experiment is carried out the first step is to carry out a visibility test. The visibility test is quite straightforward. Each arm in the MZI is blocked separately. A half-wave plate (HWP) is plate directly after the PPKTP crystal and it is originally oriented so that the polarizations of the orthogonal signal and idler photons are not changed. This position is defined as the "zero" position (i.e. the angle is set to zero). We show the setup in Fig. 6.2.

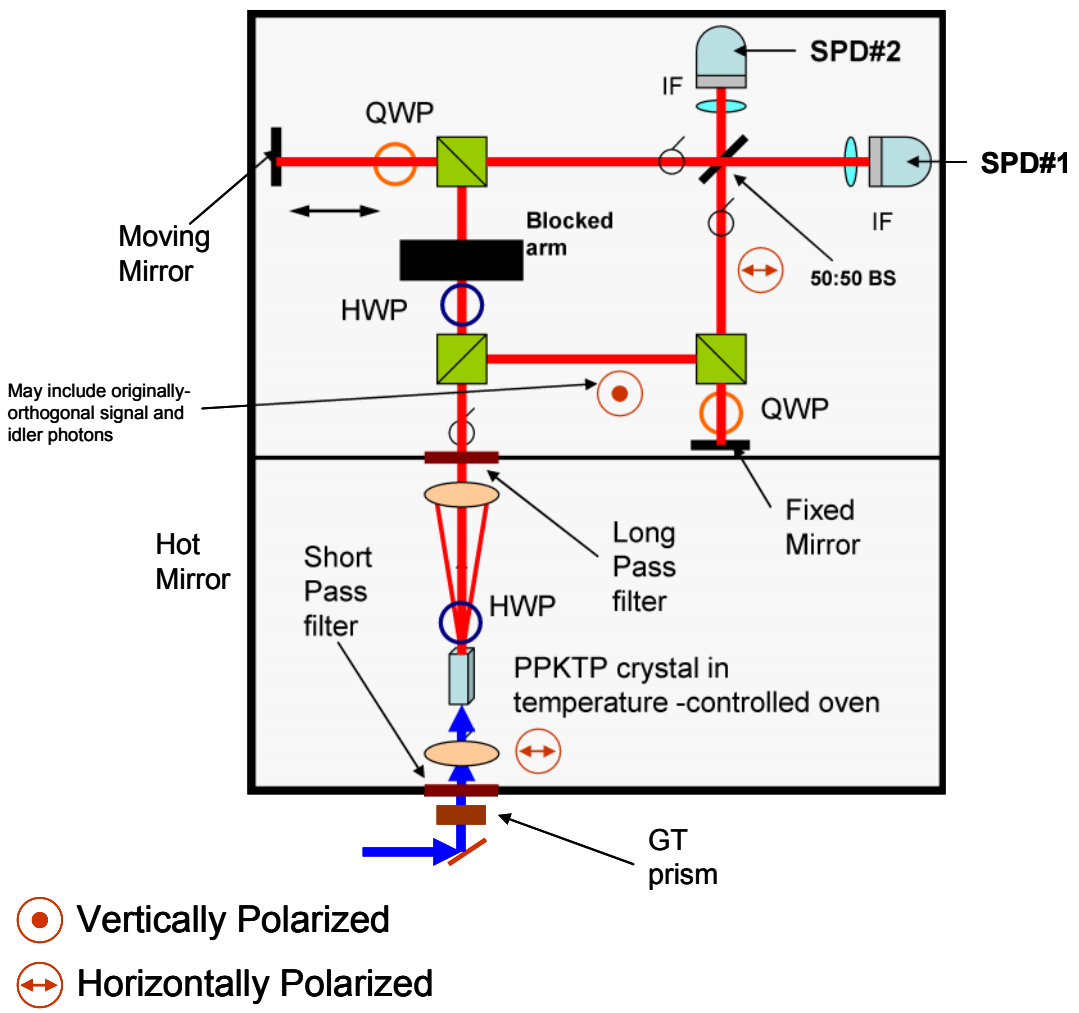

Figure 6.2: Visibility test before experiment is run

As the HWP orientation is incrementally changed in small steps, we record the coincidence counts at the detectors. At the "zero" position, we expect the coincidence

counts to be 0, since only vertically polarized photons should be allowed to pass for the setup in Fig. 6.2 (where the reference arm is blocked). There is some polarization leakage in the PBSs, in addition to other sources of stray coincidence counts, which will account for the fact that the coincidence counts never go exactly to 0 at the "zero" position (Fig. 6.3). The counts are maximum at 22.5° and other angles at ± multiples of 45° from this reference value. At these angles, we expect equal amounts of the projections of down-converted horizontal and vertical polarized photons to be transmitted in the sample arm as "vertically" polarized photons right after the first beam splitter. In this way, coincidence counts are registered at the final beam splitter. Similarly, the counts are minimum at ± multiples of 45° from the zero reference value. Fig. 6.3 shows that the generated visibility with the reference arm blocked was 96.6%. A similar test is also done with the sample arm blocked, with a resultant visibility of 96.1%.

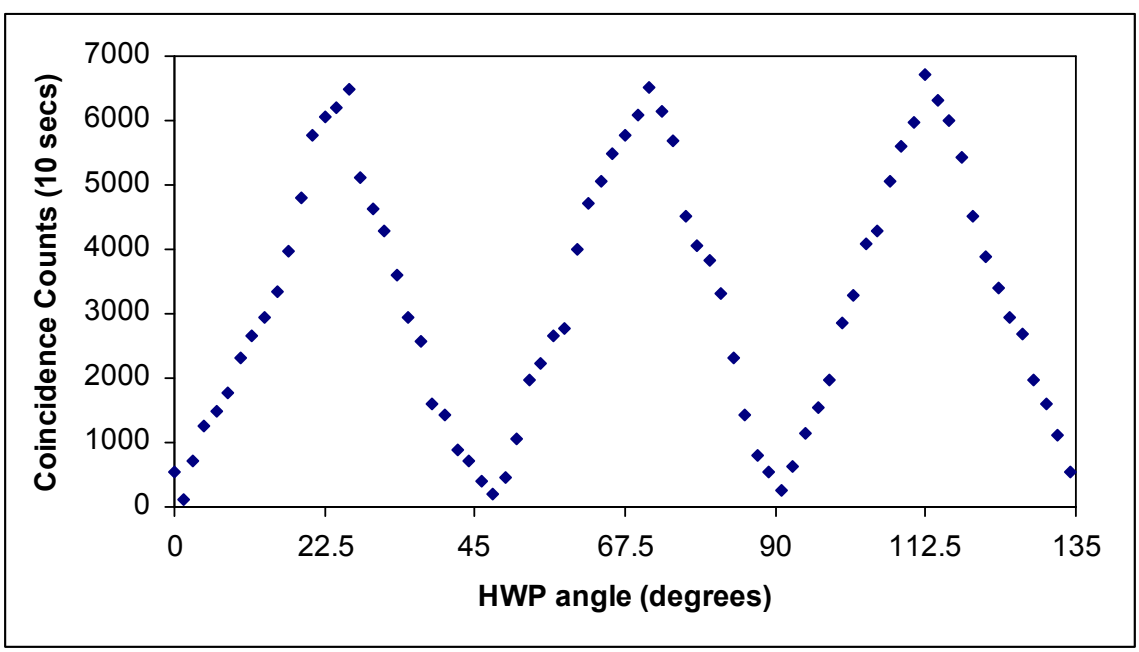

Figure 6.3: Visibility Test Results

If a dispersive sample is placed before the sample mirror using this configuration, it has been shown that certain sample characteristics can be determined, with a higher resolution and less dispersion than OCT.[58] We report our attempt to generate a quantum interference dip (without a sample) using the polarization sensitive QOCT setup above. This has only been successfully demonstrated once, using a type II beta barium borate (beta-BaB_2O_4) crystal and a pulsed Ti-Sapphire laser.[58] By using PPKTP we were able to significantly increase the flux of quantum-entangled photons. Additionally, switching to a CW laser enables higher visibility capability versus a picosecond (pseudo CW) or femtosecond pulsed laser.

6.2. Experimental Results

Generating a quantum interference dip with a polarization-sensitive QOCT experiment configuration proved to be a difficult task. In Fig. 6.4 below, we report our best result to-date in generating an interference dip (with no sample present). The single counts are the sum of the reflected and transmitted photons that enter detectors 1 and 2 (Fig. 6.1) independently. The single count rate in detector 1 was ~320,000 photons/s, while the single count rate in detector 2 was ~ 445,000 photons/s. Ideally, the single counts in both arms should be the same. We account for this difference from effects such as sub-optimal alignment and a non-ideal 50:50 beam splitter. The "drift" in the single counts of each detector is primarily due to beam walk and residual misalignment in the Mach Zehnder interferometer.

The optical path lengths of both arms were determined to within 2mm accuracy. With a large range (~40mm) for the moveable reference mirror, the zero (location for

equal path length was found. An interference dip was generated when the path lengths were equal. However, its visibility (~10%) was much less than desired. The GUI design and control of the stepper motors were done using LabVIEW.

The generated coincidence count rate was ~12,200 counts/s. This represents a coincidence/single count efficiency of ~2.7% to ~3.8%. We note that the "coincidences" typically consist of "true coincidences" and "accidental coincidences". To isolate the accidental coincidences, we set the coincidence window to be as small as possible. For this experiment, the coincidence window was set to <12ns. Additionally, we determined the optimum aperture size for high visibility selection to be ~2mm.

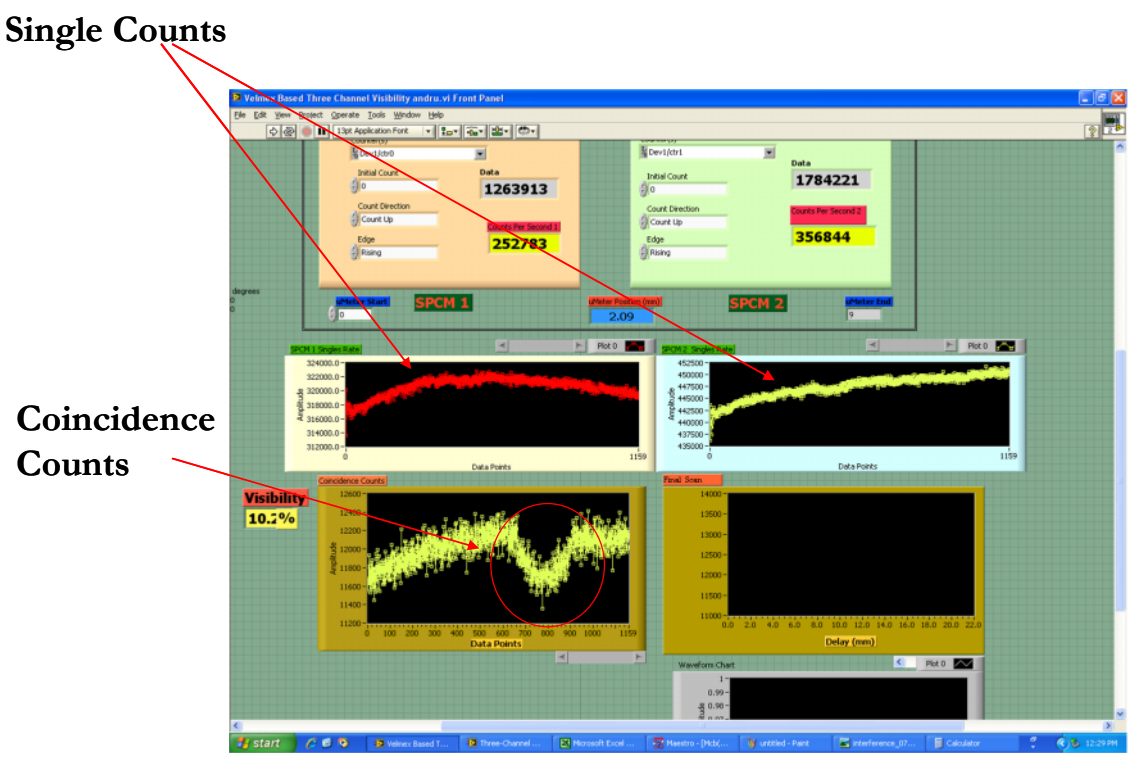

Figure 6.4: Generated Interference Dip and Single Counts

We used Maestro© software to assist in the identification of "true" versus "accidental" coincidences. In Fig. 6.5 below, we illustrate a typical peak that helps to isolate optimum conditions for true versus accidental coincidences. With a sharp "Gaussian" peak, as shown in Fig. 6.5, coupled with balanced single counts in both arms, a scenario for an optimal selection of coincidences is achieved. The coincidence window, in this case, is defined as the extreme edges of the peak.

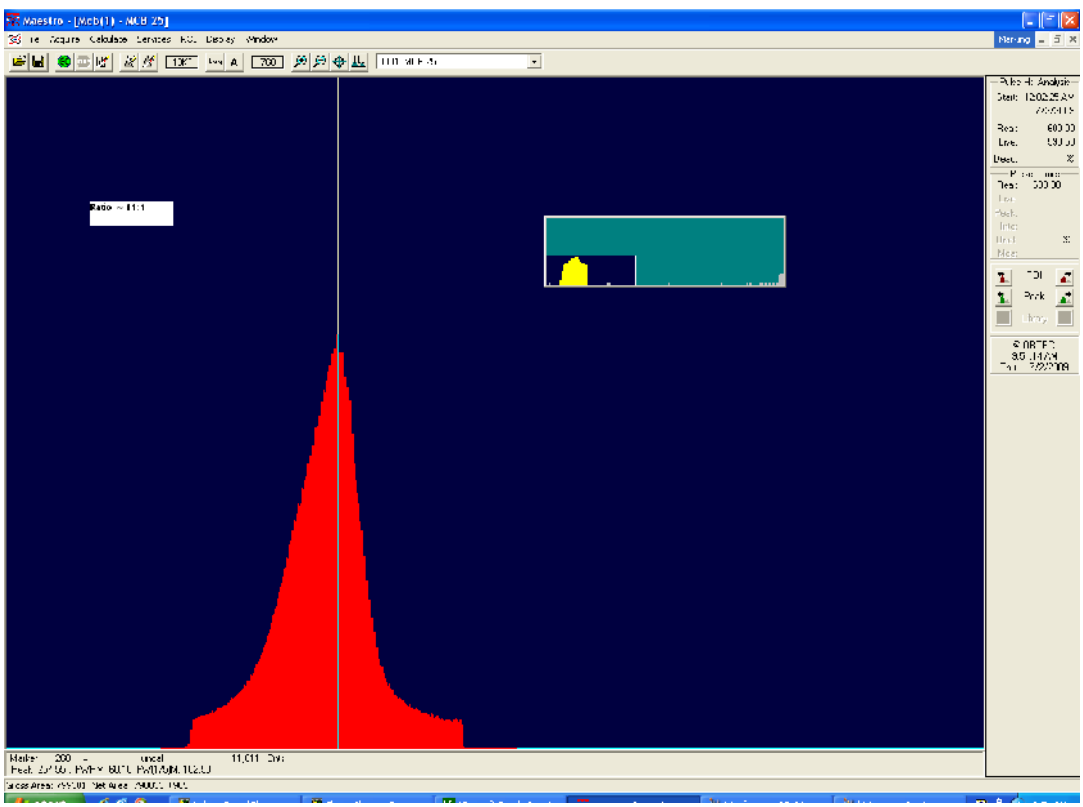

Figure 6.5: Determination of "True Coincidences"

Even with meticulous alignment of the optics, detectors, coupled with vibration isolation and tight temperature control of the PPKTP crystal, it was very difficult to isolate the noise from the data set (as seen in Fig. 6.4 below). With a higher flux of entangled photons (compared with previous experiments), we were able to take as few as 20 measurements per point (with one measurement per second). However, we were still

unable to get very high visibility in our approach. So Fig. 6.4 represents our best efforts to-date. Based on our literature search, this is only the second attempt at a polarization sensitive QOCT experiment using a type II crystal.

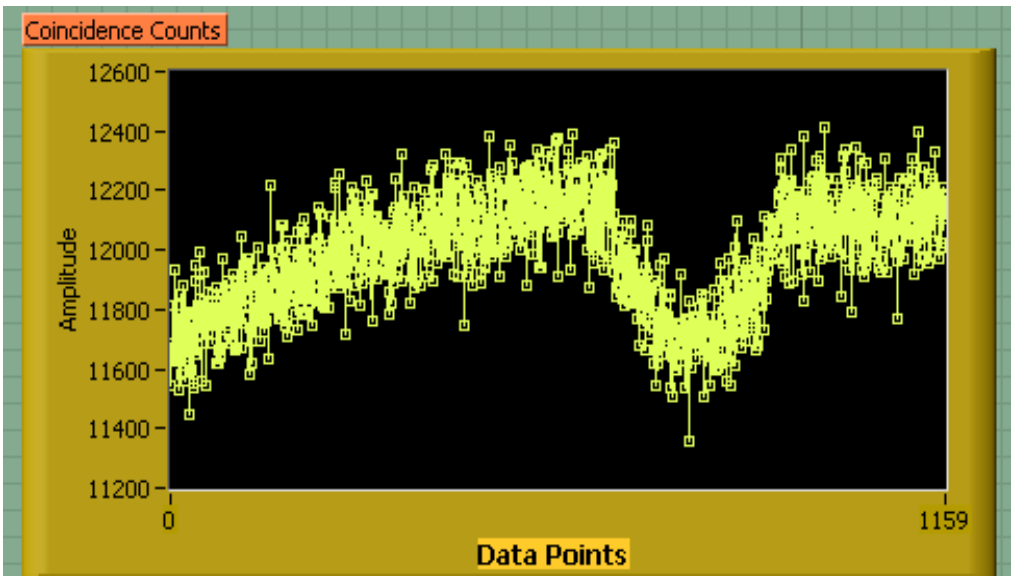

Figure 6.6: Generated Interference Dip

6.3. CONCLUSION (Part C)

From the experimental results in section 7 above, we draw some critical observations. First, in order to ensure that the interference dip is definitely due to quantum interference, we have to get a higher visibility than 50% (versus the attained 10%). In order to achieve optimum results, alignment of the optics and elimination of beam walk is critical. Additionally, maintaining the overlap of two beams at the final beam splitter and vibration elimination are also essential. Since the generation of the

interference dip also assumes indistinguishable photons, very small aperture sizes are required, in addition to proper orientation of the optics to ensure that the polarizations of the incident beams on the final beam splitter are the same.

Future work includes maximizing the dip and characterizing dispersive samples by investigating the effect of polarization on the dip shape (Polarization-sensitive QOCT).

APPENDIX

Overlap integral Γ is calculated as:

$$\Gamma = \frac{g}{V} \iint E \left| E' \right|^2 dA \tag{A.1}$$

where E is the applied electric field, E' is the normalized electric field distribution and A is the electrode cross-sectional area.

Table A.1: Brief Timeline of Quantum Entanglement

Year	
1935	Einstein, Podolsky and Rosen publish a paper that illustrates the conflict between the premises of locality, realism and the completeness of quantum mechanics
1965	Bell mathematically discriminates between local realistic theories and quantum physical predictions for entanglement (Bell's inequality)
1972	1st experiment that demonstrates the violation of Bell's inequality
1988	Shih et al. carry out 1st non-locality experiments using parametric down-conversion (PDC) sources
1992	Time-bin entanglement demonstrated by Brandel, Kwiat et al.
1993	Type-2 PDC source used to generate entangled photons
1997	Entanglement maintained over 10km (Tittel et al.)
1997	1st quantum teleportation experiment
1999	3-photon GHZ state is produced
2004	1st demonstration of time-bin entanglement by FWM in a cooled fiber (Takesue)
2007	General quantum theory describing photon statistics during FWM and Raman scattering in fiber (Agrawal)

REFERENCES

[1] R. L. Sutherland, Ed., "Handbook of Nonlinear Optics", 2nd Edition, Marcel Dekker, Inc. (2003)

[2] L. Mandel and W. Wolf, "Optical Coherence and Quantum Optics", Cambridge University Press (1995)

[3] P. A. Franken, A. E. Hill, C. W. Peters, G. Weinreich, "Generation of optical harmonics", Physical Review Letters, 1961

[4] N. Bloembergen, "Nonlinear Optics", Benjamin, NY (1965)

[5] R. Boyd, "Nonlinear Optics", 2nd Edition, Academic Press (2003)

[6] P. Grangier , G. Roger and A. Aspect, "Experimental Evidence for a Photon Anticorrelation Effect on a Beam Splitter: A New Light on Single-Photon Interferences", Europhysics Letters, **1**, 4.

[7] R. P. Feynman, R. B. Leighton and M. Sands, *The Feynman Lectures on Physics* (Addison-Wesley, Reading, 1965) V. 3.

[8] C. H. Cox III, E. I. Ackerman, G. E. Betts, and J. L. Prince, "Limits on the Performance of RF-over-fiber links and their impact on device design," *IEEE Trans. Microw. Theory Tech.*, Vol. 54, No. 2, February 2006

[9] W. Chang (Ed), *RF Photonics Technologies in Optical Fiber Links*, Cambridge University Press, 2002.

[10] C. H. Cox, III, *Analog Optical Links: Theory and Practice*, Cambridge University Press, 2004

[11] S. A. Pappert and B. Krantz, "RF Photonics for Radar Front-Ends," *Proc. 2007 IEEE Radar Conf.*, p. 965-970, April 2007.

[12] N. Rengand, I. Shpantzer, Y. Achiam, A. Kaplan, A. Greenbalatt, G. Harston, P. S. Cho, "Novel design for the broadband linearized optical intensity modulator", *Military Communications Conference, 2003, MILCOM 2003*. IEEE, Vol. 2, pp. 1208-1212, 13-16 Oct. 2003.

[13] H. Al-Raweshidy, and S. Komaki (Editors), *Radio over Fiber Technologies for Mobile Communications Networks*, Artech House, 2002.

[14] C. Chang (Ed.), *RF Photonics Technology Fiber Links*, (Cambridge University Press, 2002).

[15] L. Gheorma, and R.M. Osgood, Jr., "Fundamental Limitations of Optical Resonator Based High-Speed EO Modulators", IEEE Photonics Technology Letters, **14**, 795 (2002).

[16] X. Xie, J. Khurgin, J. Kang, F-S Chow, "Linearized Mach-Zehnder Intensity Modulator", IEEE Photonics Technology Letters, **15**, 531 (2003).

[17] B. Dingel, "Ultra-linear, broadband optical modulator for high performance analog fiber link system", *in Proceedings of IEEE Microwave Photonics 2004 Tech. Digest*, 241.(2004)

[18] B. Dingel, "Ultra-high Linearized Optical Modulator", US patent 6,943,931, (2005).

[19] E. Ackerman, C. Cox III, and N. Riza (Editors), *Selected Papers on Analog Fiber-Optic Links*, SPIE Milestone Series, Vol. MS-149, 1998.

[20] B. Dingel, R. Madabhushi, and N. Madamopoulos, "Super-Linear Optical Modulator Technologies for Optical Broadband Access Network: Development and Potential", Proc. SPIE, **6012**, 32 (2005).
[21] N. Madamopoulos and B. Dingel, "Performance Analysis of the Ultra-Linear Optical Intensity Modulator", Proc. SPIE, **6390**, 63900D (2006).
[22] B. Dingel and M. Izutsu, "Multifunction optical filter with a Michelson-Gires-Tournois interferometer for wavelength-division-multiplexed network system applications", Opt. Lett., **23**, 1099 (1998).
[23] B. Dingel and T. Aruga, "Properties of a Novel Noncascaded Type, Easy-to-Design, Ripple-Free Optical Bandpass Filter", IEEE Journal of Lightwave Technology, **17**, 1461 (1999).
[24] J. E. B. Oliveira, B. F. R. Sakamoto and W. dos Santos Fegadolli, "Similarities between birefringent Gires-Tournois interferometer and double ring assisted Mach-Zehnder electrooptic modulator," *European Microw. Conf.*, 2007. pp. 1330-1333, 9-12 Oct. 2007.
[25] V. Van, W. Herman and P-T Ho, "Linearized Microring-Loaded Mach-Zehnder Modulator With RF Gain", IEEE Journal of Lightwave Technology, **24**, 4 (2006).
[26] B. Dingel, R. Madabhushi, and N. Madamopoulos, "Super-Linear Optical Modulator Technologies for Optical Broadband Access Network: Development and Potential", Proc. SPIE, **6012**, 32 (2005).
[27] A. Yariv and P. Yeh, *Optical Waves in Crystals*, (Wiley, New York, 1990), p. 243.
[28] A. Yariv, "Universal Relations for Coupling of Optical Power between Micro-resonators and Dielectric Waveguides," *Electronics Letters*, **36**, 321-322, (Feb 2000)
[29] K. Okamoto, *Fundamentals of Optical Waveguides*, Academic Press, 2000
[30] O. Schwelb, "Transmission, group delay, and dispersion in single-ring optical resonators and add/drop filters – a tutorial overview," *Journal of Lightwave Technology*, 22, 1380-1394 (2004)
[31] K.-P. Ho and J. M. Kahn, "Optical Frequency Comb Generator Using Phase Modulation in Amplified Circulating Loop," *IEEE Photonics Technology Letters*, **5**, 721-725 (June, 1993)
[32] H. Tazawa, Y-H Kuo, I. Dunayevskiy, J. Luo, A. Jen, H. Fetterman, and W. Steier, "Ring Resonator-Based Electro optic Polymer Traveling-Wave Modulator", IEEE JLT, **24**, 3514 (2006).
[33] W. Bridges and J. Shaffner, "Distortion in Linearized Electrooptic Modulators", IEEE Transactions on Microwave Theory and Techniques, **43**, 9 (1995).
[34] H. Tazawa and W. Steier, "Bandwidth of Linearized Ring Resonator Assisted Mach-Zehnder Modulator", IEEE Photonics Technology Letters, **17**, 1851 (2005).
[35] A. Prescod, B. Dingel and N. Madamopoulos, "Super-Linear Modulator with Extended Bandwidth Capability for Broadband Access Applications", Proc. SPIE, **7234**, 72340E (2009).
[36] *G.* E. Betts, L. M. Johnson, C. H. Cox III**, "**High-Sensitivity Lumped-Element Bandpass Modulators in LiNbO," *IEEE J. of Lightw. Techn.*, Vol. 7, No. 12, pp 2078-2083, Dec. 1989.
[37] B. Dingel, "General Multi-function Optical Filter" US Patent 6,304,689, 2001.

[38] *G.* E. Betts, L. M. Johnson, C. H. Cox III**, "**High-Sensitivity Lumped-Element Bandpass Modulators in LiNbO," *IEEE J. of Lightw. Techn.*, Vol. 7, No. 12, pp 2078-2083, Dec. 1989.
[39] G. E. Betts, L. M. Johnson, and C. H. Cox, III, "Optimization of externally modulated analog links", *Proc. SPIE 1562, Devices for Optical Processing,* Ed: D. M. Gookin, pp. 281-302, 1991.
[40] J. E. B. Oliveira, B. F. R. Sakamoto and W. dos Santos Fegadolli, "Similarities between birefringent Gires-Tournois interferometer and double ring assisted Mach-Zehnder electrooptic modulator," *European Microw. Conf.*, 2007. pp. 1330-1333, 9-12 Oct. 2007.
[41] R. C. Alferness, "Waveguide Electrooptic Modulators", IEEE Transactions on Microwave Theory and Techniques, **30**, 8, 1982
[42] H. Tazawa, Ring Resonator based Electro-Optic Polymer modulators for Microwave Photonics Applications, PhD Thesis (2005).
[43] B. E. Bouma and G. J. Tearney, Eds., "Handbook of Optical Coherence Tomography", Marcel Dekker, Inc. (2002)
[44] M. B. Nasr, B. E. A. Saleh, A. V. Sergienko, and M. C. Teich, "Demonstration of Dispersion-Canceled Quantum-Optical Coherence tomography", Physical Review Letters, **91**, 8 (2003).
[45] M. B. Nasr, B. E. A. Saleh, A. V. Sergienko, and M. C. Teich, "Dispersion-canceled and dispersion-sensitive quantum optical coherence tomography", Optics Express, **12**, 7 (2004).
[46] J. Perina Jr., A. V. Sergienko, B. M. Jost, B. E. A. Saleh, and M. C. Teich, "Dispersion in femtosecond entangled two-photon interference", Physical Review A, **59**, 3 (1999).
[47] A. F. Abouraddy, M. B. Nasr. B. E. A. Saleh, A. V. Sergienko, and M. C. Teich, "Quantum-optical coherence tomography with dispersion cancellation", Phys. Rev. A, **65**, 053817.
[48] M. B. Nasr, D. P. Goode, N. Nguyen, G. Rong, L. Yang, B. M. Reinhard, B. E. A. Saleh, M. C. Teich, "Quantum optical coherence tomography of a biological sample", Optics Communications, **282** (2009) 1154-1159.
[49] Kumar et al., "Optical-Fiber Entanglement Sources and Quantum Frequency Conversion in PPLN Waveguides", Research Laboratory of Electronics at MIT (2003)
[50] K. Kato and E. Takaoka, "Sellmeier and thermo-optic dispersion formulas for KTP", Applied Optics, **41**, 24 (2002)
[51] W. H. Peeters and M. P. van Exter, "Optical characterization of periodically-poled $KTiOPO_4$", Optics Express, **16**, 10 (2008)
[52] B. Zhao, X. Liang, Y. Leng, C. Wang, J. Du, R. Li and Z. Xu, "Study of Noncollinear Quasi-Phase Matching Optical Parametric Amplification with Group-Velocity Matching Based on Periodically Poled Crystals", Japanese Journal of Applied Physics, 44, 8 (2005 6029-6034
[53] L. E. Myers, R. C. Eckardt, M. M. Fejer, R. L. Byer, W. R. Bosenberg, J. W. Pierce, "Quasi-phase-matched optical parametric oscillators in bulk periodically poled $LiNbO_3$", J. Opt. Soc. Am. B, **12**, 11 (1995)

[54] S. Nagano, R. Shimizu, Y. Sugiura, K. Suizu, K. Edamatsu, H. Ito, "800-nm Band Cross-Polarized Photon Pair Source Using Type-II Parametric Down-Conversion in Periodically Poled Lithium Niobate", Japanese Journal of Applied Physics, **46**, 44 (2007)
[55] http://www.gkoe.com/products_cn/ppktp_ppslt.php
[56] Burnham and Weinberg, Phys. Rev. Lett., **25**, 84 (1970)
[57] C. K. Hong, Z. Y. Ou and L. Mandel, "Measurement of Subpicosecond Time Intervals between Two Photons by Interference", Physical Review Letters, **59**, 18 (1987).
[58] M. Booth, G. Di Guiseppe, B. E. A. Saleh, A. V. Sergienko, M. C. Teich, "Polarization-sensitive quantum optical coherence tomography", Physical Review A, **69**, 043815 (2004)

List of Conference and Journal Publications

[1] A. Prescod, B. Dingel and N. Madamopoulos, “Super-Linear Modulator with Extended Bandwidth Capability for Broadband Access Applications”, Proc. SPIE, 7234, 72340E (2009).
[2] A. Prescod, B. Dingel and N. Madamopoulos, “Traveling wave optical modulator with high dynamic range (>130 dB) at large modulation frequencies”, Proc. Sarnoff Symposium, 978-1-4244-3381-0 (2009)
[3] A. Prescod, B. Dingel and N. Madamopoulos, “Analysis of the Spectrum Characteristics of a Super Linear Optical Modulator”, Proc. SPIE, 7620, 762008 (2010)
[4] A. Prescod, B. Dingel and N. Madamopoulos, “Effect of Ring Resonator Waveguide Loss on the SFDR Performance of Super Linear Optical Modulators”, Photonic Technology Letters, **22**, 17 (2010)
[5] A. Prescod, B. Dingel and N. Madamopoulos, “An Ultra-Linear Modulator with Inherent SFDR Compensation Capability”, Proc. OSA IPR/PS, JTuB22 (2010)
[6] N. Madamopoulos and A. Prescod, “Applications of Large Optical 3D MEMS Switches In Radio-over-fiber In-building Networks”, Proc. OSA IPR/PS, JTuB46 (2010)
[7] B. Dingel, N. Madamopoulos and A. Prescod, “Analytical Model, Analysis and Parameter Optimization of a Super Linear Electro-Optic Modulator (SFDR > 130 dB)”, under review
[8] B. Dingel, A. Prescod and N. Madamopoulos, “Modulation Bandwidth Enhancement of an Optical Modulator with High Linearity Control”, in preparation.